Multiscale Analysis of Failure in Heterogeneous Solids Under Dynamic Loading

Bryan M. Love

Dissertation submitted to the Faculty of the
Virginia Polytechnic Institute and State University
in partial fulfillment of the requirements for the degree of

Doctor of Philosophy
in
Engineering Mechanics

Prof. Romesh C. Batra, Chair
Prof. Michael W. Hyer
Prof. Rakesh K. Kapania
Prof. Raymond H. Plaut
Prof. Surot Thangjitham

November 12, 2004
Blacksburg, VA

Keywords: multiscale analysis, finite element method, adiabatic shear band, ductile
fracture, tungsten heavy alloys

Multiscale Analysis of Failure in Heterogeneous Solids Under Dynamic Loading

Bryan M. Love

(Abstract)

Plane strain transient finite thermomechanical deformations of heat-conducting particulate composites comprised of circular tungsten particulates in nickel-iron matrix are analyzed using the finite element method to delineate the initiation and propagation of brittle/ductile failures by the nodal release technique. Each constituent and composites are modeled as strain-hardening, strain-rate-hardening and thermally-softening microporous materials. Values of material parameters of composites are derived by analyzing deformations of a representative volume element whose minimum dimensions are determined through numerical experiments. These values are found to be independent of sizes and random distributions of particulates, and are close to those obtained from either the rule of mixtures or micromechanics models.

Brittle and ductile failures of composites are first studied by homogenizing their material properties; subsequently their ductile failure is analyzed by considering the microstructure. It is found that the continuously varying volume fraction of tungsten particulates strongly influences when and where adiabatic shear bands (ASB) initiate and their paths. Furthermore, an ASB initiates sooner in the composite than in either one of its constituents.

We have studied the initiation and propagation of a brittle crack in a precracked plate deformed in plane strain tension, and a ductile crack in an infinitely long thin plate with a rather strong defect at its center and deformed in shear. The crack may propagate from the tungsten-rich region to nickel-iron-rich region or vice-a-versa. It is found that at the nominal strain-rate of 2000/s the brittle crack speed approaches Rayleighs wave speed in the tungsten-plate, the nickel-iron-plate shatters after a small extension of the crack, and the composite plate does not shatter; the minimum nominal strain-rate for the nickel-iron-plate to shatter is 1130/s. The ductile crack speed from tungsten-rich to tungsten-poor regions is nearly one-tenth of that in the two homogeneous plates. The maximum speed of a ductile crack in tungsten and nickel-iron is found to be about 1.5 km/s.

Meso and multiscale analyses have revealed that microstructural details strongly influence when and where ASBs initiate and their paths. ASB initiation criteria for particulate composites and their homogenized counterparts are different.

Acknowledgments

Contents

List of Figures

vii

ix

List of Tables

Chapter 1

Introduction

Composites have become common engineering materials. The prospect of producing "designer" materials for specific applications is of great interest to many engineers. However, the thermal and mechanical behavior of these composites is more complex than that of homogeneous materials; many composites are anisotropic and exhibit nonlinear behavior. Experimental testing to determine the behavior of a composite is tedious due to the increased number of material constants and the possibility of unexpected nonlinearities and failure modes. Numerical simulation provides the ability to test a variety of composites under various loading conditions. In this work, we seek to better understand the behavior of heterogeneous materials at both the micro- and the macro-scales. The micro-scale of many composites is far below reasonable length scales for macro-scale simulations; accurate determination of bulk or "effective" properties that capture the overall behavior of the composite is highly desirable. Furthermore, failure modes and instabilities are not guaranteed to behave in the same way as in homogeneous materials–the heterogeneity of the material may cause interesting effects. Bridging the length scales between the macro-scale (at a length scale comparable to the material's application) and the micro-scale (at a length scale comparable to the microstructure of the material) allows one to investigate the effectiveness of the bulk properties to capture heterogeneity-driven phenomena. A greater understanding of these phenomena is needed for critical uses of these materials.

In this work, we focus on a class of particulate composites known as tungsten-heavy alloys (WHAs). WHAs are high density, high strength materials that are of interest in high strain-rate loading scenarios, most particularly, armor and armor-penetration applications. Due to the brittleness of pure tungsten, WHA was developed to prevent brittle fracture/shattering under high stress; a typical WHA consists of tungsten particulates suspended in a nickel-iron matrix. The particulate is typically spherical or ellipsoidal and is randomly distributed; thus the overall composite is isotropic. Unlike many typical composites, both constituents are

capable of thermoelastoviscoplastic deformations–the stiffness of tungsten and nickel-iron are of the same order of magnitude, but their overall response when considering strain- and strain-rate hardening, as well as thermal softening, are decidedly different.

The microstructure of a particulate composite lends itself to the development of a material with a spatial gradation of material properties, something frequently referred to in the literature as a functionally graded material (FGM). FGMs offer designers several interesting possibilities; most particularly, the ability to develop a material with desirable properties on two surfaces without the need for a discrete interface. Here, we investigate the response of tungsten/nickel-iron FGMs under dynamic loading; both in the development of material instabilities and brittle and ductile fracture.

The dissertation is organized as follows: Chapter 1 describes previous work presented by others in the literature, and our contribution, if any, in that area, as well as the model considered here. Chapter 2 focuses on the development of equivalent thermoelastoviscoplastic properties for WHAs. Chapter 3 shows the investigation into the development of adiabatic shear bands in tungsten/nickel-iron FGMs. Chapter 4 examines the brittle and the ductile failure modes of tungsten/nickel-iron FGMs. Chapter 5 summarizes work done on multi-scale analyses that attempt to bridge the length scales of WHAs.

1.1   Literature Review

1.1.1   Determination of Effective Properties

Determination of effective properties of a composite from the properties of the constituents, frequently referred to as homogenization, has been a topic of research for several decades. Much of the past work has been devoted to the determination of elastic constants of composites. Hashin and Shtrikman [1] established upper and lower bounds for the shear and the bulk modulus of a composite composed of multiple linear elastic phases. Mori and Tanaka [2] developed a concept of average stress to account for the interaction among a finite concentration of linear elastic ellipsoidal particles embedded in a linear elastic matrix; Weng [3] implemented this technique for isotropic constituents, giving closed form expressions for the shear and bulk modulus of the composite. Christensen and Lo [4] determined the effective shear modulus of a three phase composite by examining the shear deformation of concentric spheres. Equating the strain energy of the composite sphere to the strain energy of a homogeneous sphere with unknown properties allows for analytical determination of the shear modulus; however, this method does not account for interaction between particulates. There exist many methods for determination of elastic parameters of various types of materials;

these are summarized in Nemat-Nasser and Hori [5].

Estimation of the viscoplastic parameters of a composite is much more challenging. Suquet [6] determined the upper and the lower bounds of the yield stress of a particulate composite composed of multiple incompressible power law materials. For a random dispersion of isotropic spherical particulates in an isotropic matrix, Suquet derived an expression for the effective yield stress of the composite that relies on the yield stress of the constituent and the effective shear modulus of the composite. Willis [7] and Talbot and Willis [8] established bounds for the stress-strain curve of a multi-phase nonlinear composite by using a variational technique similar to that of Hashin and Shtrikman [1]. Ponte Castaeda [9] developed a second-order technique for homogenization of multi-phase materials into a nonlinear homogeneous material, given prior knowledge of the stress concentrations within the composite and an admissible constitutive relation. Many researchers have focused on composites with a viscoplastic matrix and an elastic particulate/inclusion (see Ponte Castaneda [10], Dohgri and Friebel [11], Dvorak and Srinivas [12]), as this is more common with epoxy/carbon systems and metal matrix systems such as aluminum/silicon carbide (see Dai et al. [13]); however, these techniques do not apply to a system where both the matrix and particulate may experience large plastic deformations.

1.1.2 Adiabatic Shear Banding in Functionally Graded Materials

Tresca [14] observed hot lines now called adiabatic shear bands (ASBs) during the hot forging of a platinum bar; they were subsequently also observed by Massey [15]. An ASB is a narrow region, usually a few micrometers wide, of intense plastic deformation that forms after softening of the material due to the heat generated by plastic working overcomes the strain- and strain-rate hardening effects. Even though heat conduction plays a significant role in determining the width of an ASB and possibly spacing between adjacent bands, the adjective adiabatic is used to signify that they form rapidly in a body deformed at a high strain-rate and there may not be enough time for the heat to be conducted away. Their study is important because they precede ductile fracture. The research activity in ASBs increased subsequent to their observation by Zener and Hollomon [16] during the punching of a hole in a steel plate. They also postulated that a material point becomes unstable when thermal softening equals the combined hardening due to strain- and strain-rate effects. Several earlier investigations, e.g. see Recht [17], have used this criterion to determine the average strain at the time of initiation of an ASB and rank materials according to their susceptibility to shear banding; under identical loadings a material in which an ASB forms sooner is more susceptible to shear banding. Bai [18] studied simple shearing deformations

3

of a homogeneous thermoviscoplastic body, neglected elastic deformations, perturbed the homogeneous solution of the governing equations, and hypothesized that an ASB forms when infinitesimal perturbations grow. Batra and Chen [19] have shown that this approach gives the same result as that proposed by Zener and Hollomon [16]. Experimental observations of Marchand and Duffy [20] on the torsion of thin-walled tubes have revealed that an ASB forms much later than when the shear stress peaks and is accompanied by a rapid drop in the torque required to deform the tube. Numerical solutions of simple shearing, plane strain and axisymmetric problems [21] and torsional deformations of a thin-walled tube [22] have confirmed that the load carrying capacity of a member drops significantly upon the formation of an ASB. Much of the literature on ASBs can be found in two books [23, 24], a review paper [25], and special issues of journals [26–30].

One of the earlier papers on FGMs is of Hasselman and Youngblood [31] who showed that the thermal stress resistance of a structural ceramic can be enhanced by properly grading the thermal conductivity. Most works on FGMs have analyzed thermoelastic deformations of plate-like structures, e.g, see [31–42] and those on ASBs have focused on analyzing their initiation and propagation in a homogeneous body. We note that Batra and Zhu [43–45] studied ASBs in a laminated composite body. Here we analyze the problem for a FGM comprised of two constituents with the compositional profile and hence material properties varying continuously in a cross-section. A goal is to find compositions that either enhance or delay the initiation of an ASB. Whereas in a monolithic body, deformations become inhomogeneous due to the interaction of waves reflected from boundaries with the incident waves, in an FGM the additional source of nonuniform deformations is the spatial variation of material properties. In an FGM comprised of particulates in a matrix, waves are also reflected from numerous interfaces between the two phases. The interaction among waves and the sudden change in properties of two constituents give inhomogeneous deformations of the body. However, here first a FG body with continuous variation of material properties is considered. Thus the wave speed varies continuously from point to point and waves are reflected only from the boundaries. The deformations are inherently inhomogeneous. It is found that the compositional profile noticeably affects the time of initiation, the direction of propagation, and the material point from where an ASB forms relative to that in a homogeneous body comprised of each constituent. Furthermore, an ASB forms sooner in a FGM than in either one of the two constituents. Thus materials of desired susceptibility to adiabatic shear banding can be designed. In Chapter 5 we analyze thermomechanical deformations of a heterogeneous material and compare its response to that of an equivalent homogenized body.

4

1.1.3   Brittle and Ductile Fracture

Modeling crack propagation during the solution of a transient problem by the finite element method (FEM) is very challenging since the crack initiation point and its path are to be determined as a part of the solution of the problem. Three strategies often used to analyze fracture are: (i) introducing cohesive elements along inter-element boundaries that are weak in shear and tension but very strong in compression, (ii) representing a crack as two traction-free surfaces by placing two coincident but unconnected nodes at the crack initiation point and relieving tractions on the newly created crack surfaces, and (iii) reducing elastic constants and stresses developed in the failed region to zero and virtually eliminating these elements from the analysis of the problem. Each of these techniques has its advantages and disadvantages. Technique (i) has often been used to simulate brittle failure wherein strains induced are small and very little plastic deformations occur. When used to study ductile failure, it does not allow for the incorporation of frictional forces between two sliding surfaces formed during the failure process. Whereas technique (iii) can accommodate large plastic deformations, it also does not permit the consideration of sliding between adjacent surfaces surrounding the failed region. Wang and Nakamura [46] have discussed four techniques for simulating material failure; however technique (ii) is not one of them. They adopted technique (i) to analyze failure in TiB/Ti FG ceramic/metal plate in which brittle failure ensues at rather small strains. They modeled the plate material as elastic-plastic and considered inertia forces. An accurate modeling of the crack path and hence its speed of propagation requires a very fine FE mesh.

Most studies (e.g., see [47–54]) on fracture of FGMs have considered their static linear elastic deformations. Following an earlier study of a propagating crack by Atkinson and List [55], there have been at least three studies [56–58] on analyzing propagating cracks in FGMs. Recently, Lee [57] developed displacement and stress fields ahead of a crack propagating at a uniform velocity in a FGM with shear modulus either varying linearly ahead of the crack-tip and Poisson's ratio and mass density kept constant or the shear modulus and mass density varying exponentially but Poisson's ratio kept constant. Works that have analyzed the elastic-plastic fracture of FGMs include that of Jin and Noda [48] who showed that the HRR singularity exists near a stationary crack-tip in a power-law hardening material provided the yield stress is continuous and piecewise continuously differentiable function of the effective plastic strain. Tvergaard [58] modeled the interface between two power-law materials with a graded elastic-plastic layer and investigated crack growth in the FGM layer using a cohesive zone model with constant peak cohesive traction and cohesive energy density. Jin and Dodd [59] have analyzed the crack growth resistance behavior of a ceramic/metal FGM with the background material modeled by the J_2 flow theory and undergoing 3-dimensional quasi-

static plastic deformations. They simulated crack propagation with a cohesive zone model having six material dependent parameters. Small plastic deformations are concentrated near the crack-tip and the crack growth resistance, calculated by the J-integral, was found to increase significantly with the crack extension due to gradation in material properties. Wang and Nakamura [46] used the cohesive zone model to analyze transient infinitesimal elastic-plastic deformations of a dynamically loaded FGM plate. They simulated brittle fracture and found that the energy of separation constituted a small part of the total fracture energy. The former was computed from the cohesive law and the latter equaled the sum of the separation energy and the energy dissipated due to plastic deformations. Thus, a large plastic dissipation translates to higher crack growth resistance. However, no thermal effects, such as heat conduction and material softening due to heating, were considered.

1.2 Formulation of the Problem

The study of materials subjected to large deformations at high strain-rates requires careful formulation of the governing equations. The materials under consideration, tungsten and nickel-iron, are both metallic materials that exhibit thermo-elasto-viscoplastic behavior. The occurrence of ASBs during the analysis requires that one consider large deformations; strains can exceed 100% inside an ASB. Furthermore, due to the high strain-rates, the constitutive theory employed must include strain- and strain-rate hardening, as well as thermal softening. Large plastic deformations can also give rise to porosity in the material; the effect of porosity on the material parameters and the yield surface must be considered. In the next few sections, we will outline the governing equations and the FE formulation used to develop the computer code that is employed for the studies.

1.2.1 Governing Equations

We use rectangular Cartesian coordinates and the referential description of motion to describe transient coupled thermomechanical deformations of an thermo-elasto-viscoplastic body deformed at a high strain-rate in plane strain tension. Deformations of each constituent and the composite body are governed by the following equations expressing, respectively, the balance of mass, the balance of linear momentum, the balance of moment of momentum,

and the balance of internal energy.

$$\rho(1-f)J = \rho_0(1-f_0), \tag{1.1}$$

$$\rho_0(1-f_0)\dot{v}_i = T_{i\alpha,\alpha}, \ i,j = 1,2, \ \alpha = 1,2, \tag{1.2}$$

$$T_{i\alpha}F_{j\alpha} = T_{j\alpha}F_{i\alpha}, \tag{1.3}$$

$$\rho_0(1-f_0)\dot{e} = -Q_{\alpha,\alpha} + T_{i\alpha}\dot{F}_{i\alpha}. \tag{1.4}$$

Here ρ is the present mass density, f the porosity (i.e., the volume fraction of voids), $J = \det \mathbf{F}$, $F_{i\alpha} = x_{i,\alpha} = \partial x_i/\partial X_\alpha$ the deformation gradient, $\mathbf{x}$ the present position at time t of a material particle located at the place $\mathbf{X}$ in the reference configuration, $\mathbf{T}$ the first Piola-Kirchhoff stress tensor, e the specific internal energy, $\mathbf{Q}$ the present heat flux measured per unit reference area, $\mathbf{v}$ the velocity of a material particle, a superimposed dot indicates the material time derivative, and a repeated index implies summation over the range of the index. Greek indices refer to coordinates in the reference configuration, and Latin indices to coordinates in the present configuration.

We assume that the strain-rate tensor $\mathbf{D}$ defined by $D_{ij} = (v_{i,j} + v_{j,i})/2, \ v_{i,j} = \partial v_i/\partial x_j$, has the additive decomposition into an elastic part $\mathbf{D}^e$, a plastic part $\mathbf{D}^p$ and a thermal part $\hat{\alpha}\dot{\theta}\mathbf{1}$, viz.,

$$\mathbf{D} = \mathbf{D}^e + \mathbf{D}^p + \hat{\alpha}\dot{\theta}\mathbf{1}. \tag{1.5}$$

Equations (1.1)-(1.5) are supplemented with the following constitutive relations.

$$\dot{\sigma}_{ij} + \sigma_{ik}W_{kj} - \sigma_{jk}W_{ik} = \frac{E(1-f)}{1+\nu}D^e_{ij} + \frac{E(1-f)\nu}{(1+\nu)(1-2\nu)}D^e_{kk}\delta_{ij}, \tag{1.6}$$

$$\dot{e} = c\tau\ddot{\theta} + c\dot{\theta} + \frac{1}{\rho(1-f)}\sigma_{ij}D^e_{ij}, \tag{1.7}$$

$$T_{i\alpha} = J\sigma_{ij}(F^{-1})_{\alpha j}, \tag{1.8}$$

$$q_i = -\kappa\left(1 - \frac{3}{2}f\right)\theta_{,i}, \ Q_\alpha = Jq_i(F^{-1})_{\alpha i}, \tag{1.9}$$

$$\phi \equiv \frac{\sigma_e^2}{\sigma_y^2} - 1 + 2f^*\beta_1\cosh\left(\frac{\beta_2\bar{p}}{2\sigma_y}\right) - \beta_1^2(f^*)^2 = 0, \ \sigma_e^2 = \frac{3}{2}\sigma'_{ij}\sigma'_{ij}, \ i,j = 1,2,3, \tag{1.10}$$

$$D^p_{ij} = \dot{\lambda}\frac{\partial\phi}{\partial\sigma_{ij}} = \dot{\lambda}\left[\frac{3\sigma'_{ij}}{\sigma_y^2} - \frac{f^*\beta_1\beta_2}{\sigma_y}\sinh\left(\frac{\beta_2\bar{p}}{2\sigma_y}\right)\delta_{ij}\right], \ \sigma'_{ij} = \sigma_{ij} + p\delta_{ij}, \tag{1.11}$$

$$p = -(\sigma_{11} + \sigma_{22} + \sigma_{33})/3, \ \bar{p} = pH(-p-0), \tag{1.12}$$

7

$$\dot{\lambda} = \begin{cases} \dfrac{(1-f)\sigma_y \dot{\varepsilon}_e^p}{\sigma_{ij}\dfrac{\partial \phi}{\partial \sigma_{ij}}}, & \text{if } \phi = 0 \text{ and } \dot{\phi} \geq 0, \\[6mm] 0 & \text{when either } \phi < 0 \text{ or } \phi = 0 \text{ and } \dot{\phi} < 0, \end{cases} \tag{1.13}$$

$$\dot{f} = (1-f)D_{ii}^p + \frac{f_2 \dot{\varepsilon}_e^p}{s_2\sqrt{2\pi}} e^{-\frac{1}{2}\left(\frac{\varepsilon_e^p - \varepsilon_n}{s_2}\right)^2} H(-p-0), \tag{1.14}$$

$$f^* = \begin{cases} f, \ f \leq f_c, \\[2mm] f_c + \dfrac{f_u - f_c}{f_f - f_c}(f - f_c), \ f > f_c, \end{cases} \tag{1.15}$$

$$\sigma_y = (A + B(\varepsilon_e^p)^n)\left(1 + C\,ln\left(\frac{\dot{\varepsilon}_e^p}{\dot{\varepsilon}_0^p}\right)\right)\left(1 - \left(\frac{\theta - \theta_r}{\theta_m - \theta_r}\right)^m\right). \tag{1.16}$$

The left-hand side of equation (1.6) equals the Jaumann derivative of the Cauchy stress tensor $\boldsymbol{\sigma}$, $W_{ij} = (v_{i,j} - v_{j,i})/2$ is the spin tensor, E Young's modulus, ν Poisson's ratio, $\hat{\alpha}$ the coefficient of thermal expansion, θ the temperature rise, δ_{ij} the Kronecker delta, $\mathbf{1}$ the identity tensor, c the specific heat, τ the thermal relaxation time, and κ the thermal conductivity of the solid material. Batra and Jaber [60] found that the Jaumann and the Green-Naghdi stress rates in equation (1.6) give virtually identical results for the times of initiation of an ASB and of brittle failure at points near the surface of a notch tip in a dynamically loaded prenotched plate. This is because elastic strain-rates appearing in equation (1.6) are small as compared to the plastic strain-rates at points within an ASB. $\phi = 0$ describes the yield surface proposed by Gurson [61] for a porous material, p is the hydrostatic pressure, and f^* the modified value of the porosity given by (1.15). Gurson's yield surface is based on quasistatic analysis with the matrix material modeled as rigid perfectly plastic and obeying von Mises yield criterion. One should note that in the absence of porosity, (1.10) becomes the classical von Mises yield surface. Wang and Jiang [62] have considered inertia effects. Wang [63] has analyzed transient deformations of a single spherical void in a solid spherical shell made of a power-law heat-conducting viscoplastic material. For a microporous material, Wang [63] derived an approximate expression for the macro-stress potential through an upper bound approach. Constants β_1 and β_2, introduced by Tvergaard [64], provide a better fit of results computed from a FE analysis of the formation of ASBs in a plate having an array of large cylindrical voids with test observations, and $\dot{\lambda}$ is the factor of proportionality defined by (1.13); $\dot{\lambda} > 0$ only when the material point is deforming plastically. σ_y is the current yield stress of the material whose dependence upon the effective plastic strain ε_e^p, the effective plastic strain-rate $\dot{\varepsilon}_e^p$ and the temperature θ is described by the Johnson-Cook [65] relation (1.16) in which A, B, C, $\dot{\varepsilon}_0^p$, and m are material parameters, θ_r the room temperature and θ_m the melting temperature of the material. Parameters B and n characterize the strain

hardening of the material, C and $\dot{\varepsilon}_0^p$ the strain-rate hardening and the last factor on the right-hand side of (1.16) its thermal softening. Equation (1.14) gives the evolution of porosity; the first term on its right-hand side is derived by assuming that the matrix is incompressible and the elastic dilatation is negligible as compared to the plastic dilatation, and the second term is the strain based nucleation of voids introduced by Chu and Needleman [66]. f_2, s_2 and ε_n are material parameters; the rate of nucleation of voids is highest when ε_e^p equals ε_n and decays exponentially with the difference between ε_e^p and ε_n. H is the Heaviside step function. Thus the second term contributes to the evolution of porosity at a point only when the hydrostatic pressure there is tensile. To account for the coalescence of neighboring voids, Tvergaard and Needleman [67] enhanced the porosity, as given by equation (1.15), after it reaches its critical value f_c. In equation (1.15), f_f is the porosity at ductile fracture, and $f_u = 1/\beta_1$ is the porosity when the yield surface has shrunk to a point. Equations (1.10) and (1.16) imply that the radius of the von Mises yield surface increases due to strain- and strain-rate hardening of the material but decreases due to the softening induced by the temperature rise and the increase in porosity. The degradation of material properties due to the damage, taken here synonymous with the porosity, is indicated by equations (1.6) through (1.10). The affine variation with the porosity of Young's modulus, the bulk modulus, the stress-temperature coefficient, and the heat capacity implies that the rule of mixtures (e.g. see Section 2.2.2) has been employed to find their effective values; the expression for the thermal conductivity in equation (1.9) is due to Budiansky [68]. The interaction, if any, among neighboring voids has been tacitly ignored. Jiang and Batra [69], among others, have considered this interaction. The shrinkage of the yield surface due to an increase in porosity described by equation (1.10) can be seen by plotting the yield surface for two different values of f while keeping other variables fixed. Perzyna [29] has given a different equation for the evolution of porosity.

For a functionally gradient or multi-constituent body, all thermophysical parameters may vary with $\mathbf{X}$.

Substitution from equations (1.5), (1.7) and (1.9) into (1.4) gives the following hyperbolic heat equation:

$$\rho_0(1 - f_0)c(\tau\ddot{\theta} + \dot{\theta}) = \left(\kappa\left(1 - \frac{3}{2}f\right)\theta_{,\alpha}\right)_{,\alpha} + J\sigma_{ij}D_{ij}^p. \tag{1.17}$$

The term $J\sigma_{ij}D_{ij}^p$ equals the heating due to plastic working per unit volume in the reference configuration; thus the Taylor-Quinney parameter has been taken as 1. Except for a delay in the time of initiation of an ASB other results remain unaffected by a lower value of the Taylor-Quinney factor. The form (1.17) of the hyperbolic heat equation is due to Cattaneo [70] and

9

Vernotte [71]. The thermal relaxation time τ in it represents the time required to establish a steady state of heat conduction in an element suddenly exposed to heat flux. According to Chester [72] τ equals $3\kappa/\rho c V_0^2$ where V_0 is the speed of an elastic wave. Thus for a typical steel, $\tau = 1 \times 10^{-12}$s, and $\tau \simeq 25 \times 10^{-12}$s for copper. Batra and Lear [73], and Batra and Chen [74] found that the finiteness of the thermal wave speed affects the time of initiation of an ASB in a typical steel and the spacing between adjacent shear bands only when $\tau \geq 10^{-6}$s. Batra [75] considered higher-order spatial and temporal gradients of temperature and derived a heat equation that admits finite speeds of thermal waves. However, in such a material either a thermal wave propagates with a finite speed or the linearized problem has a unique solution. Ideally, one will like to have both.

We note that Batra and Kim [76], Batra and Jaber [60] and Batra and Chen [19] have analyzed different aspects of shear banding with four different thermoviscoplastic relations, namely, the Johnson-Cook [65], the Litonski-Batra (e.g. see Batra [75]), the Bodner-Partom [77] and a power law. These relations were calibrated to give nearly the same effective stress vs. the effective strain curve during homogeneous deformations of the body. However, during inhomogeneous deformations, each one of the relations gave qualitatively similar but quantitatively different results. The decision to use the Johnson-Cook relation here is based on the availability of values of thermomechanical parameters for different materials.

1.2.2   Nondimensionalization of Variables

Let ρ_R, $\dot{\varepsilon}_R$, H, σ_0 and θ_R be the reference mass density, the reference strain-rate, the reference length, the reference stress and the reference temperature used to non-dimensionalize quantities. Then in terms of nondimensional variables indicated by the same symbols as before, equations (1.2) and (1.17) become

$$\alpha_I(1 - f_0)\dot{v}_i = T_{i\alpha,\alpha}, \ i = 1, 2, \ \alpha = 1, 2, \tag{1.18}$$

$$\rho_0(1 - f_0)(\tau\ddot{\theta} + \dot{\theta}) = -\alpha_t \left(\left(1 - \frac{3}{2}f \right) \theta_{,\alpha} \right)_{,\alpha} + J\sigma_{ij}D^p_{ij}, \ i, j = 1, 2, 3, \tag{1.19}$$

where
$$\alpha_I = \frac{\rho_R \dot{\varepsilon}_R^2 H^2}{\sigma_0}, \ \alpha_t = \frac{\kappa}{\rho_R c H^2 \dot{\varepsilon}_R}, \ \theta_R = \frac{\sigma_0}{\rho_R c H^2}. \tag{1.20}$$

α_I and α_t are nondimensional measures of inertia and heat conduction effects respectively. For a given material, inertia effects are directly proportional to the square of the reference strain-rate and the square of the reference length, and heat conduction effects are inversely proportional to the reference strain-rate and the square of the reference length.

1.2.3 General Initial and Boundary Conditions

For most analyses, the body is initially taken to be at rest, with no initial stress and at uniform temperature. There may be an initial porosity distribution to simulate an initial defect. Thus,

$$\mathbf{x}(\mathbf{X}, 0) = \mathbf{X}, \ \mathbf{v}(\mathbf{X}, 0) = \mathbf{0}, \ \theta(\mathbf{X}, 0) = \theta_0, \ \dot{\theta}(\mathbf{X}, 0) = 0, \ \rho(\mathbf{X}, 0) = \rho_0,$$
$$\boldsymbol{\sigma}(\mathbf{X}, 0) = \mathbf{0}, \ \varepsilon_e^p(\mathbf{X}, 0) = 0, \ f(\mathbf{X}, 0) = f_0(\mathbf{X}), \ \mathbf{X} \in \Omega. \tag{1.21}$$

Here Ω is the region occupied by the body in the reference configuration.

Let the boundary $\partial\Omega$ be divided into two parts, Γ_t and Γ_v. On Γ_v the positions of material particles are given as functions of time, and the tractions on Γ_t are specified as functions of time. The entire boundary is taken to be thermally insulated. Thus,

$$T_{i\alpha}N_\alpha = \bar{t}_i \text{ on } \Gamma_t, \ x_i = \bar{x}_i \text{ on } \Gamma_v, \ Q_\alpha N_\alpha = 0 \text{ on } \partial\Omega. \tag{1.22}$$

All of the simulations conducted in Chapters 2 through 5 obey this set of initial and boundary conditions. More specific boundary conditions for each individual case, such as the location of Γ_t and Γ_v and the velocity and traction specifications, are given in the respective chapters.

1.2.4 Semi-discrete Formulation of the Problem

Equations (1.6), (1.8) and (1.3) imply that the balance of moment of momentum (1.3) is identically satisfied. The present mass density can be computed from equation (1.1) if the deformation gradient and the current value of the porosity are known. However, here the present mass density at a node is determined along with other unknowns. Thus, the dependent variables to be solved for are $\mathbf{x}$, ρ, f and θ and the independent variables are $\mathbf{X}$ and t. Equations (1.18) and (1.19) are second-order coupled non-linear hyperbolic partial differential equations for $\mathbf{x}$ and θ. These can not be written explicitly in terms of $\mathbf{x}$ and θ since $\mathbf{T}$ is given by (1.8) and $\boldsymbol{\sigma}$ by (1.6) which involves $\mathbf{D}^p$ and θ. In order to solve the problem numerically by the FE method, we first derive its weak or variational formulation.

Let $\mathbf{w}(\mathbf{X})$ be a smooth function that is an analog of virtual velocity. We take the inner product of equation (1.18) with $\mathbf{w}$, integrate the resulting equation over the region Ω occupied by the body in the reference configuration, and use the divergence theorem to arrive at

$$\int_\Omega \alpha_I (1 - f_0) \dot{v}_i w_i d\Omega = -\int_\Omega w_{i,\alpha} T_{i\alpha} d\Omega + \int_{\Gamma_t} w_i \bar{t}_i d\Gamma. \tag{1.23}$$

Let $\psi_1, \psi_2, \ldots, \psi_n$ be FE basis functions defined on Ω. We write

$$v_i = \sum_{A=1}^{\text{nodes}} \psi_A(\mathbf{X})\tilde{v}_{Ai}(t), \ w_i = \sum_{A=1}^{\text{nodes}} \psi_A(\mathbf{X})c_{Ai}, \ i = 1, 2. \tag{1.24}$$

Here $\tilde{\mathbf{v}}$ is the vector of velocities of nodes, and c_{Ai}'s are constants. Substituting from (1.24) into (1.23) and exploiting the fact that the resulting equation must hold for all choices of $\mathbf{c}$'s we get

$$\mathbf{M}\dot{\tilde{\mathbf{v}}} = -\mathbf{F}^{\text{int}} + \mathbf{F}^{\text{ext}},$$

$$M_{AB} = \int_\Omega \alpha_I(1 - f_0)\psi_A\psi_B d\Omega, \tag{1.25}$$

$$F_{Ai}^{\text{int}} = \int_\Omega \psi_{A,\alpha}T_{i\alpha}d\Omega, \ F_{Ai}^{\text{ext}} = \int_{\Gamma_t} w_i\bar{t}_i d\Gamma.$$

In order to derive a weak form of equation (1.19) we first introduce an auxiliary variable

$$\xi = \dot{\theta}, \tag{1.26}$$

and follow the same procedure as that used to derive equation (1.25) with the following result.

$$\dot{\boldsymbol{\theta}} = \tilde{\boldsymbol{\xi}},$$

$$\tau\mathbf{H}\dot{\tilde{\boldsymbol{\xi}}} + \mathbf{H}\tilde{\boldsymbol{\xi}} = \mathbf{F}^\theta + \tilde{\mathbf{Q}}, \tag{1.27}$$

where

$$H_{AB} = \int_\Omega \rho_0(1 - f_0)\psi_A\psi_B d\Omega,$$

$$F_A^\theta = \int_\Omega \alpha_t\left(1 - \frac{3}{2}f\right)\theta_{,\alpha}\psi_{A,\alpha}d\Omega, \tag{1.28}$$

$$Q_A = \int_\Omega \psi_A J \operatorname{tr}(\boldsymbol{\sigma}\mathbf{D}^p)d\Omega.$$

Note that the natural boundary condition of zero heat flux has been embedded in equation (1.27).

We solve equation (1.16) for $\dot{\varepsilon}_e^p$ in terms of σ_y, ε_e^p and θ and derive its weak form in the same way as before except that the divergence theorem is not used. Recall that $\dot{\varepsilon}_e^p > 0$ only when a material point is deforming plastically as signified by the satisfaction of equation

(1.10); otherwise $\dot{\varepsilon}_e^p = 0$. Weak forms of equation (1.6), (1.14) and

$$\dot{\mathbf{x}} = \mathbf{v}(\mathbf{X}, t) \tag{1.29}$$

are also derived. We thus get coupled nonlinear ordinary differential equations

$$\dot{\mathbf{d}} = \mathbf{F}, \tag{1.30}$$

where $\mathbf{d}$ is the vector of unknowns and $\mathbf{F}$ is the force vector that depends upon time t and $\mathbf{d}(t)$. The thirteen unknowns at a node are $\{x_1, x_2, v_1, v_2, \sigma_{11}, \sigma_{22}, \sigma_{12}, \sigma_{33}, f, \theta, \xi, \varepsilon_e^p, \rho\}$.

1.2.5 Implementation

A computer code based on the semidiscrete formulation was developed using 4-node quadrilateral elements. Spatial integration is accomplished over each element using 2×2 Gaussian quadrature. Spatial variation in material properties is embedded in the integration by using local values at each quadrature point. Natural boundary conditions are embedded in equation (1.30); suitable modifications to the equations are made to enforce prescribed velocity components on Γ_v. Equation (1.30) is then integrated using the Livermore Solver for Ordinary Differential Equations (LSODE); parameter MF in LSODE is set to 10, which implies an Adams-Moulton method. The absolute and relative tolerances in LSODE are set to 10^{-7}. LSODE adaptively adjusts the timestep in order to compute the solution to within the desired accuracy. It should be noted that LSODE is freely available on the internet in both Fortran and C++ variants.

The computer code was validated by comparing computed results for several problems with their published analytical and numerical solutions and was also validated by the method of manufactured solutions. In this method, body forces and sources of internal energy density are found for any assumed deformation and temperature fields so that the governing equations are satisfied. These fields are input into the code. The computed solution should match the presumed analytical solution to a high degree of accuracy; see the material following equation (20) in Batra and Liang [78] for an example. Furthermore, the solution for ASB initiation and propagation in a homogeneous body coincided with Batra and Lear's [73] solution obtained with triangular elements.

1.2.6 Simulation of Crack Propagation

In order to simulate crack initiation and propagation, we assume that as soon as a failure criterion is met at a node, say N, an additional node N^*, coincident with N but not connected

to it, is added to the FE mesh. The node N^* is connected to the node N^{**} that has the next highest value of the critical parameter that determines the crack initiation. The elements are adjusted such that all nodes originally connected to N on one side of the newly formed crack are connected to N^* instead. Thus lines NN^* and N^*N^{**} overlap at the instant of the initiation of fracture. Note that no new element is created; however, a node is added, the element connectivity is modified and the number of unknowns is increased. Subsequent deformations of the body will either move N and N^* apart thereby creating a gap between them, or tend to push them together which may be accompanied by relative sliding between them. In the former case, surface tractions and the normal component of the heat flux are assumed to be null on the crack surfaces. In the latter case, the contacting surfaces are designated as master and slave, and the minimum distance of a node on the slave surface from the master surface is determined. If interpenetration occurs, then a Lagrange multiplier-based conjugate gradient method is used to compute the minimum force to be applied to the slave node and the master line segment in order to prevent interpenetration. One returns to the previous time step and applies loads determined by the contact algorithm; this technique is usually called predictor-corrector and has been described by Zywicz and Puso [79], and Carpenter et al. [80]. During contact, this algorithm is computationally expensive, as it requires each timestep to be taken twice. However, the contact detection algorithm is fast, requiring little overhead during non-contact timesteps. Furthermore, it is independent of which master segment a node on the slave surface penetrates, gives the minimum normal tractions between contacting surfaces (unlike less-expensive penalty methods), and permits their relative sliding. Batra and Lear [81] used a penalty-type method to compute the normal force to be applied to contacting nodes in order to avoid interpenetration.

Chapter 2

Equivalent Thermoelastoviscoplastic Parameters for Tungsten Heavy Alloy Particulate Composites

2.1 Problem Statement

In this chapter, we seek to determine the effective thermoelastoviscoplastic properties for WHA particulate composites. These composites consist of nearly spherical tungsten particulates, between 30 and $70\mu m$ in diameter, embedded in a nickel-iron matrix. We utilize a representative volume element (RVE) indicative of the microstructure of the composite; this RVE is subjected to a variety of thermomechanical tests in order to find stress-strain curves. These curves are used to estimate strain- and strain-rate hardening and thermal softening parameters for the composite. The effects of RVE size, particulate distribution, particulate diameter, and volume fraction of the particulate are considered.

2.2 Numerical Tests

2.2.1 Initial and Boundary Conditions

Utilizing the FE code described in Section 1.2, a square RVE with side length H is subjected to what will be referred to as a "constant area plane strain tension test". The body is taken to be initially at rest, stress-free, at a uniform temperature, with no initial porosity (as indicated in Section 1.2.3). Furthermore, porosity evolution is assumed to be zero; thus, the body is always porosity free, giving a von Mises yield surface. The heat produced by plastic working is also assumed to be zero. The upper surface of the body is given a constant
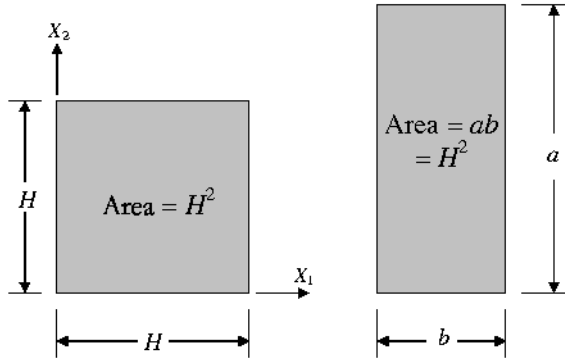
Figure 2.1: Sketch of constant-area plane-strain deformation used for homogenization

velocity v_0 in the X_2 direction after a short ramp time of $1\mu s$. The lower surface of the body is held fixed in the X_2 direction and is allowed to slide frictionlessly in the X_1 direction. The lateral surfaces are prescribed a velocity such that the area of the rectangle remains a constant H^2, as shown in Figure 2.1. This choice of deformation is somewhat arbitrary; however, it does guarantee that the shape of the boundary remains well-defined, despite the inhomogeneous nature of the RVE. Also, the area-preserving nature of the RVE is consistent with the incompressibility assumption made with the von Mises yield surface, making this deformation admissible for large plastic deformations.

2.2.2 Rule of Mixtures

According to this rule, the value P of a material parameter for a mixture comprised of two constituents with volume fractions V_1^f and V_2^f and values P_1 and P_2 of the material parameter is given by

$$P = V_1^f P_1 + V_2^f P_2 = (1 - V_2^f)P_1 + V_2^f P_2. \tag{2.1}$$

It gives exact values of the mass density and the heat capacity and often gives an upper bound for values of other material parameters for the composite.

2.2.3 Homogenization Techniques

Determination of elastic and viscoplastic parameters from a series of thermomechanical deformations of an RVE is a non-trivial task. In a macro-scale analysis, the RVE itself is small

enough to be considered a material point; that is, one could consider it having uniform material properties as well as a single stress and strain states. Thus, an effective stress and strain tensor for the deformation of the RVE should be defined. While analyzing deformations of a RVE it has been assumed that the two materials are perfectly bonded together at their common interfaces.

For the constant-area plane-strain biaxial tension/compression deformation described in Section 2.2.1, we define the Cauchy stress tensor as follows: recalling that the length in the x_3 direction is taken to be one, σ_{22} is the normal load divided by the present length of the top and bottom edges, σ_{11} is the normal load divided by the present length of the lateral edges, σ_{12} is the tangential load divided by the present length for all four edges (which is, not surprisingly, nearly zero for this deformation), and σ_{33} is the total load in the x_3 direction divided by the current area perpendicular to the x_3 axis.

Large deformations require the definition of a suitable strain tensor. The deformation described in Section 2.2.1 results in the initial square being deformed into a rectangle. For a homogeneous material, this would be a homogeneous deformation; so, for homogenization purposes, we assume that $F_{11} = H/a$, $F_{22} = a/H$, and $F_{33} = 1$, where a is the current x_2 coordinate of the top surface (as shown in Figure 2.1), and the strain tensor is then defined as:

$$\varepsilon_{ij} = (\delta_{ij} - B_{ij}^{-1})/2 \tag{2.2}$$

Here $B_{ij} = F_{i\alpha}F_{j\alpha}$ is the left Cauchy-Green tensor. Note that the tensor $\boldsymbol{\varepsilon}$ is equivalent to the small-strain tensor for infinitesimal deformations. The von Mises effective stress can be computed as in equation $(1.10)_2$, and the effective strain is taken to be $\varepsilon_e = \sqrt{\frac{3}{2}\varepsilon_{ij}\varepsilon_{ij}}$. Initial numerical analyses are conducted such that no heat is generated during plastic working; that is $\dot{\theta} = 0$. Therefore, the thermal and mechanical properties are divorced and can be treated separately. Furthermore, no porosity generation is allowed, reducing Gurson's yield surface (equation $(1.10)_1$) to the more familiar von Mises yield surface.

Elastic Parameters

Determination of Young's modulus and Poisson's ratio is relatively simple using the definitions of the stress and strain tensors in the previous section. For metals, deformations in the elastic regime are relatively small (strains < 1%), so one may use classical linear elasticity

17
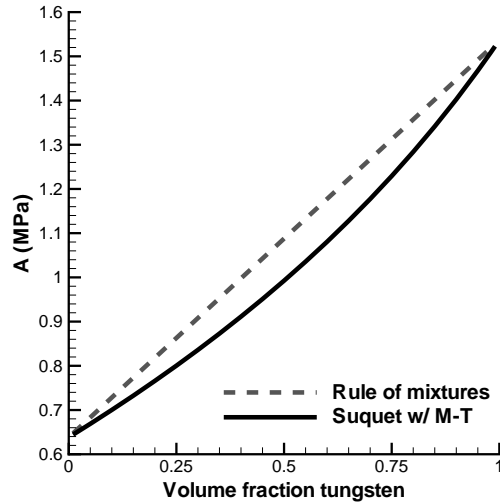
Figure 2.2: Comparison of yield stress estimates from the rule of mixtures and Suquet's method using the Mori-Tanaka estimate for the shear modulus

relations. For plane strain deformations of isotropic linear elastic materials:

$$\varepsilon_{11} = \frac{1}{E}[\sigma_{11} - \nu(\sigma_{22} + \sigma_{33})], \tag{2.3}$$

$$\varepsilon_{22} = \frac{1}{E}[\sigma_{22} - \nu(\sigma_{11} + \sigma_{33})], \tag{2.4}$$

$$\varepsilon_{33} = 0 = \frac{1}{E}[\sigma_{33} - \nu(\sigma_{11} + \sigma_{22})] \tag{2.5}$$

With the results from a constant-area plane strain tension test, equation (2.5) can be solved directly for Poisson's ratio, ν. Using this result, one can compute Young's modulus from either (2.3) or (2.4). The other offers an excellent check on the isotropy of the particulate arrangement.

Strain- and Strain-Rate Hardening

Determination of the quasi-static yield stress A and the strain hardening parameters B and n in the Johnson-Cook relation is difficult from an examination of an effective stress versus effective strain curve. For a given material, there are several different sets of parameters that produce very close stress-strain curves. The onset of yielding (corresponding to an effective stress of A in a quasi-static test) is not readily apparent when examining the stress-strain curve or its derivative because the strain-rate hardening term in the Johnson-Cook relation prevents a noticeable change in the slope of the curve at the yield strain. Figure 2.2 compares

values of A computed from the rule of mixtures with that obtained from Suquet's [6] relation, with the effective shear modulus obtained from the Mori-Tanaka [2] relation. We have chosen to estimate A of the composite using the rule of mixtures. Conducting a plane-strain tension test (as described in Section 2.2) at an effective strain-rate close to the reference strain rate $\dot{\varepsilon}_0$ then allows the determination of the yield strain from the estimated value of A; the effective plastic strain ε_e^p is then defined as the effective strain minus the strain at yield. Plotting $\log(\sigma_y - A)$ versus $\log(\varepsilon_e^p)$ allows the determination of B and n from a simple linear least squares fit. Through numerical tests it was shown that the use of a different homogenization technique for determining A, such as the method proposed by Suquet [6], produces quantitatively different values for B and n, but the resulting stress-strain curve is effectively the same.

The effective strain-rate hardening coefficient C can be determined by examining two tests performed at different effective strain-rates on the same RVE. We have taken the reference strain-rate $\dot{\varepsilon}_0$ to be the same for the two constituents and the composite. Given the stress-strain curve for the two different tests, the value of C can be calculated using equation (2.6)

$$C = \frac{1 - \frac{\sigma_{y1}}{\sigma_{y2}}}{\frac{\sigma_{y1}}{\sigma_{y2}}ln(\frac{\dot{\varepsilon}_2}{\dot{\varepsilon}_0}) - ln(\frac{\dot{\varepsilon}_1}{\dot{\varepsilon}_0})}. \tag{2.6}$$

Here σ_{y1} and σ_{y2} are the stresses at an arbitrary strain during tests at strain-rates of $\dot{\varepsilon}_1$ and $\dot{\varepsilon}_2$, respectively.

Thermal Softening

Thermal softening in the Johnson-Cook relation is governed by θ_m, the melting temperature of the material, and m, a thermal exponent. Note that as the temperature approaches θ_m, the stiffness of the material approaches zero. Here we assume that the thermal exponent m equals 1 for both constituents and the composite, as it is nearly equal to 1 for most materials.

To determine the effective melting temperature of the composite, we conduct plane strain tension tests at different uniform temperatures. As in the other tests, plastic working does not contribute to temperature rise; initial attempts at relaxing this assumption resulted in transient, non-constant temperature fields in the RVE which were dependent on the effective strain-rate of the test, making it difficult to assign an effective temperature to the RVE. Given the uniform temperature, the ratio of stresses at a given effective plastic strain for two tests with different temperatures allows one to simply determine the effective melting

temperature for the composite from equation (2.7)

$$\theta_m = \frac{\frac{\sigma_{y1}}{\sigma_{y2}}\theta_2 + \theta_1}{1 - \frac{\sigma_{y1}}{\sigma_{y2}}}. \tag{2.7}$$

Here σ_{y1} and σ_{y2} are the stresses at an arbitrary strain during tests at temperatures of θ_1 and θ_2, respectively.

It is important to note that the "melting temperature" of the composite governs its thermal softening, but has no physical significance. The actual melting temperature of the composite would equal the lowest melting temperature among the constituents.

Thermal Conductivity

The effective thermal conductivity of the composite is determined by applying a constant temperature differential across two opposite edges of the RVE. The average heat flux on those edges is divided by the applied temperature gradient, giving an effective thermal conductivity. Ideally, one would have a microstructure that gives an isotropic thermal conductivity; in practice, this is difficult. The average of the computed thermal conductivity in the X_1 and X_2 directions is taken to be the effective thermal conductivity.

Coefficient of Thermal Expansion

The effective coefficient of thermal expansion of the composite is computed by constraining the RVE on the edges in the normal direction (as well as the plane strain constraint) and applying a uniform temperature rise over the entire RVE. Given that the resulting stresses are below the yield stress, the effective coefficient of thermal expansion is computed by equation (2.8):

$$\hat{\alpha} = \frac{-\sigma_{kk}}{9K\Delta T}. \tag{2.8}$$

Here, K is the *effective* bulk modulus of the material and ΔT is the temperature rise; K is computed from E and ν. Note that it is assumed that the coefficient of thermal expansion is a scalar, tacitly assuming an isotropic material.

2.3   Computation and Discussion of Results

2.3.1   Tungsten Heavy Alloys

The particulate composite that we have considered is composed of tungsten particulates dispersed in a nickel-iron matrix. When the volume fraction of tungsten exceeds 50%, the

composite is frequently referred to as a tungsten heavy alloy (WHA); these materials are being considered as a replacement for depleted uranium in armor penetration applications due to their high density and strength. Pure tungsten is undesirable in this application due to its brittleness; the addition of the nickel-iron to the matrix provides some ductility while allowing the composite to retain some of the strength and density of tungsten. Listed in Tables 2.1 and 2.2 are the properties of the constituents, as given in Stevens and Batra [82].

For both materials, the thermal relaxation time was taken to be $\tau = 10^{-8}$ sec. The thermal softening exponent m was taken to be 1.

Note that nickel-iron exhibits significantly higher strain- and strain-rate hardening and thermal softening than tungsten. Numerical tests have shown that nickel-iron is significantly less susceptible to shear band formation than tungsten [83].

Table 2.1: Elastic and thermal properties for W and NiFe

Material	E (GPa)	ν	ρ (kg/m^3)	κ (W/m K)	$\hat{\alpha}$ (x10^{-6}/K)	c (J/kg K)
W	400	0.29	19300	160	5.3	138
NiFe	255	0.29	9200	100	15.0	382

Table 2.2: Viscoplastic properties for W and NiFe

Material	A (MPa)	B (MPa)	n	C	$\dot{\varepsilon}_0$ (1/s)	θ_m (K)
W	730	562	0.0751	0.0290	1.4x10^{-13}	1700
NiFe	150	546	0.2080	0.0838	6.7x10^{-14}	1225

2.3.2   Verification of Homogenization Methods

In an attempt to verify the plausibility and accuracy of the homogenization methods described in Section 2.2.3, we examined deformations of a pure tungsten specimen of square cross section of length $H = 0.25$ mm. The reference strain-rates listed in Table 2.2 are far too slow to allow numerical tests without significant strain-rate effects, so the reference strain-rate needs to be altered. If the reference strain-rate above is denoted by $\dot{\varepsilon}_0$ and the new reference strain-rate is denoted by $\dot{\varepsilon}_1$, then the Johnson-Cook viscoplastic relation (equation

1.16, without thermal effects) gives

$$\sigma_y = (A + B(\varepsilon_e^p)^n) \left(1 + C \, ln \left(\frac{\dot{\varepsilon}_e^p}{\dot{\varepsilon}_0} \right) \right)$$

$$= (A + B(\varepsilon_e^p)^n) \left(1 + C \, ln \left(\frac{\dot{\varepsilon}_e^p}{\dot{\varepsilon}_1} \frac{\dot{\varepsilon}_1}{\dot{\varepsilon}_0} \right) \right)$$

$$= (A + B(\varepsilon_e^p)^n) \left(\left(1 + C \, ln \left(\frac{\dot{\varepsilon}_e^p}{\dot{\varepsilon}_1} \right) \right) \left(1 + C \, ln \left(\frac{\dot{\varepsilon}_e^p}{\dot{\varepsilon}_1} \right) \right) - C^2 \, ln \left(\frac{\dot{\varepsilon}_e^p}{\dot{\varepsilon}_1} \right) \, ln \left(\frac{\dot{\varepsilon}_e^p}{\dot{\varepsilon}_0} \right) \right).$$

Assuming that $C << 1$, neglecting the term containing C^2 allows A and B to be computed at the new reference strain-rate

$$A^* = A \left(1 + C \, ln \left(\frac{\dot{\varepsilon}_1}{\dot{\varepsilon}_0} \right) \right), \; B^* = B \left(1 + C \, ln \left(\frac{\dot{\varepsilon}_1}{\dot{\varepsilon}_0} \right) \right). \tag{2.9}$$

This modification to the material properties produces a slight error (due to the omission of the C^2 term); however, this error is of the order of 1 to 2 percent, far lower than the accuracy level of the material parameters themselves. The modified values of A and B are listed in Table 2.3.

Table 2.3: Modified values of A and B for a reference strain-rate of 5000 1/s

Material	A (MPa)	B (MPa)	$\dot{\varepsilon}_0$ (1/s)
W	1536.9	1183.2	5000
NiFe	638.4	2323.6	5000

With the modified material parameters, the pure tungsten RVE was subjected to tests with nominal axial strain-rates of 2500, 5000, 25000, and 50000 1/s, and additional 50000 1/s tests were conducted at temperature rises of 100, 200, 500, and 1000 K. Additionally, uniform FE meshes of 40 by 40, 60 by 60, and 80 by 80 elements were tested and gave identical results for the pure tungsten sample. Using the data from these tests, the effective material parameters for tungsten were computed using the homogenization techniques; the results are listed in Table 2.4, along with the percent error from the input values.

Table 2.4: Values obtained from homogenization procedure for pure tungsten

	E (GPa)	ν	B (MPa)	n	C	θ_m (K)	κ (W/mK)	$\hat{\alpha}$ (10^{-6}/K)
homog. values	405.94	0.2907	1189.4	0.07813	0.02877	1708	160.0	5.27
% error	1.49%	0.24%	0.52%	4.03%	1.03%	0.47%	~0%	0.57%

Note that the quasi-static yield stress A was assumed to be 1536.9 MPa, which was the input value. The accuracy of the homogenization method is excellent, producing less than 4% error for all of the homogenized values. Use of different strain-rate and temperature tests resulted in slight differences in the computed values of C and θ_m; it was found that using a large ratio of strain-rates and a large temperature rise produced more accurate results.

2.3.3 Representative Volume Element Size

The appropriate size for the RVE is dependent on the microstructure of the material in question. Typical WHAs have tungsten particulates with diameters of ~ 50 μm arranged randomly, such that the bulk material is isotropic. An RVE must capture a sufficient number of particulates to give an accurate volume fraction of material and give a roughly isotropic response.

In order to investigate this effect, four RVEs were created with side lengths of $H =$ 0.15, 0.25, 0.35, and 0.50 mm. The FE mesh density was kept constant, with each element measuring 5 μm by 5 μm. Each RVE consists of 50 μm tungsten particulates distributed randomly to give a volume fraction of tungsten equal to 50%. Each of the RVEs was subjected to a plane-strain tension test and then re-tested after a 90 degree rotation, to insure that the distribution gave nearly isotropic results. Shown in Figure 2.3 are all four RVEs and the effective stress versus effective strain curves for each. All four of the curves agree pointwise to within 1%. The 0.25 mm RVE was chosen for the remainder of the analyses, and the effective stress versus the effective strain curve obtained from it is referred to as the standard stress strain curve (the deviations in Figure 2.3 are normalized with respect to the 0.25 mm RVE's result).

2.3.4 Finite Element Mesh Density

To test the effects of the mesh density on the homogenization results, a 0.25 mm RVE consisting of 50% volume fraction tungsten particulates of diameter 50 μm was tested with four different uniform meshes: 40×40, 50×50, 60×60 and 80×80 elements. Figure 2.4 shows the RVE and the deviations of the other three meshes from the standard 50×50 mesh. Note that the mesh density does not play a strong role in influencing the homogenization results. The 50×50 mesh was chosen for the remainder of the analyses.
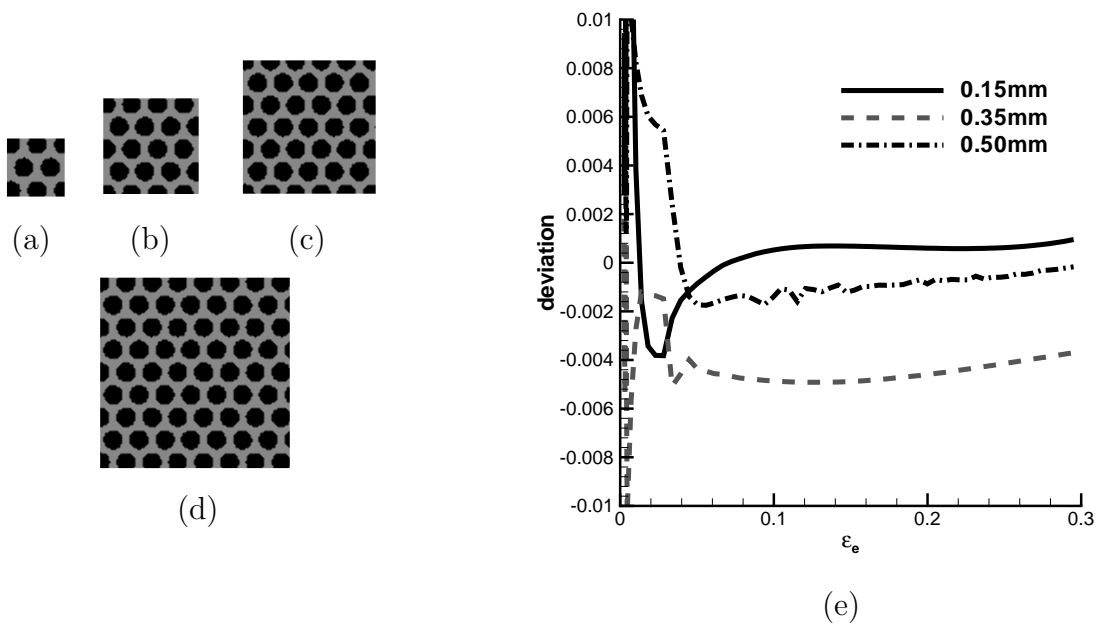
Figure 2.3: 50% volume fraction tungsten RVEs with $H =$ (a) 0.15 mm, (b) 0.25 mm, (c) 0.35 mm, and (d) 0.50 mm, and (e) the deviation in the effective stress versus effective strain curve for $H = 0.15$ mm, 0.35 mm, and 0.50 mm from that for $H=0.25$ mm
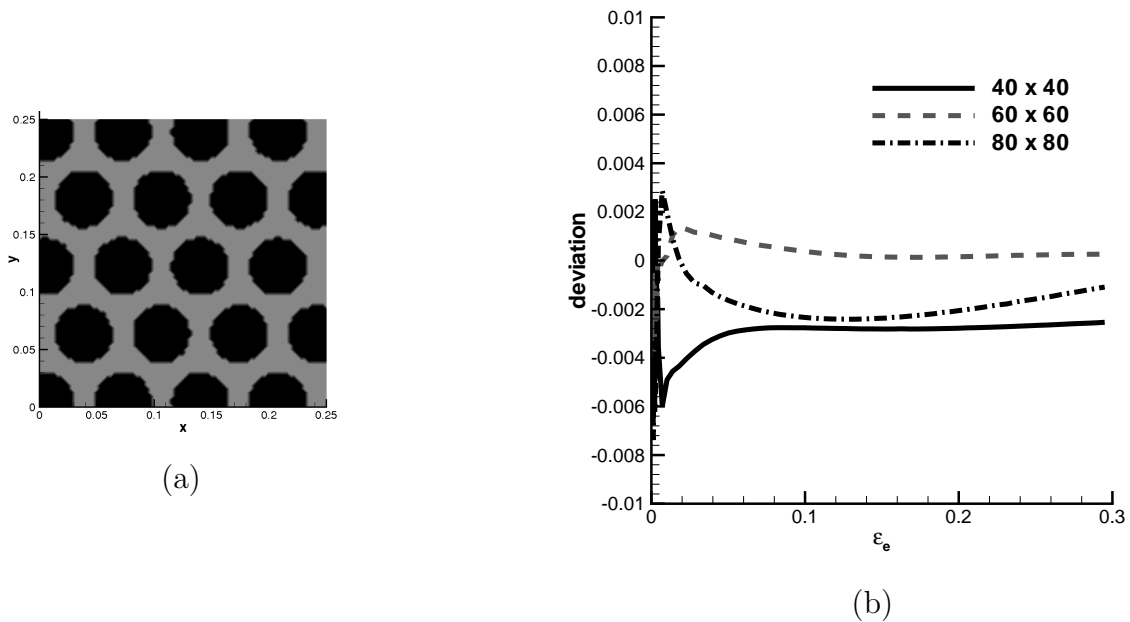
Figure 2.4: Finite element mesh density test: (a) 0.25 mm square 50% volume fraction tungsten RVE, (b) the deviations from the stress-strain curve for the 40 × 40, 60 × 60, and 80 × 80 FE meshes from those for the 50 × 50 mesh
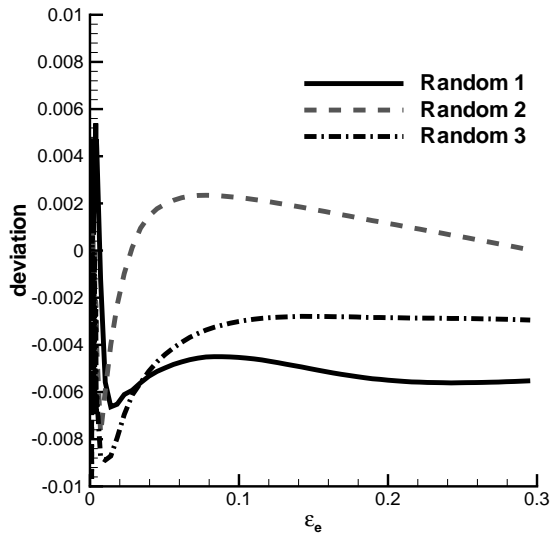
Figure 2.5: Deviations in the stress-strain curve from the ordered particulate arrangement for three different random distributions of 50 μm particulate
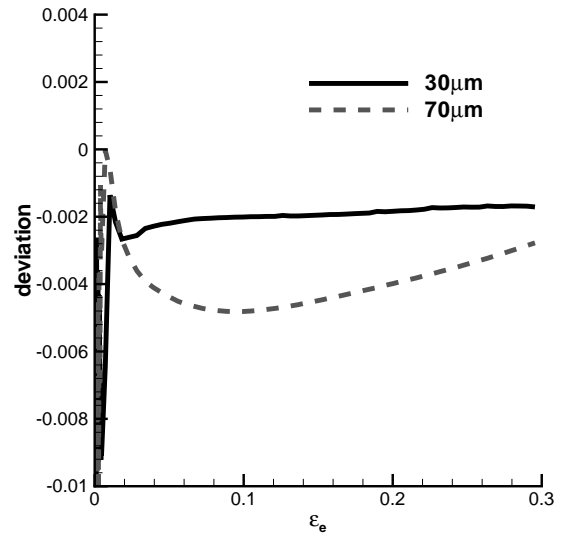
Figure 2.6: Deviations in the stress-strain curve from the 50 μm particulate distribution for the 30 μm and 70 μm distributions

2.3.5   Particulate Arrangement

The arrangement of the particulates in the RVE could possibly have an effect on the values of the homogenized parameters. Most WHAs exhibit isotropic behavior, so the arrangement of the particulates must be such that the overall response is independent of direction. To examine this effect, four RVEs with 50% volume fraction of 50 μm tungsten particulates were tested; the first with the particulates centered on the vertices of equilateral triangles and the remaining three with different random dispersions of particulates. The deviations of stress-strain curves for these four cases are shown in Figure 2.5, with the reference curve taken to be that for the ordered arrangement. No effect of particulate arrangement is seen in the overall stress-strain curve.

2.3.6   Particulate Size

Figure 2.6 shows the deviation in the stress-strain curves from the testing of three RVEs with 50% volume fraction of tungsten particulates, each test with a different diameter of particulate: 30, 50 and 70 μm. The reference curve was taken to be the 50 μm particulate case. One can see no discernible effect of particulate size from this analysis.

2.3.7 Volume Fraction of Constituents

Of primary interest to material designers and engineers is the effect of the volume fraction of the particulate on the homogenized material parameters. Results from Sections 2.3.3 and 2.3.4 give an indication of the appropriate RVE size and the FE mesh to study the problem. Sections 2.3.5 and 2.3.6 demonstrate that the particulate size and distribution have little effect on the response of the RVE. With these guidelines, a 0.25×0.25 mm RVE meshed with 2500 uniform square elements is studied, using 50 μm diameter particulates centered on the vertices of equilateral triangles. The distance between the particulates is adjusted to give volume fractions between 50 and 80%. Less than 50% volume fraction is of little interest to designers; greater than 80% volume fraction is difficult to achieve with circular particulates. Each RVE was subjected to plane-strain tension tests at nominal axial strain-rates of 5000 and 50000 1/s. Additionally, the RVE was tested at 50000 1/s with temperature rises of 200 and 500K.

Elastic Parameters

Figure 2.7 shows Young's modulus as a function of volume fraction of tungsten. The rule of mixtures and the Mori-Tanaka estimates are plotted as a reference. The Mori-Tanaka estimate, as shown by Weng [3], assumes randomly distributed spherical particulates; this plane-strain analysis assumes particulates to be cylinders. Despite the non-isotropic arrangement (if one considers the x_3 direction), the homogenization estimate is quite reasonable. The Poisson's ratio of the composite matched the Poisson's ratio of the constituents within 1% for all volume fractions.

Strain Hardening Parameters

The variation of B and n with volume fraction of tungsten is shown in Figures 2.8 and 2.9, respectively. The homogenization procedure predicts slightly higher values for B and n than the rule of mixtures, but the slope is nearly the same as that of the rule of mixtures.

Strain-Rate Hardening Parameters

The strain-rate hardening coefficient C was determined for each of the volume fractions at effective plastic strains of 5% through 30%. Figure 2.10 shows the value of C at 5% effective plastic strain for each of the volume fractions. The homogenization results are similar to the rule of mixtures. It is important to note that the value of C is different over the range of strains studied. Figure 2.11 shows C as a function of effective strain ε_e for each of the tested volume fractions.
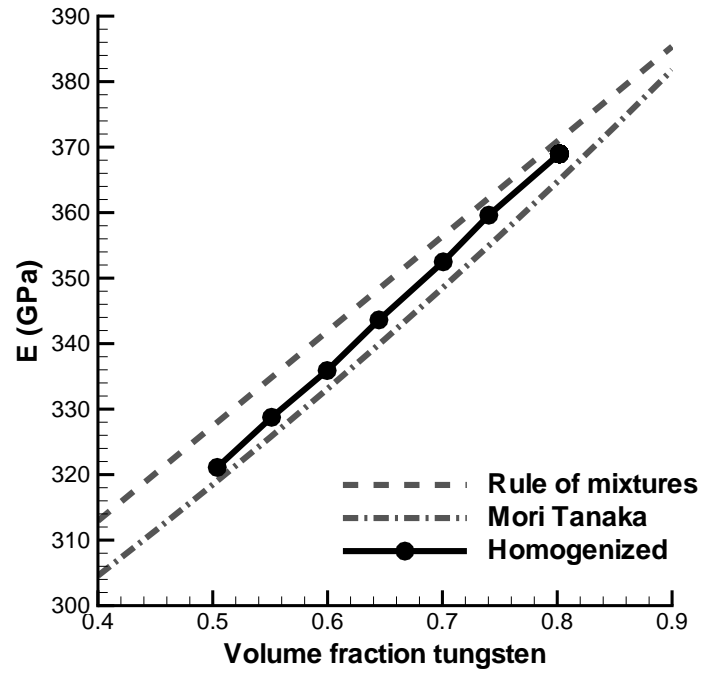
Figure 2.7: Effective Young's modulus as a function of volume fraction of tungsten particulates
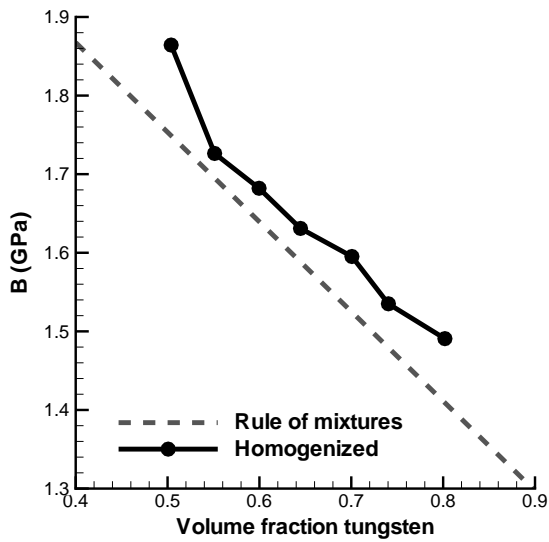
Figure 2.8: Strain hardening coefficient B as a function of volume fraction of tungsten particulates
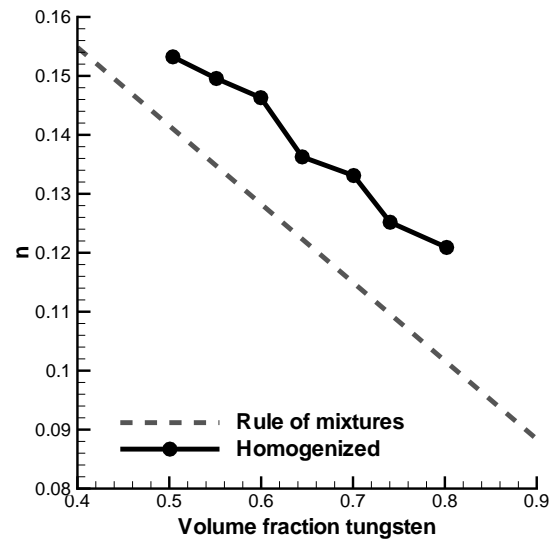
Figure 2.9: Strain hardening exponent n as a function of volume fraction of tungsten particulates
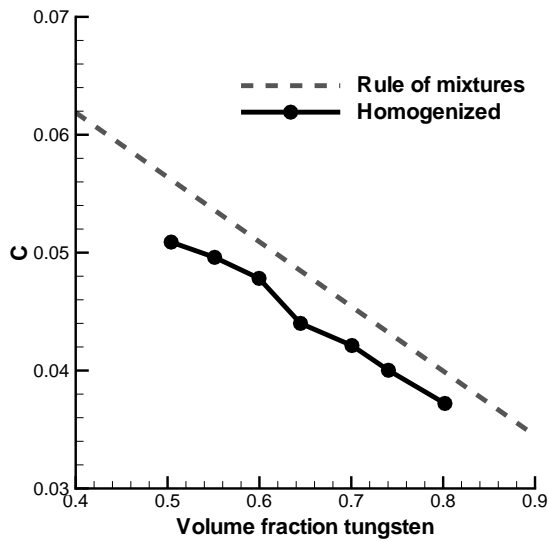
Figure 2.10: Strain-rate hardening co-efficient C as a function of volume fraction of tungsten particulates
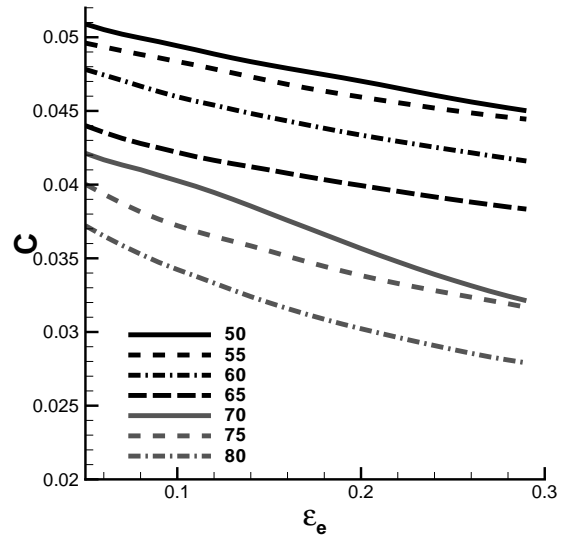
Figure 2.11: Strain-rate hardening exponent C as a function of effective plastic strain for different volume fractions of tungsten particulates

One possible explanation for the variation in C is the interaction between the particulates and the matrix. Nickel-iron is much softer than tungsten, so it constitutes most of the initial deformation. Also, it exhibits more strain-rate hardening; so initially, the strain-rate hardening value for the composite is maximum. As the strain increases, more of the tungsten is deformed plastically, lowering the overall strain-rate hardening. This effect is amplified by our choice of a constant value for B and n (dictated by the linear curve fit); realistically, B and n are also functions of strain. This variation with respect to strain is dictated by the microstructure of the material and is difficult to quantify. In order to simplify the model, B, n, and C are taken to be independent of strain for a given volume fraction, as given by Figures 2.8, 2.9, and 2.10.

Thermal Softening

Figure 2.12 shows the melting temperature as a function of volume fraction. The values indicated as $\Delta\theta = +200K$ are obtained by comparing the plane strain tension test at the reference temperature to a test with a temperature rise of 200K. The values indicated as $\Delta\theta = +500K$ were obtained from a test with a temperature rise of 500K. Note that there is a slight difference between the two lines. Figure 2.13 shows the variation in computed
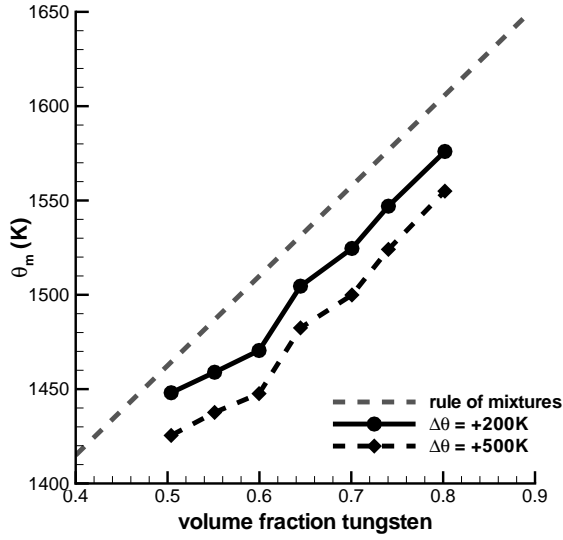
Figure 2.12: Melting temperature θ_m as a function of volume fraction of tungsten particulates
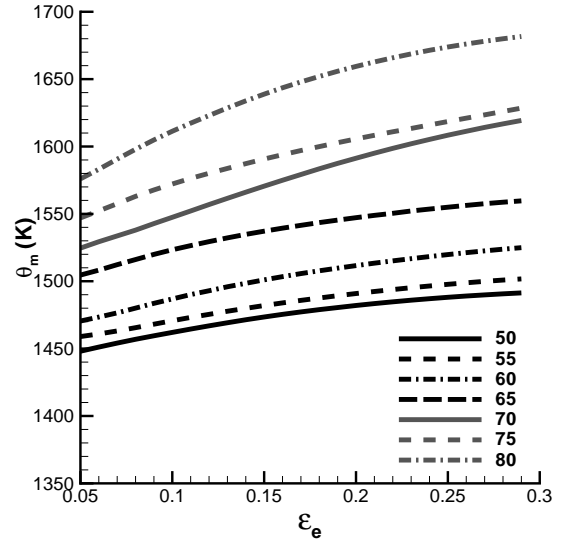
Figure 2.13: Melting temperature θ_m as a function of effective plastic strain for different volume fractions of tungsten particulates

melting temperature versus strain. There is a slight increase in melting temperature with strain, possibly for similar reasons as the strain-rate hardening case above.

Thermal Conductivity

Figure 2.14 shows the thermal conductivity as a function of volume fraction. The top and bottom surfaces of each RVE were held at constant temperature, with the top surface held at +100K over the bottom surface. The average heat flux in the X_2 direction was calculated at multiple values of $X_2 = $ constant using the local material parameters; this heat flux was nearly constant throughout the body after reaching steady-state conditions. The average heat flux divided by the overall temperature gradient (100K/0.25 mm) gave the values reported in Figure 2.14. The homogenized values are compared with the rule of mixtures and an approach given by Hatta and Taya [84].

It should be noted that each RVE was tested at both normal orientation and at a 90° rotation. For the tungsten/nickel-iron RVEs, the rotation made little difference in the results because of the small difference in thermal conductivity between the metals. Care must be taken when implementing this technique for systems with great disparity between the thermal conductivities of the constituents; thermally isotropic arrangements of such systems can be
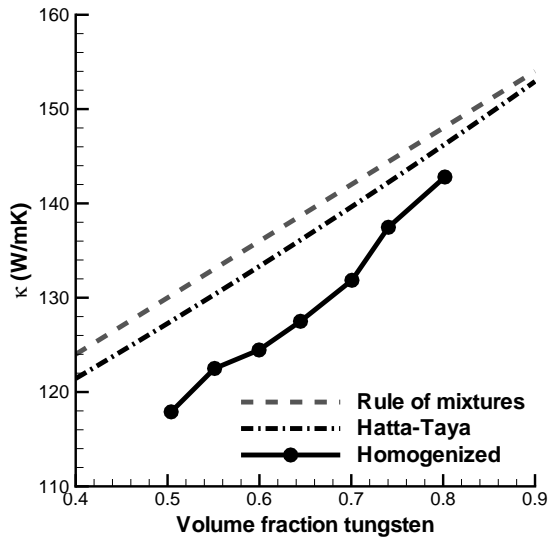
Figure 2.14: Thermal conductivity κ as a function of volume fraction of tungsten particulates

Figure 2.15: Coefficient of thermal expansion $\hat{\alpha}$ as a function of volume fraction of tungsten particulates

difficult to determine.

Coefficient of Thermal Expansion

The coefficient of thermal expansion as a function of volume fraction of tungsten is given in Figure 2.15. The edges of each RVE were held fixed as the body was given a uniform temperature rise of 50K. The average values of stress components were calculated as indicated in Section 2.2.3, and the homogenized value of the coefficient of thermal expansion was computed by equation (2.8). It should be noted that the bulk modulus used in equation (2.8) is the homogenized value of bulk modulus, obtained from the values of Young's modulus in Figure 2.7 and Poisson's ratio of 0.29. The average stress σ_{33} is slightly different from that of the in-plane stresses σ_{11} and σ_{22} due to the cylindrical particulates required by the plane-strain condition; however, the impact on the results is negligible. Note the excellent agreement between the homogenized results and those of the approach proposed by Hashin and Rosen [85].

Summary of Homogenized Material Parameters

Equations 2.10 through 2.18 give the homogenized material parameters as functions of the volume fraction of tungsten, v_f. A polynomial least squares fit was used with sufficient order

to capture the trends. Note that these relations are only valid in the range 50% to 80% volume fraction of tungsten.

$$\text{Young}'\text{s modulus (GPa)} : E = 241.76 + 155.03v_f + 4.53v_f^2, \qquad (2.10)$$

$$\text{Poisson}'\text{s ratio} : \nu = 0.29, \qquad (2.11)$$

$$\text{Yield stress} : A = 0.6384 + 0.8985v_f, \qquad (2.12)$$

$$\text{Strain hardening coefficient (GPa)} : B = 2.394 - 1.152v_f, \qquad (2.13)$$

$$\text{Strain hardening exponent} : n = 0.2126 - 0.1535v_f, \qquad (2.14)$$

$$\text{Strain rate hardening coefficient} : C = 0.07563 - 0.04794v_f, \qquad (2.15)$$

$$\text{Thermal conductivity (W/mK)} : \kappa = 76.24 + 81.63v_f, \qquad (2.16)$$

$$\text{Coefficent of thermal expansion} (\times 10^{-6}/\text{K}) : \alpha = 14.11 - 9.138v_f, \qquad (2.17)$$

$$\text{Melting temperature} (^{\text{o}}\text{C}) : \theta_m = 1214.1 + 447.1v_f. \qquad (2.18)$$

Listed in Table 2.5 are the maximum deviations of the homogenized values of each thermo-mechanical parameter from the rule of mixtures and corresponding micromechanical models.

Table 2.5: Maximum deviation of the homogenized material parameters from the rule of mixtures and micromechanical models

Quantity	Max. % deviation from the Rule of Mixtures	Micromechanical model	
		Name	Max. % deviation
E	-2.2%	Mori-Tanaka	1.2%
A	–	Suquet	5.9%
B	6.2%	–	–
n	13.7%	–	–
C	-10.4%	–	–
θ_m	-2.7%	–	–
κ	-10.5%	Hatta-Taya	-8.1%
α	-7.4%	Hashin-Rosen	-3.7%

2.3.8 Accuracy of Homogenization

In order to test the accuracy of the homogenization, a homogeneous material with material parameters found from the above homogenization techniques was subjected to a plane-strain tension test at 50000 1/s with a uniform temperature rise of 200K. The stress-strain curve was compared with a similar analysis performed on an RVE. Shown in Figure 2.16 is the result for the 80% volume fraction of tungsten case. The results of a similar test on a homo-
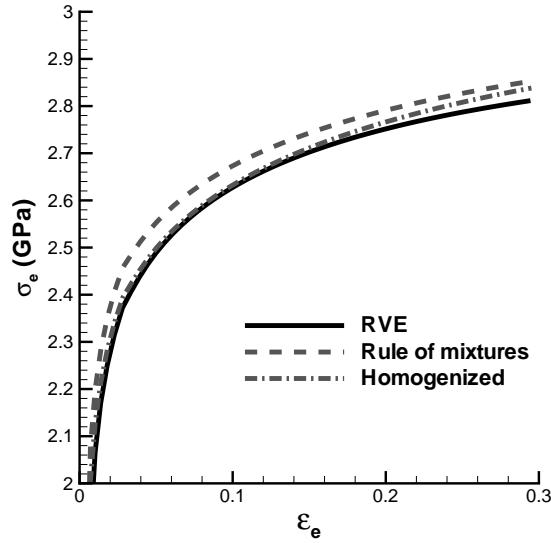
Figure 2.16: Effective stress versus effective strain curve for 80% volume fraction tungsten RVE and its equivalent homogeneous material

geneous material with the properties derived by the rule of mixtures is given for comparison. Note that the maximum point-to-point error for the homogenized material over the entire range of strains is 1.8%. For the 7 different volume fractions, the maximum point-to-point error was 2.2%, with the average point to point error being less than 0.5%. This level of accuracy is encouraging considering that the RVE is not truly isotropic due to the plane strain assumption and inertia effects were neglected in the homogenization procedure.

Loading and Unloading

During a more complicated analysis, material points may be loaded, unloaded, and possibly reloaded. To test the accuracy of the homogenization procedure, a RVE containing 60% volume fraction of tungsten and its equivalent homogeneous sample were subjected to the plane strain tension test as described in Section 2.2.3. However, the velocity on the upper surface was given a non-constant profile, given in equation (2.10).

$$v_2 = \begin{cases} v_0 t, 0 \leq t \leq 1\mu s, \\ v_0, 1 < t \leq 6\mu s, \\ -v_0 t, 6 < t \leq 8\mu s, \\ -v_0, t \geq 8\mu s \end{cases} \quad \text{on } X_2 = H. \tag{2.19}$$

Here the value of $v_0 = 12.5$m/s, corresponds to a nominal axial strain-rate of 50000 1/s.

32
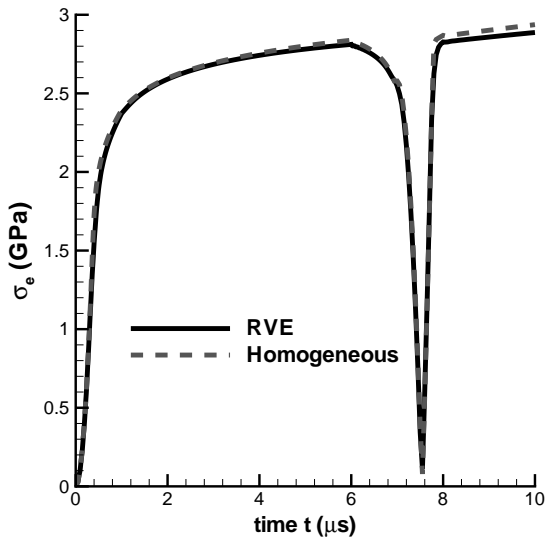
Figure 2.17: Effective stress versus time for plane strain tension unload/reload test for 60% volume fraction of tungsten RVE and its equivalent homogeneous material
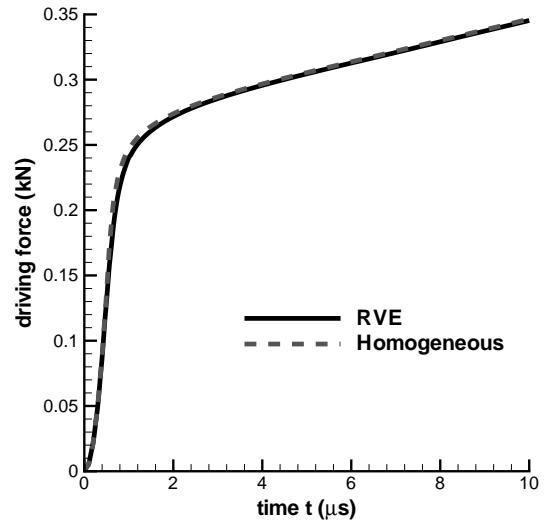
Figure 2.18: Driving force versus time in simple shear test for both 60% volume fraction of tungsten RVE and its equivalent homogeneous material

Shown in Figure 2.17 is a plot of effective stress versus time for both the homogeneous sample and the RVE. Note the excellent agreement, even after the body has been allowed to unload and then is reloaded.

Simple Shear

The homogenized material parameters are only accurate if the response of the homogeneous material compares well to that of the RVE under different types of loading. To test the homogenization technique, a 60% volume fraction tungsten RVE and a homogeneous sample with the homogenized properties are subjected to a simple shear test. The upper and lower surfaces are restrained in the x_2 direction and the upper surface is given velocity v_0 in the x_1 direction while the lower surface is given the velocity $-v_0$ in the x_1 direction. Here v_0 was chosen such that the effective strain-rate is approximately 25000 1/s. Figure 2.18 shows the the time-histories of driving force (the force in the x_1 direction on the upper surface) for the two cases. Note the excellent agreement between the two sets of curves.

2.4 Conclusions

We have developed a technique to find the thermoelastoviscoplastic properties of a metal-metal particulate composite. This technique was used to find the thermoviscoplastic parameters for the Johnson-Cook relation for a tungsten heavy alloy composed of tungsten particles suspended in a nickel-iron matrix. It was found that the rule of mixtures under-predicts the strain hardening parameters B and n, with the under-prediction of n by as much as 13%. Furthermore, the strain-rate hardening coefficient C was shown to vary with strain, possibly due to the two constituents being strained at different rates. The rule of mixtures over-predicts C by $\sim$10%. The thermal softening of the homogenized material, governed by the pseudo-melting temperature θ_m was found to be slightly less than that predicted by the rule of mixtures. A slight ($< 5\%$) variation in the melting temperature at different strains and temperature ranges was observed.

The homogenized parameters were verified by subjecting a representative volume element of the microstructure and the corresponding homogeneous material to a series of tests. A tension/compression test where the specimen was unloaded and reloaded, and a simple shear test, showed that the stress strain curves of the homogenized sample and the RVE were nearly identical.

Chapter 3

Adiabatic Shear Bands in Functionally Graded Materials[1]

3.1 Problem Statement

The initiation and propagation of ASBs in FGMs is critical in understanding the failure of this new class of materials when deformed at high strain-rates. The FGM studied here is a tungsten/nickel-iron alloy; at the micro-scale, this material consists of tungsten particles suspended in a nickel-iron matrix. Here, we study the material at the macro-scale, with the thermomechanical properties derived by the rule of mixtures from the properties of the two constituents. As seen in Chapter 2, the rule of mixtures gives macroscopic properties that are close to those obtained by the RVE method. We seek to find the effects, if any, that the spatial gradation of material properties has on the initiation and propagation of ASBs.

3.2 Numerical Tests

3.2.1 Initial and Boundary Conditions

Utilizing the plane strain FE code described in Section 1.2, we examine the thermomechanical deformations of a FG prismatic body of square cross-section of side length $2H$. We assume that the compositional profile, and thus the thermomechanical deformations, are symmetric about the two centroidal axes. Deformations of a quarter of the cross-section, represented by the first quadrant shown shaded in Figure 3.1, are analyzed using the boundary conditions given in equation (3.1). The left (segment AD) and bottom (segment AB) surfaces contain

---

[1]Material in this Chapter is from Ref. [83]
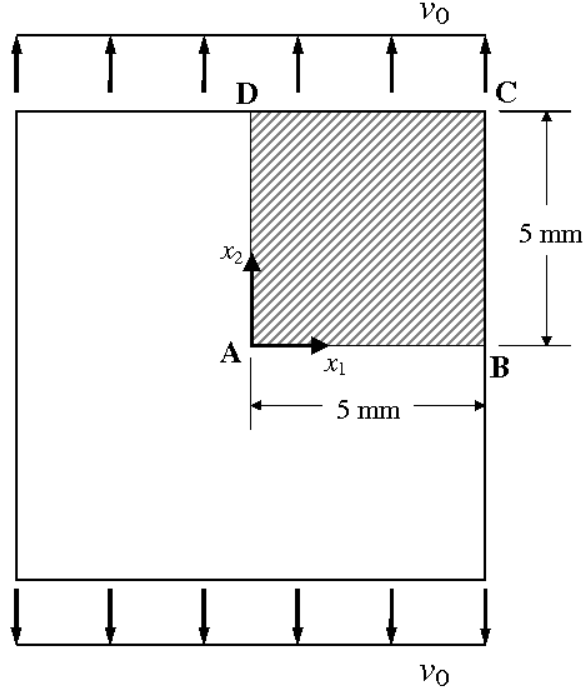
Figure 3.1: Schematic sketch of the problem studied

the symmetry conditions (no normal displacements or heat flux). The other lateral surface (segment BC) is taken to be traction-free. The top surface CD is given velocity v_0 after a short ramp time of $1\mu s$. As described in Section 1.2.3, the body is taken to be initially at rest, with uniform temperature, and with zero initial porosity. Thus

$$\mathbf{x}(\mathbf{X}, 0) = \mathbf{X}, \ \mathbf{v}(\mathbf{X}, 0) = \mathbf{0}, \ \theta(\mathbf{X}, 0) = \theta_0, \ \dot{\theta}(\mathbf{X}, 0) = 0, \ \rho(\mathbf{X}, 0) = \rho_0,$$

$$\varepsilon_e^p(\mathbf{X}, 0) = 0, \ f(\mathbf{X}, 0) = 0, \ (X_1, X_2) \in [0, H] \times [0, H],$$

$$T_{21} = T_{11} = 0, \ Q_1 = 0 \text{ on } X_1 = H,$$

$$T_{21} = 0, \ v_1 = 0, \ Q_1 = 0 \text{ on } X_1 = 0, \tag{3.1}$$

$$T_{12} = 0, \ v_2 = 0, \ Q_2 = 0 \text{ on } X_2 = 0,$$

$$T_{12} = 0, \ Q_2 = 0, \ v_2 = \begin{cases} v_0 t, \ 0 \le t \le 1 \ \mu s, \\ v_0, \ t \ge 1\mu s, \end{cases} \text{ on } X_2 = H.$$

3.2.2 ASB initiation criterion

Batra and Rattazzi [86] studied the initiation and propagation of an ASB in a prenotched thick-walled steel tube and found that the choice of the ASB initiation criterion will affect the predicted initiation time. They used four different criteria: (i) the effective plastic strain at a point equals 0.5, (ii) the effective plastic strain at a point equals 1.0, (iii) the effective stress at a point has dropped to 90% of its peak value at that point, and (iv) the effective stress at a point has dropped to 80% of its maximum value at that point; in each case the material point must be deforming plastically. Criteria (iii) and (iv) reflect Marchand and Duffy's [20] observation that the torque required to twist thin-walled tubes drops precipitously upon the initiation of an ASB. Batra and Kim [87] scrutinized ASBs in twelve materials deformed in simple shear and proposed criterion (iv) which we use in the present work.

3.3   Computation and Discussion of Results

3.3.1   Compositional Profile

Results have been computed for tungsten (W) particles interspread in NiFe matrix with the volume fraction, $\nu_{f,NiFe}$, of NiFe given by one of the following two expressions.

$$
\begin{array}{cc}
\text{Type-I} & \text{Type-II} \\
\nu_{f,NiFe} = \left\{ \begin{array}{ll} c_f \frac{r}{H}, & r \leq H \\ c_f, & r \geq H \end{array} \right. & \nu_{f,NiFe} = \left\{ \begin{array}{ll} c_f \left(1 - \frac{r}{H}\right), & r \leq H \\ 0, & r \geq H. \end{array} \right.
\end{array} \tag{3.2}
$$

Here r is the radial distance from the specimen centroid, and $2H = 10$ mm equals the length of a side of the square cross-section. In both type-I and type-II FGMs, material properties in the region $r > H$ are constants. In type-I FGMs, the volume fraction of NiFe varies from zero at the specimen centroid to c_f at $r = H$, and in type-II FGMs, it varies from c_f at the specimen centroid to zero at $r = H$. The material is homogeneous in the region $r \geq H$. The variation of the mass density in these two types of FGMs is depicted in Figure 3.2.

The primary reason for studying compositional profile (3.2) is that it does not influence the direction of propagation of an ASB originating from the centroid of the cross-section. For the same overall volume fraction of the constituents, the ASB initiation time may depend upon the distribution of the two constituents. If an ASB does not initiate from the centroid, then the distribution (3.2) of NiFe may affect the direction of propagation of the ASB.
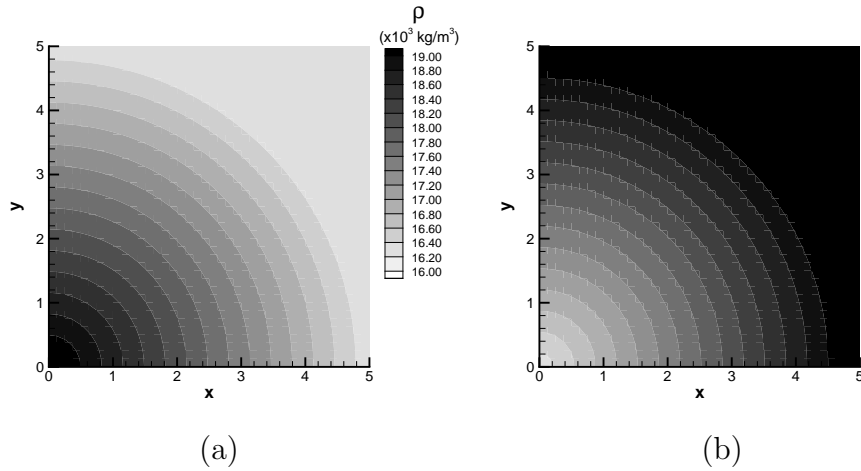
Figure 3.2: Contour plots of density in W/NiFe FGMs; (a) type-I, (b) type-II

3.3.2 Finite Element Mesh

In order to ascertain the effect of the FE mesh on the ASB initiation time, we analyzed deformations of type-I FGM with $c_f = 0.3$ in equation (3.2) with three different uniform FE meshes. As is clear from the results summarized in Table 3.1, the ASB initiation time decreased by 2.1% in going from a 40×40 to a 120×120 uniform FE mesh, and the CPU time increased by a factor of 21. Results presented in subsequent sections are with a 40×40 uniform FE mesh of 4-node isoparametric quadrilateral elements.

Table 3.1: Effect of FE mesh on the ASB initiation time for a type-I FG material with $c_f = 0.3$.

Uniform FE mesh	ASB initiation time (μs)	CPU time (secs)	% change in ASB initiation time
40×40	65.9	1,133	—
80×80	64.8	6,908	1.67
120×120	64.5	29,242	2.12

3.3.3 ASBs in Five Homogeneous Materials

For homogeneous materials, Batra and Lear [45] assumed the presence of 2.5% or 5% initial porosity at the specimen centroid which decayed exponentially to zero with the distance from the centroid. Because of the maximum initial porosity, the centroid acts as a nucleation site for an ASB. However, for a composite, deformations naturally become inhomogeneous

because of the spatial variation of material properties and it determines where and when an ASB initiates. For reference and to delineate the effect of the initial porosity distribution, we have listed in Table 3.2 values of material parameters, and in Table 3.3 the nondimensional ASB initiation times (or equivalently the average axial strain) for five materials deformed at an average axial strain-rate of 5,000/s. For $H = 5$ mm, the axial speed v_0 was increased from zero to 25 m/s in 1 μs and then kept constant. It is clear that an ASB initiates considerably sooner in initially porous materials than in those with zero initial porosity. Nondimensional inertia factor α_I is higher for NiFe, Armco iron and OFHC copper than that for 4340 steel and tungsten even though the mass density of tungsten is almost twice that of steel. Heat conduction effects are highest in OFHC copper than in any of the other four materials studied; it is reflected in the delayed initiation of an ASB in copper. The rather high nondimensional thermal conductivities of NiFe and Armco iron also delay the onset of ASBs in them. The nondimensional thermal conducitivites of tungsten and NiFe are nearly the same but α_I for tungsten is about 1/5th of that for NiFe. A clear correlation among the ASB initiation time, α_I and α_t has not been established yet. We note that the ASB initiation time also depends upon the nominal axial strain-rate.

Table 3.2: Values of thermomechanical parameters for the five materials studied

Material	A (MPa)	B (MPa)	C	m	n	θ_m (K)	$\dot{\varepsilon}_0$ (1/s)
4340 steel	792.19	509.51	0.014	1.03	0.26	1793	10^{-6}
Armco iron	175.12	379.99	0.060	0.55	0.32	1811	10^{-6}
OFHC Copper	89.63	261.64	0.031	1.09	0.31	1356	10^{-6}
Tungsten	1536.9	1183.2	0.029	1.00	0.0751	1700	5000
Nickel-Iron	638.4	2328.6	0.0838	1.0	0.208	1225	5000

Material	$\hat{\alpha}$ (10^{-6}/K)	κ (W/mK)	c (J/kgK)	ρ (kg/m^3)	ν	E (GPa)	α_I^* (10^{-3})	α_t^* (10^{-6})
4340 steel	12.3	38	477	7840	0.27	210	6.19	81.3
Armco iron	12.1	73	452	7890	0.29	196	28.16	163.8
OFHC copper	17.0	386	383	8960	0.33	120	62.48	899.9
Tungsten	5.3	160	138	19300	0.29	400	7.849	480.6
Nickel-Iron	15.0	100	382	9200	0.29	255	9.007	227.6

*Values for an average axial strain-rate of 5,000/s, $H = 5$mm, and $\sigma_0 = A$.

Figure 3.3 exhibits the time-history of the applied axial load for the five materials; the axial strain plotted along the abcissa equals the time multiplied by the nominal axial strain-rate. In each case the initiation of an ASB is accompanied by a rapid drop in the axial load; the rate of drop of the axial load is highest for tungsten than that for any of the other four materials. In each case the ASB initiated from the centroid of the cross-section. The

Table 3.3: Axial strain at ASB initiation in five homogeneous materials deformed in plane strain tension at a nominal strain-rate of 5,000/s.

| Material | Axial strain at ASB initiation | | Temperature rise (K) at ASB initiation* |
	w/ initial porosity	w/o initial porosity*	
Tungsten	0.137	0.386	391
4340 steel	0.315	0.615	315
Nickel iron	–	0.944	354
OFHC copper	0.391	1.045	157
Armco iron	0.433	1.095	253

* denotes present work

porosity at the instant of the ASB initiation equaled 0.041, 0.087, 0.081, 0.126 and 0.155 respectively in W, NiFe, 4340 steel, Fe and Cu; the temperature rise is listed in Table 3.3. An approximate value of the temperature rise is given by $((A + 0.5B(\varepsilon_e^p)^n)\varepsilon_e^p)/(\rho c)$ since the effect of heat conduction till an ASB initiates is small. It also provides a check on the accuracy of computed results. For W, the temperature rise computed from this relation at the time of initiation of an ASB equals 368 K.

3.3.4 ASBs in FGMs

Numerical experiments on type-I and type-II FGMs yielded interesting results summarized in Table 3.4. In type-I FGMs, there is 100% W at $r = 0$, and the volume fraction of NiFe equals 0 at $r = 0$ and increases linearly with r reaching its maximum value at $r = H$; the maximum volume fraction of NiFe at $r = H$ varies from 0.1 to 0.5. In each case, an ASB initiated at the specimen centroid and propagated along a line inclined at approximately 45° to the horizontal axis in the present configuration. The axial strain at the instant of ASB initiation decreased when the maximum volume fraction of NiFe at $r = H$ was increased from 0.1 to 0.4, and then increased a little when c_f in equation (3.3) was increased from 0.4 to 0.5. However, in each case, the average axial strain at the instant of the ASB initiation is less than that for the pure W. It leads one to conjecture that the addition to W of a material less susceptible to shear banding than W increases tungsten's susceptibility to shear banding. In order to test this conjecture, numerical experiments were performed on type-I FGMs with NiFe replaced by 4340 steel, Cu and Fe. The results of these experiments are also included in Table 3.4. The spatial distribution of the volume fraction of W was kept the same. Whereas in each FGM the ASB initiated sooner than that in pure W, the decrease in the time of initiation of an ASB cannot be simply related to the times of initiation of ASBs in the
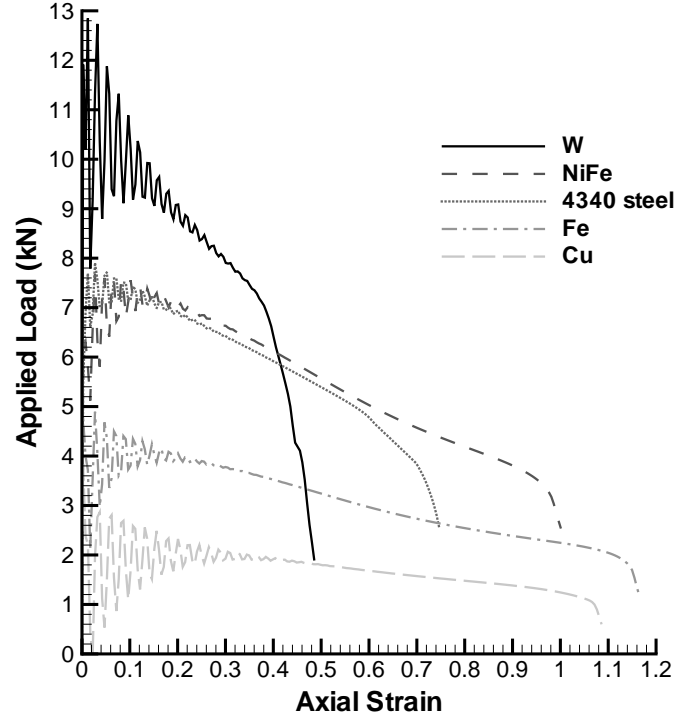
Figure 3.3: Axial load versus axial strain for five homogeneous materials deformed in plane strain tension

constituents.

Contours of the effective plastic strain in type-I FGMs are depicted in Figure 3.4. The effective plastic strain within the ASB exceeds 1 with a peak value of 1.5 at some points. The necking of the region below the ASB is evident in these plots.

For type-II FGMs with the maximum volume fraction of NiFe at the centroid, an ASB initiated from a point on the top surface and propagated inwards along the two directions of the maximum shear stress. These seem to get reflected from the surfaces $X_1 = 0, H$. As shown in Figure 3.5, there are several narrow regions of large plastic deformation. For the first three FGMs, the point where an ASB initiates on the top surface varies with the compositional profile. For the other two FGMs, an ASB initiates from a point within the cross-section. ASBs exhibited in Figure 3.5 reveal that the eventual distribution of regions of intense plastic deformation is independent of c_f. The time of initiation of an ASB decreases monotonically with an increase in the maximum volume fraction, c_f, of NiFe. However, the rate of decrease of the time of initiation decreases rapidly as c_f is increased from 0.1 to 0.5. In contrast to FGMs of type-I, necking occurs in the upper part rather than in the lower portion of the cross-section.

Table 3.4: Axial strain and point of initiation of ASBs in FGMs

Specimen type and constituents	Max. v_f of NiFe	Axial strain at ASB initiation	Ref. Location of ASB initiation	
			X	Y
W/NiFe Type-I	0.1	0.371	0.000	0.000
	0.2	0.339	0.000	0.000
	0.3	0.327	0.000	0.000
	0.4	0.325	0.000	0.000
	0.5	0.331	0.000	0.000
W/NiFe Type-II	0.1	0.340	1.125	5.000
	0.2	0.314	1.250	5.000
	0.3	0.304	1.375	5.000
	0.4	0.298	4.750	2.875
	0.5	0.292	4.875	2.875
W/4340 Steel Type-I	0.3	0.364	1.125	5.000
W/Cu Type-I	0.3	0.218	0.625	5.000
W/Fe Type-I	0.3	0.268	1.000	5.000
W, $r < 5$ NiFe, $r > 5$	–	0.194	2.875	4.000
W, $r > 5$ NiFe, $r < 5$	–	0.154	4.875	1.500

Of the FGMs studied, the type-I with NiFe matrix delays most the onset of an ASB and that with Fe matrix the least. Figure 3.6 depicts contours of the effective plastic strain in the type-I FGMs with the matrix material either 4340 steel, OFHC copper, or Fe. In each case an ASB initiates from a different point on the top surface.

Composites comprised of W in the region $r < 5$ mm and NiFe elsewhere or vice-a-versa were also analyzed. ASBs initiated in these two composites at much lower values of the average axial strain than in all of the other FGMs and in the two homogeneous bodies. Recall that material properties are discontinuous across the surface $r = H$. It suggests that the presence of a material singular surface enhances the initiation of an ASB. The gradients of displacements and temperature must be discontinuous across $r = H$ in order for surface tractions and the normal component of the heat flux to be continuous.

The significant difference between the initiation times of ASBs in the two composites with W in the region $r < 5$ mm and NiFe in $r > 5$ mm or vice-versa can not be explained on the basis of the arrival time of the elastic loading wave since $\sqrt{E/\rho}$ is nearly the same for W and NiFe. However, their acoustic impedances, $\sqrt{E\rho}$, are quite different. Batra and Kwon [88] scrutinized the initiation and development of ASBs in simple shearing deformations of a bimetallic body with the lower half made of one thermoviscoplastic material and the upper half of a different thermoviscoplastic material. For both materials having the same value of

the shear modulus and the mass density, they found that the ASB developed in the body with the higher value of the thermal softening coefficient even though the initial nonuniform temperature was symmetric about the centerline and maximum at the center. The differences in thermal conductivities shifted the ASB a little. No shift in the center of the ASB away from the centerline occurred even when the shear modulus of one material equaled twice that of the other material. The data included in the last two rows of Table 3.4 indicates that an ASB initiated at the point (2.875, 4.0) or $r = 4.93$ mm when W occupied the region $r < 5$ mm, and at the point (4.875, 1.50) or $r = 5.10$ mm for W in the region $r > 5$ mm. The coordinates of points are in the reference configuration. These results agree with those of Batra and Kwon [88]. Zhou et al. [89] analyzed numerically and experimentally plane strain deformations of a particulate composite comprised of W particles in NiFe matrix and modeled each constituent as a thermoviscoplastic material. Thus there were several surfaces of discontinuity present in the body. They also found that an ASB initiated sooner in the composite than in either one of the two constituents. They neither homogenized material properties nor investigated the effect of the spatial variation of the volume fraction of the two constituents nor considered the evolution of porosity.

An ASB initiates from the point at the center of the shaded area in Figure 3.7a. The shaded zones in Figure 3.7b-d depict the shear banded regions. Since the length of this region increases in both directions around the point shown in Figure 3.7a, one can conclude that the shear band propagates outwards in both directions.

For each problem studied, the time step was seen to drop drastically once an ASB had initiated at a point in the body. The numerical values of the ASB initiation time may depend upon the FE mesh employed. However, differences in results from a much finer mesh than the one used here are likely to be less than 5%. Recall that for a type-I FGM, as the ASB initiation time obtained with 6400 uniform elements differed from that with 1600 uniform elements by less than 2.2%. One could use either adaptively refined meshes, e.g. see [21], or a meshless method such as the modified smoothed particle hydrodynamics [90] to compute results. The former technique smoothens deformation fields and tends to delay the ASB initiation but gives narrower bands. The latter is computationally less efficient than the FEM.

Other compositional profiles symmetric about the two centroidal axes include $\nu_{f,NiFe} = a + bX_1^{2p}X_2^{2q}$ where a, b, p and q are real numbers such that $0 \leq \nu_{f,NiFe} \leq 1$ for all admissible values of X_1 and X_2. These have not been examined.

Figure 3.4: Contours of the effective plastic strain in type-I FGMs with the maximum volume fraction of NiFe at $r = H$ equal to (a) 0.1, (b) 0.2, (c) 0.3 (d) 0.4, and (e) 0.5
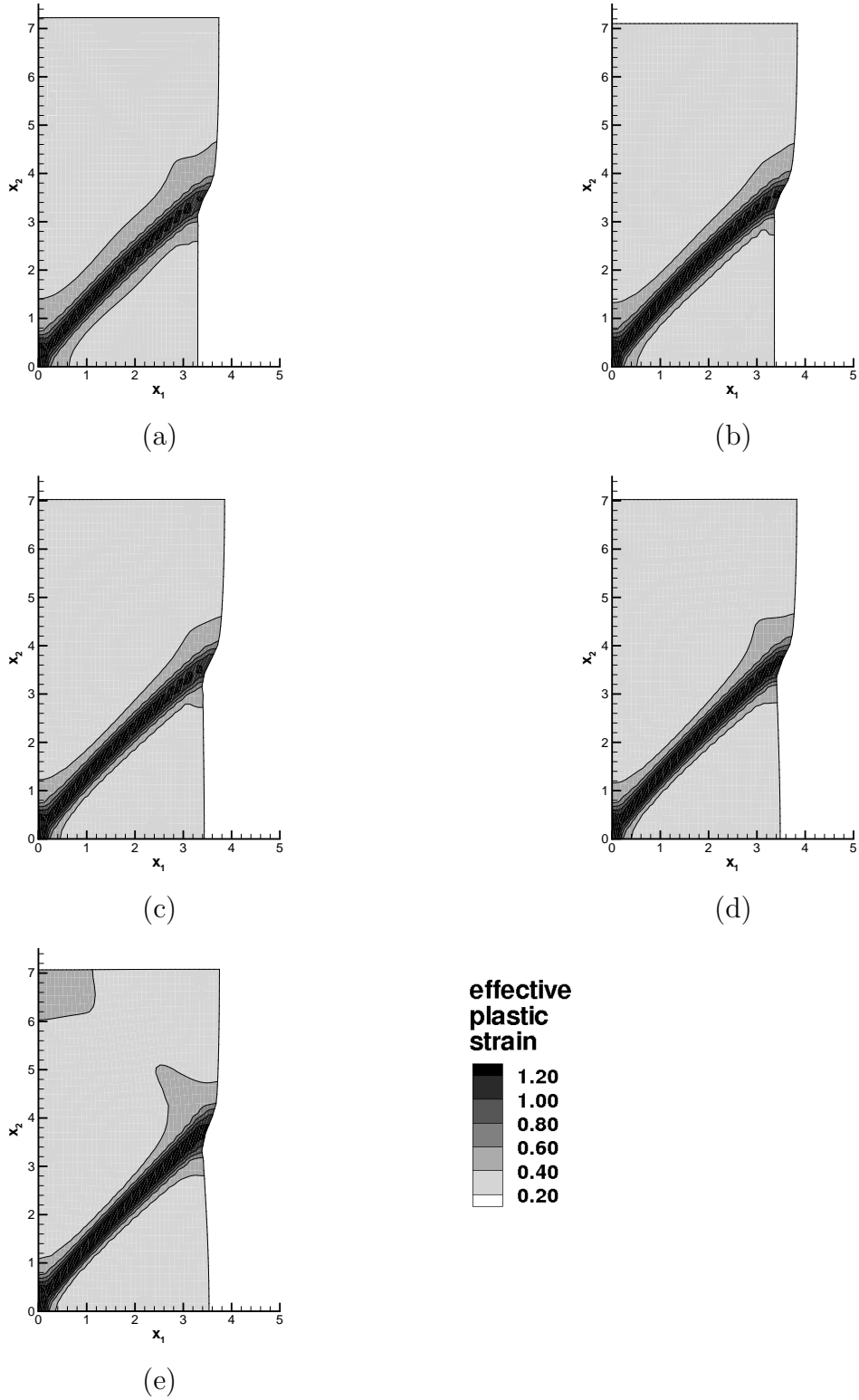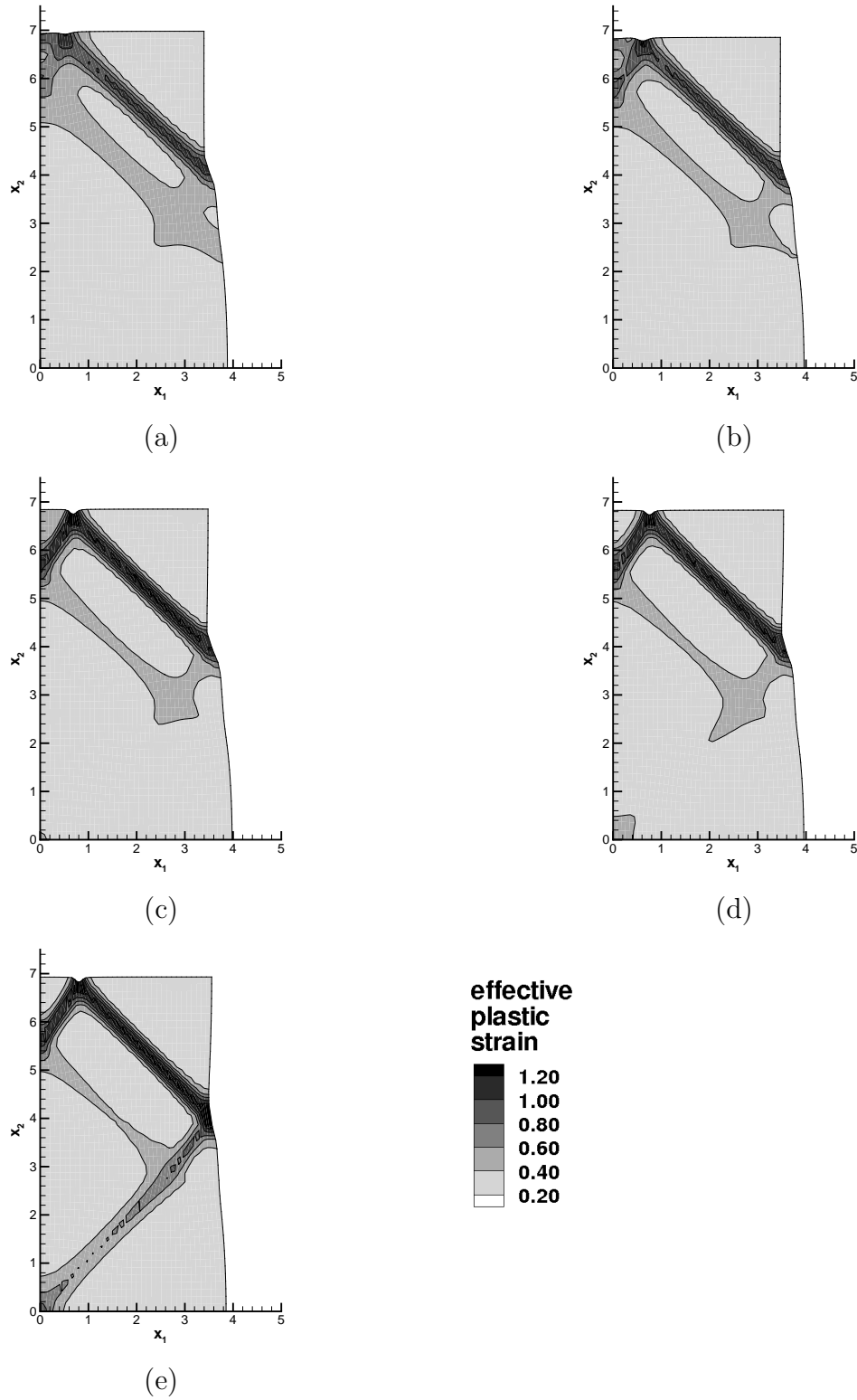
Figure 3.5: Contours of the effective plastic strain in type-II FGMs with the maximum volume fraction of NiFe at $r = 0$ equal to (a) 0.1, (b) 0.2, (c) 0.3 (d) 0.4, and (e) 0.5

(a)

(b)

(c)

effective
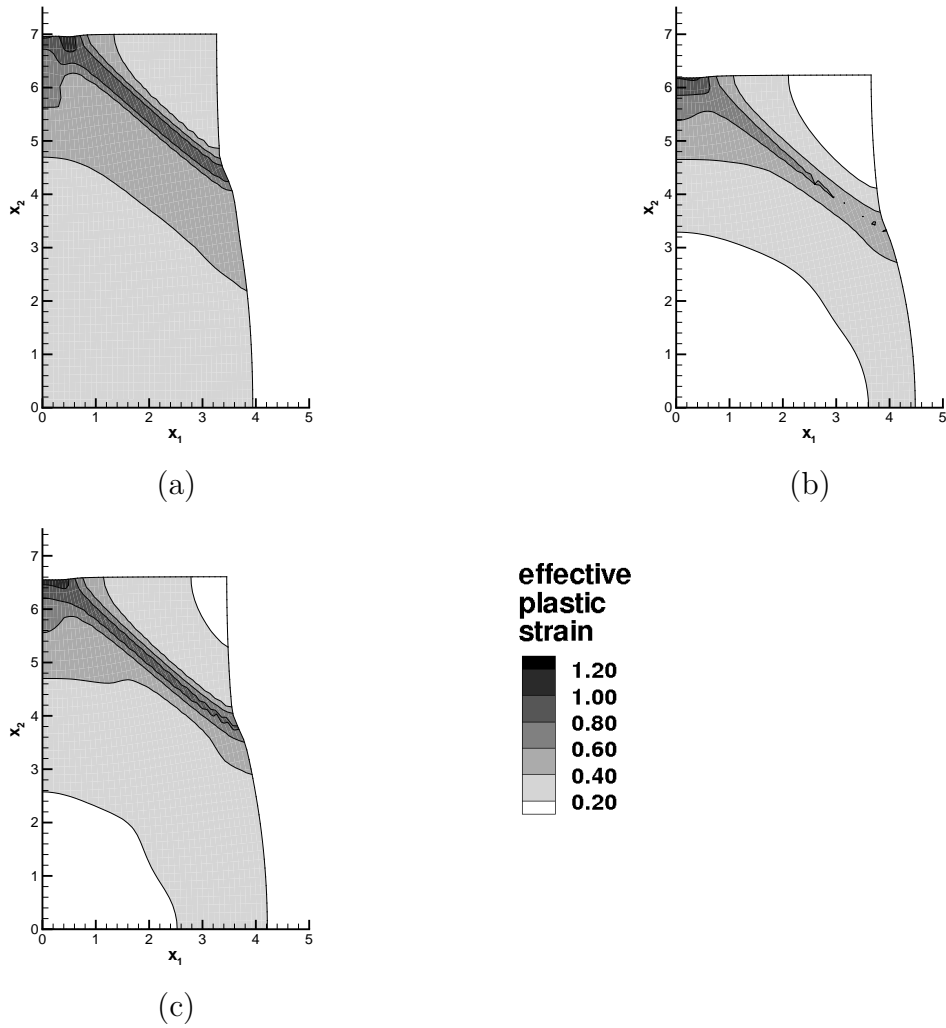plastic
strain

1.20
1.00
0.80
0.60
0.40
0.20

Figure 3.6: Contours of the effective plastic strain in type-I FGMs with the maximum volume fraction of W at $r = 0$ equal to 0.7 and (a) 4340 steel, (b) Cu, and (c) Fe as the other constituent

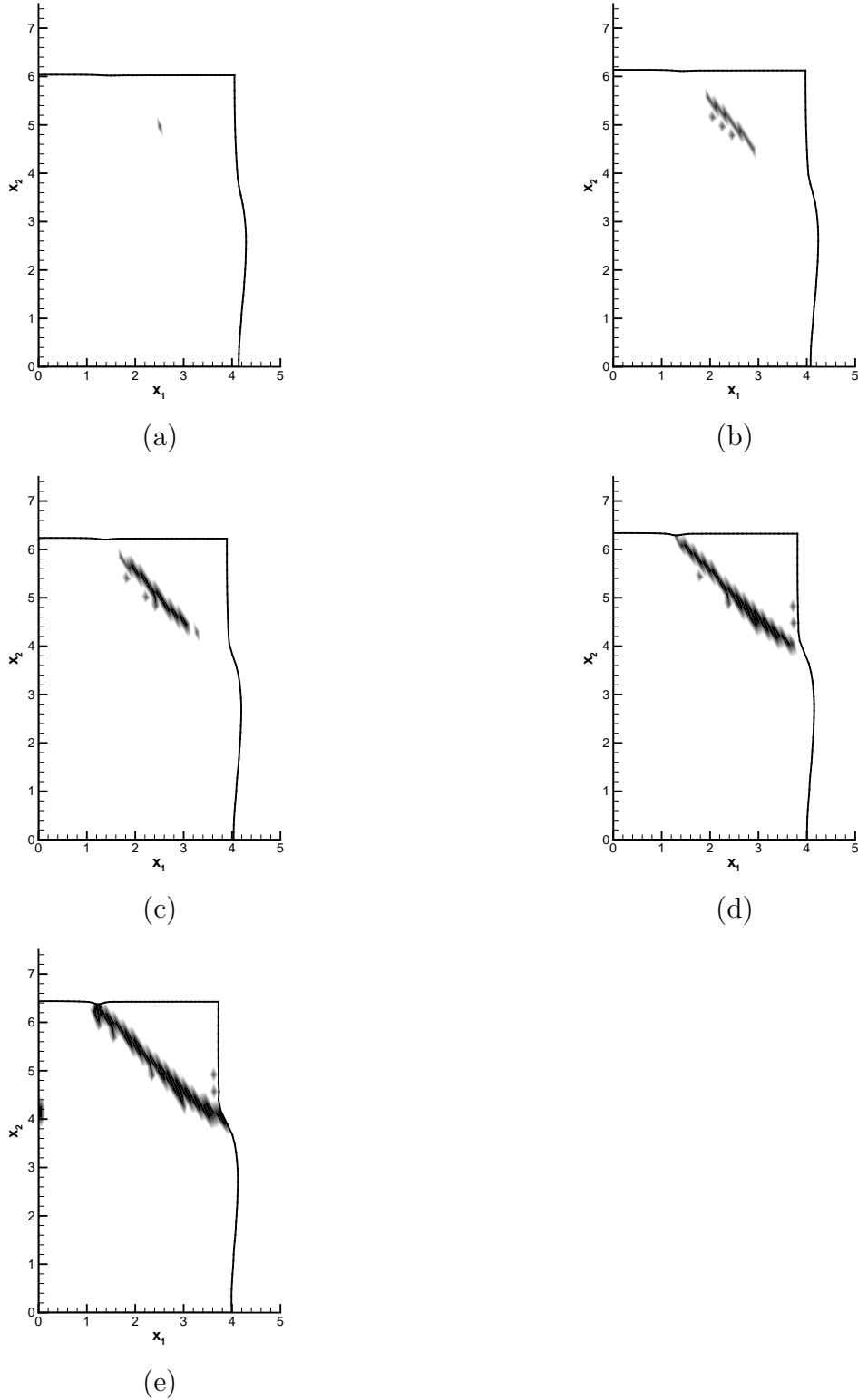**Figure 3.7:** Shear-banded region, shown shaded, in a W/NiFe composite with W in the region $r < 5$ mm and NiFe in $r > 5$ mm at (a) $42\mu s$, (b) $46\mu s$, (c) $50\mu s$, (d) $54\mu s$, and (e) $58\mu s$; the effective plastic strain in the shaded region exceeds 1.0

47

3.4 Conclusions

We have analyzed the initiation and propagation of ASBs in FG bodies deformed in plane strain tension at an average axial strain-rate of 5000/s. Each FGM studied is comprised of two constituents one of which is tungsten and the other NiFe, copper, 4340 steel or iron. Several spatial distributions of the two constituents in the region $r \leq H$ are considered. Here r is the radial distance from the centroid of the square cross-section of side $2H$. The material is homogeneous in the region $r \geq H$. For uniform 40×40 and 120×120 finite element meshes of 4-node quadrilateral elements, the ASB initiation time differed by 2.1%. It is found that an ASB initiates either at the specimen centroid or at a point on the top surface where the normal component of velocity is prescribed. In each case, it propagates along the direction of the maximum shear stress. An ASB initiates in a FGM at a lower value of the average axial strain than that in a homogeneous body made of either one of the two constituents. Thus, for the material combinations studied here, the addition to tungsten of a material that is less susceptible to adiabatic shear banding than tungsten, enhances the susceptibility of the FGM to adiabatic shear banding. The analysis can thus be used to optimize the compositional profile to either delay or to enhance the onset of an ASB.

Chapter 4

Brittle and Ductile Fracture in Functionally Graded Materials[1]

4.1 Problem Statement

Here we investigate the initiation and propagation of brittle and ductile failures in tungsten/nickel-iron FGMs. The failure of FGMs is of great interest to designers–FGMs allow material transitions without a failure-prone interface, but little is known about crack propagation and material failure of the FGMs themselves. Both constituents and the overall composite are taken to be thermoelastoviscoplastic, allowing the plasticity-driven ductile crack to initiate and propagate. Very few researchers have simulated it numerically. The crack propagation speed is obtained in both pure materials and in the FGM, and the interaction between ASBs and the ensuing ductile fracture is examined.

4.2 Numerical Tests

4.2.1 Initial and Boundary Conditions

The plane strain FE code described in Section 1.2 is utilized; the crack propagation routines and the contact algorithm described in Section 1.2.6 are implemented. For both brittle and ductile fracture tests, the body is assumed to be initially at rest, stress-free, at a uniform temperature, and have no initial porosity. Under the plane strain assumption, it is tacitly assumed that the volume fraction of constituents is constant in the X_3 direction. For the brittle fracture case, we examine a center-cracked square cross-section of length and width

---

[1]Material in this Chapter is from Ref. [91].
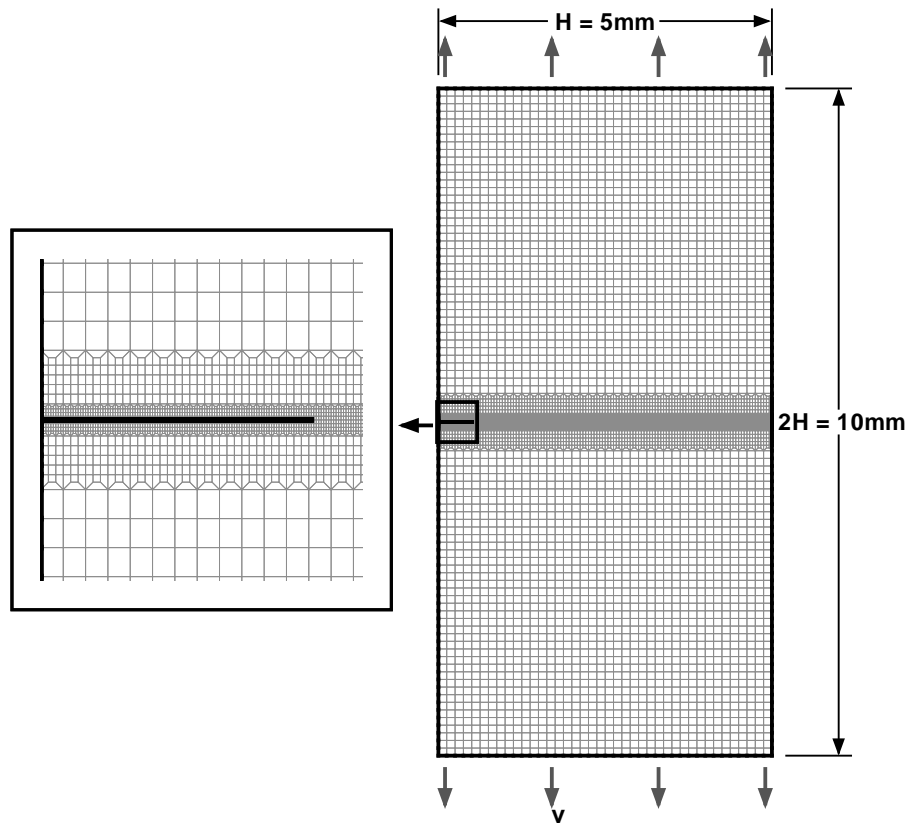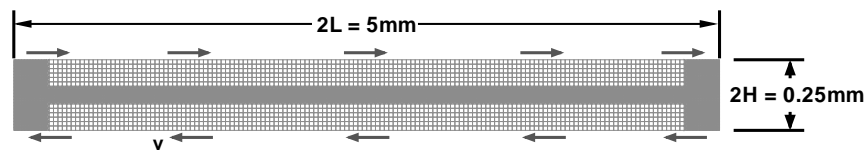
Figure 4.1: (a) FE mesh for plane strain tensile deformations of a pre-cracked plate; inset shows details of the mesh around the cracked region; (b) FE mesh for plane strain shear deformations of a plate

$2H$ deformed in plane-strain tension. Symmetry along the X_2 axis is exploited; deformations in half of the body, shown in Figure 4.1a, are analyzed. The symmetry about the X_1 axis is not exploited due to the nature of the crack propagation algorithm, which only allows cracks internal to the body. Boundary conditions arising from the symmetry of deformations are

imposed at points on the centroidal axis $X_1 = 0$. The other vertical surface $X_1 = H$ is taken to be traction free and thermally insulated. Normal velocity, null tangential tractions and zero heat flux are prescribed on the top horizontal surface $X_2 = H$. The prescribed normal velocity increases linearly with time to its steady state value v_0 in 1 μs and is then held fixed. Thus, for the brittle fracture problem

$$
\begin{aligned}
& T_{21} = T_{11} = 0, \; Q_1 = 0 \text{ on } X_1 = H, \\
& T_{21} = 0, \; v_1 = 0, \; Q_1 = 0 \text{ on } X_1 = 0, \\
& T_{12} = 0, \; Q_2 = 0, \; v_2 = \begin{cases} v_0 t, \; 0 \le t \le 1 \; \mu\text{s}, \\ v_0, \; t \ge 1\mu\text{s}, \end{cases} \text{ on } X_2 = H.
\end{aligned}
\tag{4.1}
$$

For the ductile fracture case, we analyze plane strain shear deformations of a body of length $2L$ and height $2H$, as shown in Figure 4.1b. Periodic boundary conditions are applied on the surfaces $X_1 = \pm L$, which specifies that the displacements and temperatures are equal at corresponding points–this simulates an infinitely long specimen of height $2H$. The top and bottom surfaces are taken to be thermally insulated and restrained from motion in the X_2 direction. Equal and opposite tangential velocity v_1 that increases linearly with time from zero to its steady value v_0 is 1μs is applied. Thus on $x_2 = X_2 = \pm H$, we have

$$
Q_2 = 0, \; v_2 = 0, \; v_1 = \begin{cases} \pm v_0 t, \; 0 \le t \le 1 \; \mu\text{s}, \\ v_0, \quad t > 1 \; \mu\text{s}. \end{cases}
\tag{4.2}
$$

For $t > 1$ μs, the average shear strain-rate is v_0/H. Note that only the top and the bottom surfaces are restrained from moving vertically and other material particles are free to move in the $x_1 x_2$-plane.

As in Chapter 3, the local material properties were derived by the rule of mixtures. As shown in Chapter 2, this provides a reasonable estimate of the thermoelastoviscoplastic properties over a wide range of volume fractions, and the properties are easily computed from the properties of the constituents.

4.2.2 Failure Initiation Criterion

Brittle failure

Ritchie et al. [92] proposed that the brittle failure initiates at a point when $\sigma_p/\sigma_0 = 3.0$ over a certain length that depends upon the microstructure of the material and usually equals a grain diameter. Here σ_p and σ_0 equal, respectively, the maximum principal tensile stress at a point and the yield stress in a quasistatic simple tension/compression test. For the

Johnson-Cook material, σ_0 can be taken to equal A. Tensile experiments of Hendrickson et al. [93] on prenotched steel plates with a yield stress of 705 MPa deformed at nominal stress rates of ~ 1 to 10^4 MPa/s revealed that brittle failure occurred when $\sigma_p/\sigma_0 \simeq 2.34$. This value of σ_p/σ_0 was found to be independent of the temperature and the rate of loading. Here we assume that brittle failure initiates at a point when $\sigma_p/\sigma_0 = 3.0$ there and propagates in the direction of the minimum gradient in σ_p.

Ductile failure

Ductile failure is generally believed to initiate due to the nucleation and coalescence of voids within an ASB. We recall that the effective plastic strain induced within an ASB exceeds 1. Accordingly, a ductile failure is assumed to ensue at a point when the effective plastic strain equals 1.5 and propagate in the direction of the minimum gradient in the effective plastic strain.

4.3 Computation and Discussion of Results

### 4.3.1 Wave Propagation in a Linear Elastic FG Bar

We validate our methodology of analyzing transient deformations of a FG body by studying wave propagation in a linear elastic bar whose Young's modulus, E, mass density ρ, and Poisson's ratio ν are given by

$$E = 200(1 + 0.25X_1)\text{GPa}, \ \rho = 10^4(1 + 0.25X_1)^{-1}\text{kg/m}^3, \ \nu = 0.29. \tag{4.3}$$

In equation (4.3) X_1 is in mm. Thus the wave speed $c_w = \left(\dfrac{E(1-\nu)}{\rho(1+\nu)(1-2\nu)}\right)^{1/2}$ varies affinely from 5.12 km/s at $X_1 = 0$ to 6.40 km/s at $X_1 = 20$ mm. However, the acoustic impedance $(= \sqrt{E\rho})$ is constant throughout the bar. In order to simulate one-dimensional elastic deformations of the bar, all nodes were restrained from moving in the X_2-direction, and the material parameter A was assigned a very high value to suppress plastic deformations. Since the computer code for plane strain deformations tacitly assumes that $u_3 = 0$, therefore, the only non-vanishing component of displacement is u_1. The 20 mm $\times$ 0.5 mm bar was divided into 800×20 uniform 4-node quadrilateral elements. Various integrals appearing in the weak formulation of the problem were computed by using the 2×2 quadrature rule with values of material parameters evaluated at the integration points. The same strategy was employed by Batra [94] to analyze static finite plane strain deformations of an inhomogeneous Mooney-Rivlin material. An analytical solution of the problem, using the Laplace transform
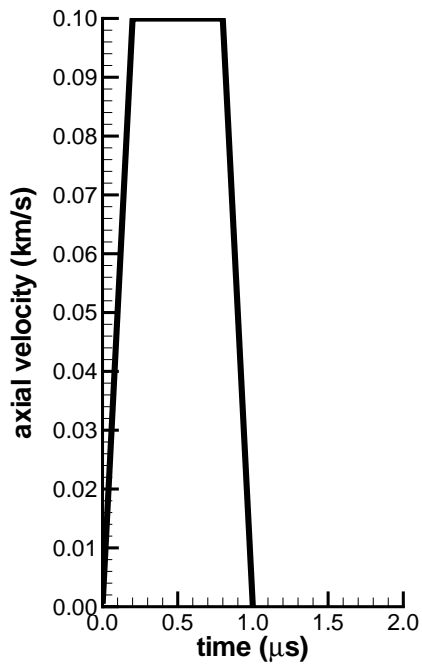
(a)
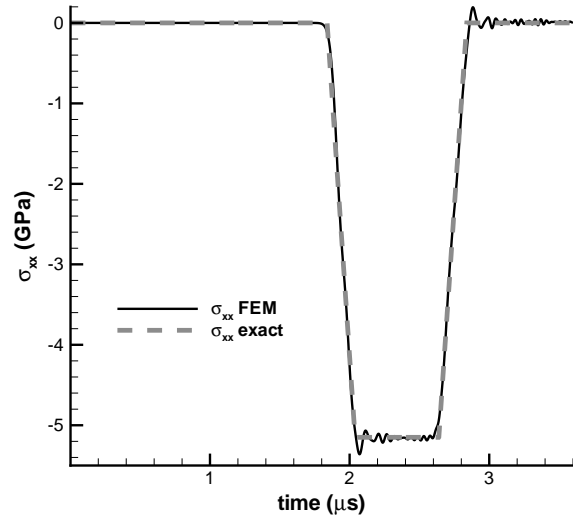
(b)
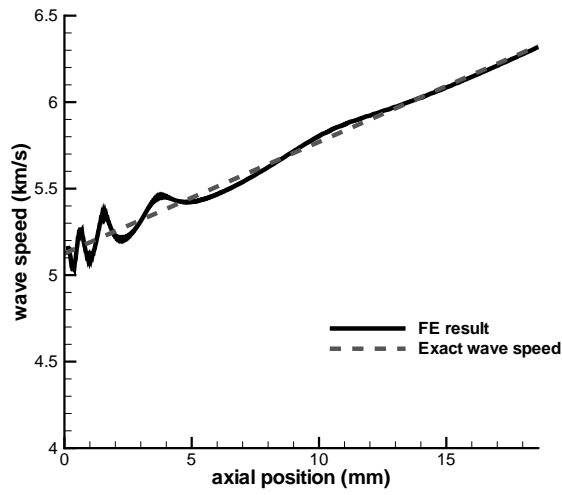
(c)

Figure 4.2: (a) Time history of the axial velocity prescribed at the left end of the bar; (b) comparison of the time histories of the axial stress at $x = 10$ mm obtained from the numerical and analytical solutions; (c) comparison of the spatial variation in the wave speed

technique, has been given by Chiu and Erdogan [95]. It is inverted numerically by employing Laguerre polynomials to find the axial stress and the axial velocity as a function of time t.

Figure 4.2a depicts the axial velocity prescribed at the end $X_1 = 0$ of the bar. The time histories of the axial stress at $X_1 = 10$ mm obtained from the numerical and the analytical solutions are compared in Figure 4.2b, and the spatial variations of the wave speed obtained from the numerical and the analytical solutions are compared in Figure 4.2c. Except for small oscillations, the two sets of results agree well with each other. The amplitude of oscillations can be diminished by introducing an artificial viscosity, but this was not attempted.

4.3.2   Simulation of Brittle Fracture

Crack Propagation Speed

The 10 mm × 10 mm cross-section has an initial sharp crack of length 1 mm at the horizontal centroidal axis with the center of the crack coincident with the centroid of the plate. The plate is deformed at an average axial strain-rate of either 200/s or 2,000/s. Values of Young's modulus, E, mass density, ρ, and Poisson's ratio, ν, for W and NiFe, and the speeds of the longitudinal wave in a bar and the Rayleigh wave speed are listed in Table 4.1; values of other material parameters are given in Table 4.2 and in equation (4.4). We note that NiFe exhibits considerably higher strain- and strain-rate hardening than W.

Table 4.1: Material parameters and wave speeds for nickel-iron and tungsten

Material	Young's modulus (GPa)	Poisson's ratio	Mass density (kg/m^3)	Bar wave speed (m/s)	Acoustic impedance (kg/m^2 s)	Rayleigh wave speed (m/s)
NiFe	255	0.29	9200	5265	48.44×10^6	3035
Tungsten	400	0.29	19300	4552	87.86×10^6	2624

Table 4.2: Values of material parameters for NiFe and W

| Material	A (MPa)	B (MPa)	C	θ_m (K)	c (J/kg K)	κ (W/mK)	α (10^{-6}/K)	m	n
NiFe	150.0	546.0	0.0838	1225	382	100	15	1.0	0.208
W	730	562	0.290	1723	138	160	5.3	1.0	0.075

Other parameters were assigned the following values for both materials.

$$\dot{\varepsilon}_0 = 10^{-6}/\text{s}, \ \beta_1 = 1.5, \ \beta_2 = 1.0, \ f_2 = 0.04, \ s_2 = 0.1, \ \theta_r = 273 \text{ K},$$
$$\tau = 10^{-8}s, \ \varepsilon_n = 0.5, \ f_c = 0.15, \ f_u = 2/3, \ f_f = 0.25, \ m = 1.0. \tag{4.4}$$

The FE mesh used to analyze the problem is depicted in Figure 4.1a, details of mesh around the crack-tip are given in the inset. The mesh consists of 17,444 4-node quadrilateral elements with 1,080 elements along the axis of the crack. There are 108 uniform elements behind the crack-tip and 972 ahead of it; thus the length of an element is 4.63 μm. The appropriateness of the mesh has been ascertained by ensuring that the computed speed of an elastic wave is very close to the analytic value when E and ρ vary along the direction of propagation of the wave. Once the brittle failure criterion at a node is met, that node is split into two essentially overlapping but unconnected nodes as described in Section 1.2.6. Thus an elastic unloading wave emanates from the newly created crack surfaces and propagates into the body. The position of the crack-tip at different times is determined and a polynomial is fit to the data. The first derivative of this polynomial fit gives speed, C_s, of crack propagation as a function of time or the position of the crack-tip. It was found that C_s so determined is very sensitive to the polynomial fit. Three curve fits with the coefficient of regression > 0.999 gave noticeably different values of C_s. Thus C_s at a point is taken to equal the slope of the least squares line through the neighboring ± 10 points. Plates consisting of pure W and pure NiFe were tested along with FG plates consisting of 100% W at $X_1 = 0$ to 0% W at $X_1 = 5mm$ (hereafter referred to as W2NiFe) and vice-versa (hereafter referred to as NiFe2W). The Rayleigh wave speed and the crack propagation speed, C_s, versus the crack length for nominal strain-rates of 200/s and 2,000/s are depicted in Figure 4.3a-d. Freund's [96] analysis of crack propagation in an infinite homogeneous linear elastic body shows that the maximum crack propagation speed equals the Rayleigh wave speed; Eischen [49] has proved a similar result for inhomogeneous materials. For each of the homogeneous and the two FG plates C_s for the nominal strain-rate of 2,000/s is higher than that for the nominal strain-rate of 200/s. For the W plate deformed at 200/s, C_s increases as the crack propagates to the right edge of the plate but at the higher strain-rate of 2,000/s, it soon approaches a steady value that is a little less than the Rayleigh wave speed. For a NiFe plate deformed at 2,000/s, the crack begins to propagate to the right and then a large region of the plate ahead of the crack fails instantaneously as indicated by the maximum principal tensile stress exceeding $3\sigma_0$ simultaneously everywhere in this region. It is signified in Figure 4.3b by the sudden drop in the crack propagation speed C_s; the shattered region is depicted in Figure 4.3e as unshaded.
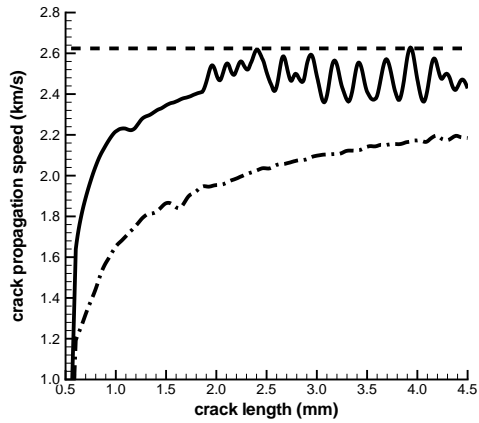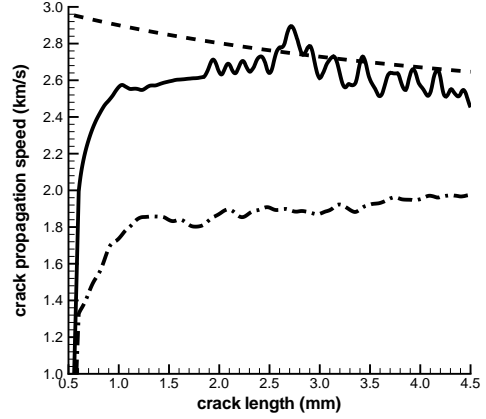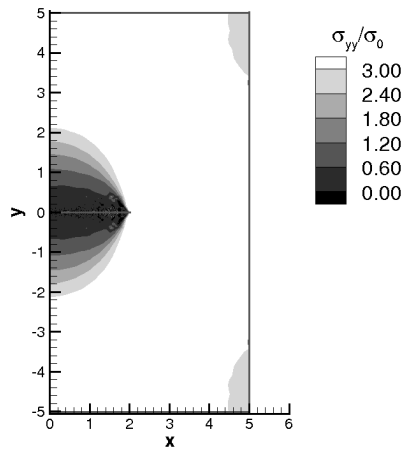
(a)
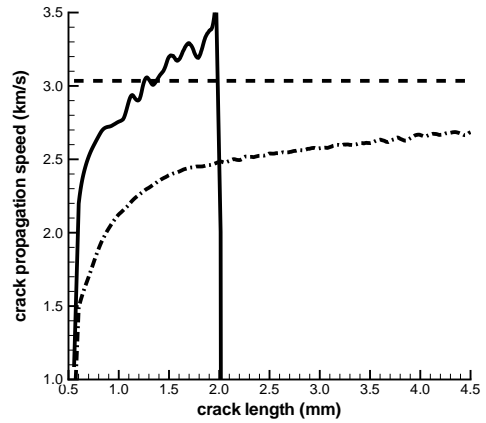
(b)
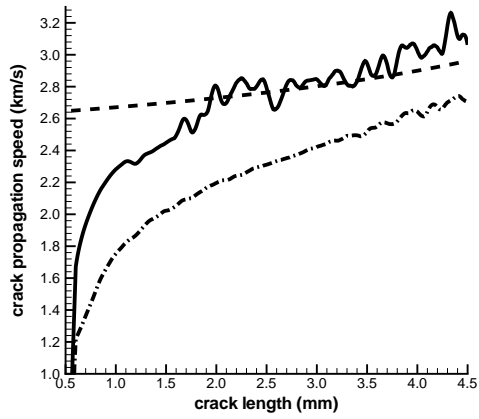
(c)

(d)

(e)

Figure 4.3: (a)-(d): Crack propagation speed versus crack length at nominal strain-rates of 200/s and 2000/s for (a) pure tungsten, (b) pure nickel-iron, (c) W2NiFe, and (d) NiFe2W (key: - - - Rayleigh wave speed; ——— nominal strain-rate = 2000/s; $- \cdot - \cdot -$ nominal strain-rate = 200/s); (e) shattered region in the NiFe plate deformed at a nominal strain-rate of 2000/s is unshaded

56

For the W2NiFe FG plate, C_s continues to increase with the crack extension, is always less than the Rayleigh wave speed when the plate is deformed at 200/s but approaches the Rayleigh wave speed when the nominal strain-rate is 2,000/s. Except for differences in magnitudes, the curves in Figures 4.3a and 4.3c are similar. Thus as far as crack propagation due to brittle failure is concerned, the W and the W2NiFe FG plates behave alike. However, for the NiFe2W FG plate, even though the Rayleigh wave speed decreases monotonically with the distance from the left edge because of the spatial variation in the material properties, the computed crack speed C_s first increases and approaches essentially a steady value after the crack has propagated a certain distance. The crack speed is higher when the nominal strain-rate equals 2,000/s than that when the nominal strain-rate is 200/s. No shattering of the NiFe2W FG plate at either of the two strain-rates is observed.

Shattering Phenomenon

Returning to the shattering of the NiFe plate, several numerical experiments were conducted by varying the nominal axial strain-rate. The plate shattered at nominal axial strain-rates exceeding 1,130/s but did not shatter at a nominal axial strain-rate of 1,120/s. The crack extension/elongation at the instant of the plate shattering decreased with an increase in the nominal axial strain-rate; it equaled $\sim$ 2.01, 1.47 and 0.741 mm for nominal axial strain-rates of 1,130, 2,000 and 3,000/s, respectively.

Axial Force

We have plotted in Figure 4.4 the variation of the computed axial load as the crack propagates to the right. Small oscillations in the load due to the arrival of unloading waves emanating from the newly formed crack surfaces have been diminished by using a neighboring-point-average technique, included in TecPlot. At a nominal strain-rate of 200/s, the crack propagation is stable in both pure W and W2NiFe FG plates as signified by either the load remaining essentially steady or increasing except when the crack has propagated to a point near the right edge. At the higher strain-rate of 2,000/s, the axial load for pure W remains nearly constant at $\sim$ 4.67 kN until the crack-tip has advanced by 1.75 mm and then slowly increases until the crack-tip is close to the outer edge of the plate. When the precracked W plate is pulled at a nominal axial strain-rate of 200/s, the axial load continues to increase slowly until the crack length equals 2.2 mm and then gradually decreases. Recall that the surface area of the horizontal plane containing the crack decreases as the crack extends, and except for the first 1 μs, the bar is being pulled with a uniform axial velocity. Thus the working of external forces is proportional to the axial force. The variation of the axial load

with the advance of the crack in NiFe and NiFe2W FG plates is similar to that in the W plate except that a large portion of material ahead of the crack suddenly fails in the pure NiFe plate deformed at a nominal strain-rate of 2,000/s. For the NiFe2W FG plate, the variation of the axial load with the crack length is similar to that for the W2NiFe FG plate.
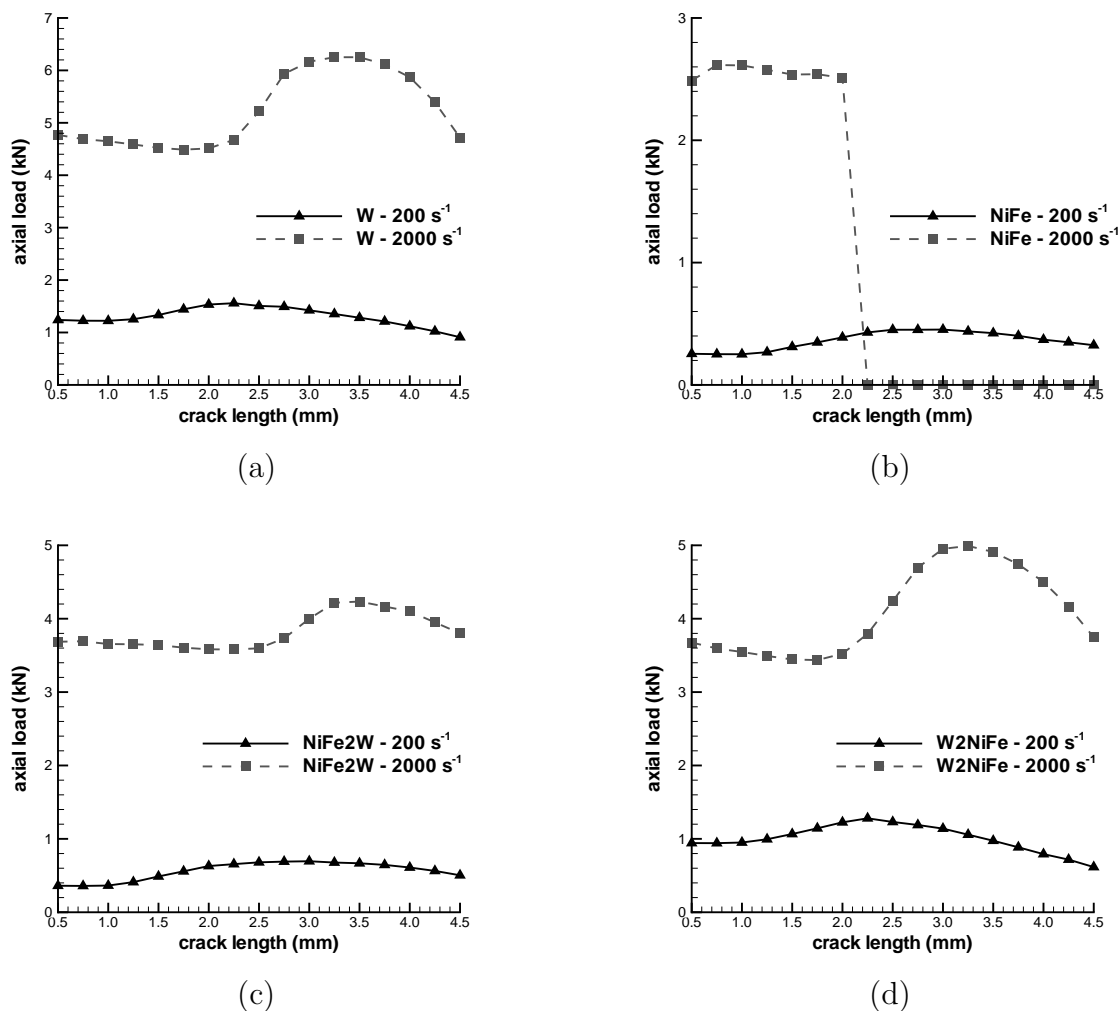

(a)

(b)

(c)

(d)

Figure 4.4: Axial load versus crack length at nominal strain-rates of 200/s and 2000/s for (a) tungsten, (b) nickel-iron, (c) W2NiFe, and (d) NiFe2W plates

J-integral

A detailed examination of stresses and strains induced within the specimen revealed that deformations were virtually elastic everywhere except near the crack-tip where small plastic strains developed. In order to see if concepts of the strain energy release rate or the J-integral
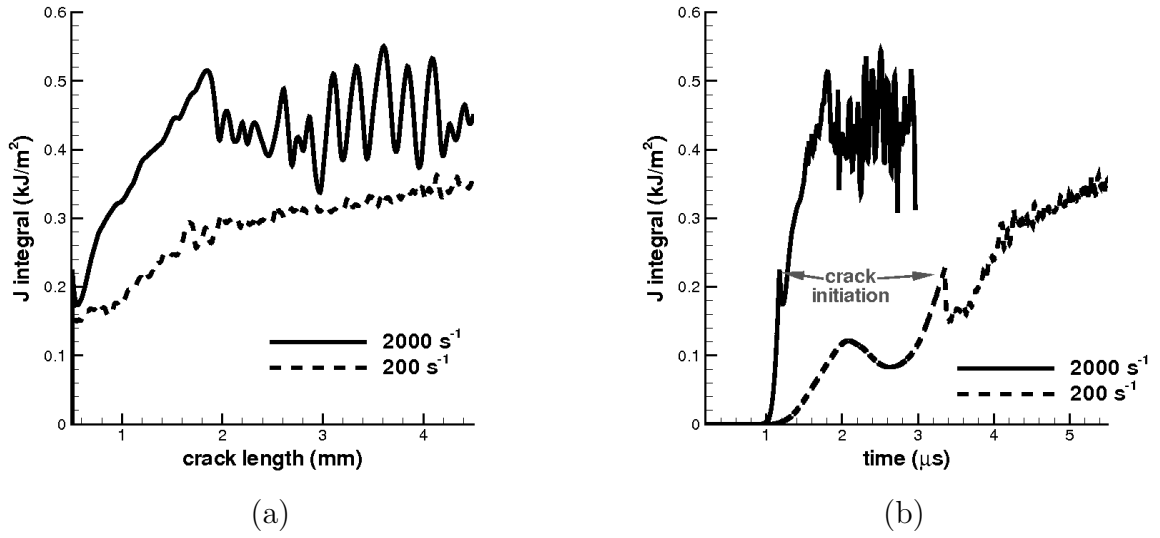
Figure 4.5: Variation of the J-integral with the crack extension in a W plate

can be used, we computed the J-integral defined by

$$J = \lim_{\Gamma \to 0} \int_{\Gamma} (w + T) dx_2 - \sigma_{ij} n_j \frac{\partial u_i}{\partial x_1} ds,$$

$$w = \int_0^t \sigma_{ij} D_{ij} dt, \ T = \frac{1}{2} \rho v_i v_i, \ u_i = x_i - X_\alpha \delta_{i\alpha}. \tag{4.5}$$

Here Γ is a closed contour enclosing the crack-tip, and ds is an element of arc length on Γ. Figure 4.5a shows the value of the J-integral as a function of the crack-tip location for the pure W specimen deformed at nominal strain-rates of 200 and 2,000/s. The contour Γ used to evaluate the J-integral appeared stationary to an observer situated at the crack-tip and, hence, moving with it. The contour Γ spanned 5 elements behind the crack-tip, 5 elements ahead of it and 10 elements perpendicular to the crack-axis (each element is a square of side length 4.63 μm and the starter crack of length 1000 μm). For an average strain-rate of 200/s, the J-integral increases monotonically signifying an increasing resistance to crack propagation. However, at the average axial strain-rate of 2,000/s, the J-integral first increases with an advance in the crack-tip but then oscillates wildly. These oscillations can not be attributed to the contour Γ used to evaluate J since a similar contour with respect to the crack-tip gave reasonable values of the J integral for all locations of the crack-tip at the lower strain-rate of 200/s and for earlier stages of the crack propagation in the plate deformed at an axial strain-rate of 2,000/s. The time history of the evolution of the J-integral is exhibited in Figure 4.5b where its values at the instants of crack initiation at different points are shown. Values of the J-integral at the instant of the first crack initiation

in the W-plate are the same and equal ~ 0.22 kJ/m^2 at nominal strain-rates of 200 and 2,000/s.

4.3.3   Simulation of Ductile Failure

In order to simulate crack propagation due to ductile failure we analyze plane strain thermo-mechanical deformations of a block of material with equal and opposite tangential velocities prescribed on its top and bottom surfaces as described in Section 4.2.1. Thus the steady-state nominal strain-rate is v_0/H, and equals 5,000/s for simulations discussed herein. The FE mesh used to analyze the problem is depicted in Figure 4.1b. The elements are of size 4.6×4.6 μm in the central and end portions but get larger in other regions. For the FG bodies, the composition varies in the horizontal direction only from either 0% W at the centroid to 100% W at the edges or vice-versa. The yield stress of the material in an area 4.6 μm thick and 200 μm long located symmetrically about the two centroidal axes was reduced by 30%; this defect acts as a nucleation spot for an ASB. Recall that a crack is assumed to open at a point when the effective plastic strain there equals 1.5; thus the crack opens inside the body, generating two crack-tips. It was found that the ASB-tips and the crack-tips propagate horizontally with equal and opposite velocities; thus their propagation to the right is described below.

Crack speed

Figures 4.6 and 4.7 depict the variation in the crack length, the ASB length, the crack-tip speed and the ASB speed as they advance in the two homogeneous materials, namely W and NiFe, and the FGM W2NiFe. For the NiFe2W FG plate, in spite of the rather strong defect at the centroid, the crack originated from points $(-L, 0)$ and $(L, 0)$ and propagated inwards. Thus it propagated from W rich region to NiFe rich region, and the situation is similar to that for crack propagation in the W2NiFe FG plate. An ASB initiates at a point when the effective plastic strain there equals 1.5; thus the difference between an ASB and a crack is that new thermally insulated traction free surfaces are created when a crack opens but the material is intact during the initiation and propagation of an ASB. The crack surfaces are always in contact with one another due to a compressive normal stress acting on them. In W, the time histories of the crack length and the ASB length and hence their speeds of propagation are virtually identical. However, in NiFe the crack length is larger than the ASB length. Hence the crack propagation speed is higher than the ASB speed. Except when the ASB/crack arrives at $x_1 = \pm L$, its speed increases from ~ 0.1 km/s at origination to ~ 1.8 km/s at the end. The crack accelerates slowly in the beginning but
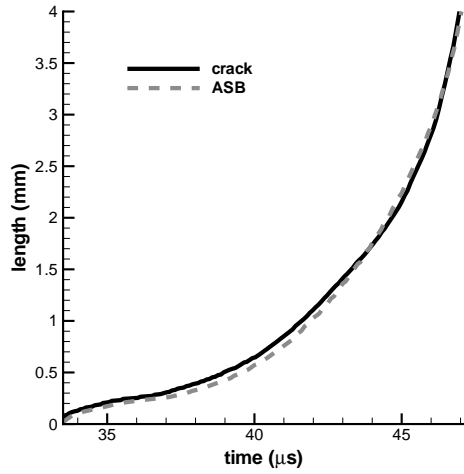
(a)
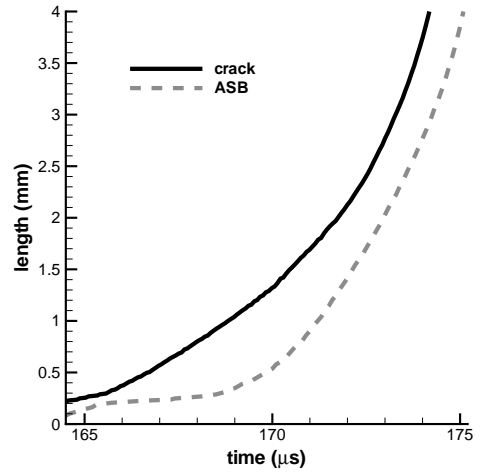
(b)
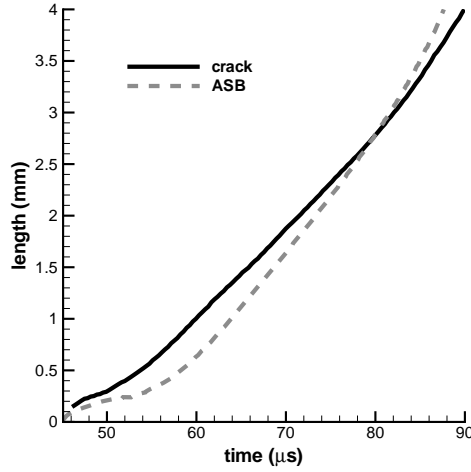
(c)

Figure 4.6: Time histories of the evolution of the ASB and the crack in (a) W, (b) NiFe and (c) W2NiFe plates deformed in plane strain shear

quite rapidly towards the end. Note that an ASB/crack initiates in NiFe at 165 μs but in W at 35 μs. Interestingly, the time histories of the crack propagation speeds in W and NiFe are nearly coincident. Whether it is so in all homogeneous materials remains to be seen. Had we assumed that an ASB forms at the effective plastic strain of 1.0 and a crack opens at the effective plastic strain of 1.5, the ASB length would have been larger than the crack length. However, their speeds of propagation would be essentially the same.
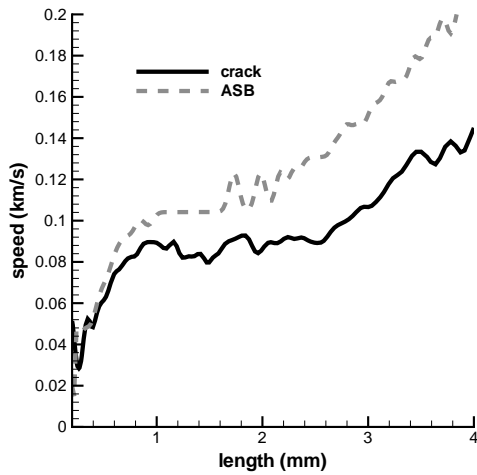
In W2NiFe FG plate, the ASB/crack initiation time is between those for the pure W and the pure NiFe plates; a similar situation occurs in the brittle failure of these materials. The ASB/crack propagation speed in the FG plate is significantly less (approximately by an order of magnitude) than that in either of its two constituents.
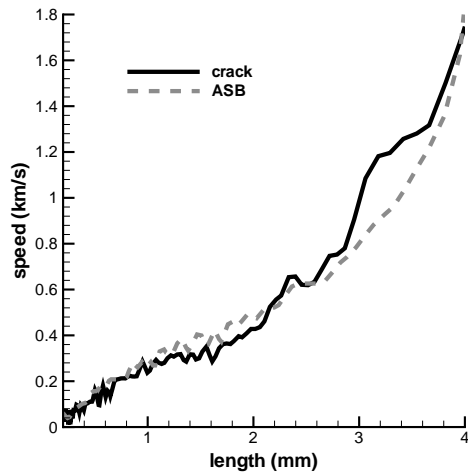
(a)
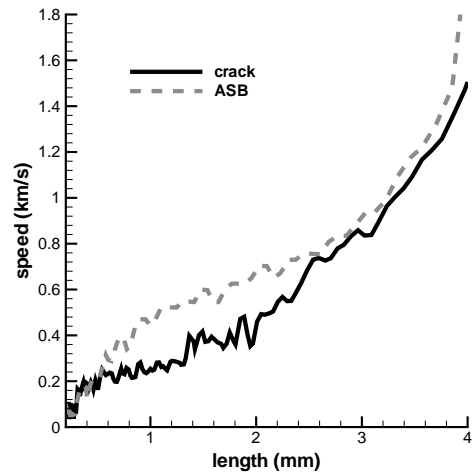
(b)

(c)

Figure 4.7: Variation of the crack and the ASB speeds in (a) W, (b) NiFe and (c) W2NiFe plates deformed in plane strain shear

We note that both the crack-tip and the ASB-tip do not advance monotonically. Rather, once a crack has opened at a node, it takes a little while for the fracture criterion to be met at the node immediately ahead of the crack-tip. Thus, the crack length as a function of time exhibits a stair-case pattern. Results plotted in Figure 4.6 have been smoothened.
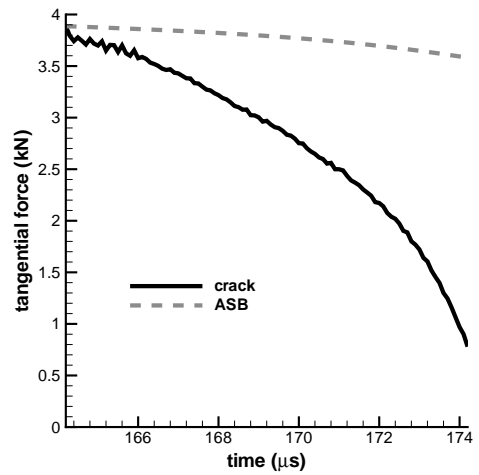
For ductile fracture, there are significant plastic deformations induced, so the J-integral is not evaluated.
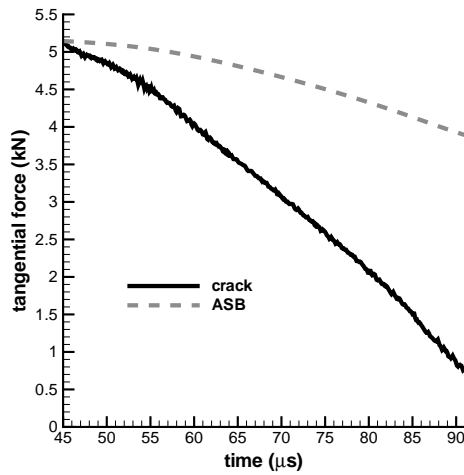
Tangential force

We have plotted in Figure 4.8 time-histories of the tangential force required to deform the specimen. Since the top and the bottom surfaces are constrained from moving in the vertical
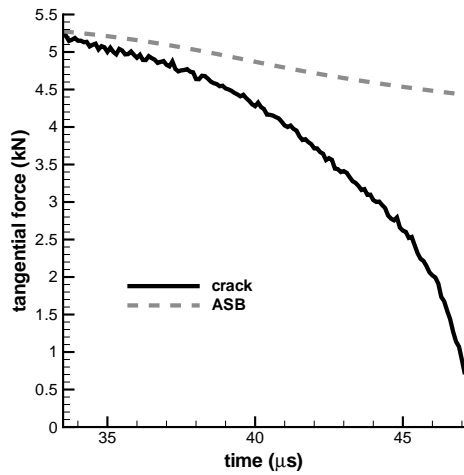
Figure 4.8: Time histories of the tangential force in (a) W, (b) NiFe and (c) W2NiFe plates deformed in plane strain shear

direction, the working of external forces is due to tangential tractions. Furthermore, this working is proportional to the tangential force as the tangential velocity, except for the first 1 μs, is constant. As expected the tangential force decreases with the opening of a crack and it continues to decrease as the crack elongates. With the crack extension, smaller surface area supports the external load. Also, with continued plastic deformations, the material softens and its capacity to support external load diminishes. The rate of decrease of the tangential force is higher for W than that for NiFe since the strain and strain-rate hardening effects are higher in NiFe than in W. With the extension of the crack, the tangential force drops more rapidly for the FG plate than that for the two homogeneous plates.
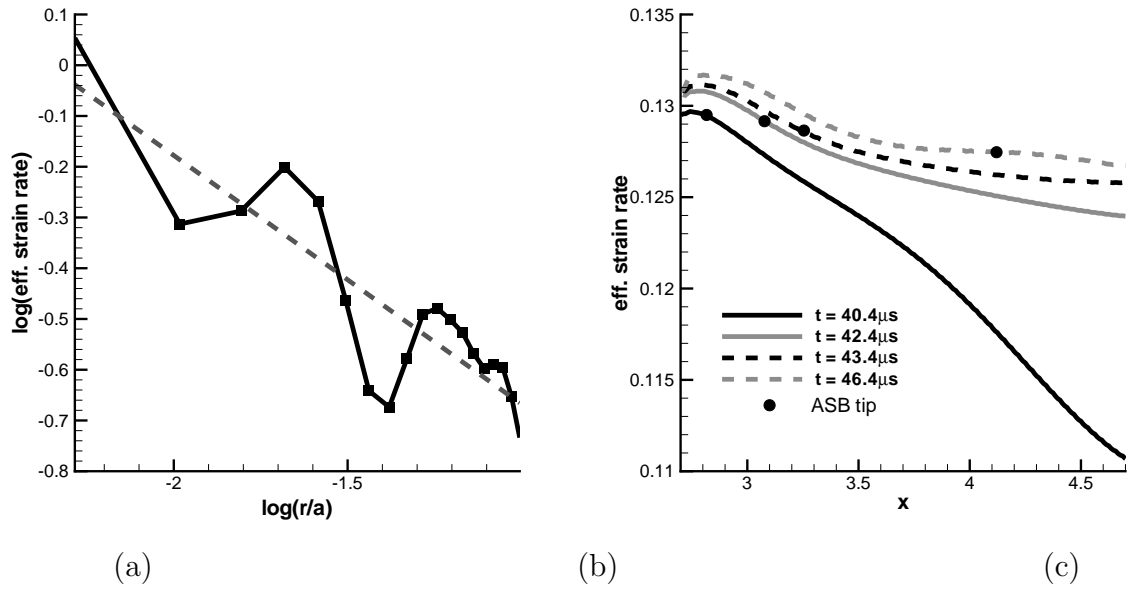
Figure 4.9: Effective strain-rates ahead of the tip in plates (a) with crack and (b) with ASB only; here a is the current length of the crack

4.3.4   Effect of Crack Opening on Deformation Fields

In order to delineate the differences, if any, between the deformation fields ahead of the ASB-tip and the crack-tip, we have plotted in Figure 4.9 the spatial variation of the effective plastic strain-rate in a W plate deformed at a nominal strain-rate of 5000/s with and without crack propagation. Because of the unloading elastic waves emanating from newly formed crack surfaces, the strain-rates ahead of the crack-tip are oscillatory; cf. Figure 4.9a. The slope of the line obtained by least squares fit to the computed values is about -0.4. Note that the effective plastic strain-rate at the crack-tip is finite, and the plot in Figure 4.9 is for $r/a \geq 10^{-2.3}$, where a is the current crack length. Results plotted in Figure 4.9b indicate that without cracking, once an ASB has developed, the spatial variation of the effective plastic strain-rate ahead of the ASB-tip varies very slowly and its value at the ASB-tip equals $\sim 1.31 \times 10^5$/s. It does not exhibit the singularity prevalent in the effective plastic strain-rate ahead of the crack-tip.

We have plotted in Figure 4.10a-c the distribution of the temperature rise in W, NiFe and W2NiFe plates at $t = 40$, 170 and 70 μs respectively. These times correspond to instants when the ASB/crack has propagated ~ 1 mm from the point of initiation. Temperatures at the ASB/crack-tips at these times are listed below. Thus the temperature rise at the crack-tip is nearly 14 K higher than that at the ASB-tip. For the case of no crack opening,

64

Table 4.3: Temperature rise at ASB/crack-tip

Material	ASB-tip (K)	Crack-tip (K)
W	512	526
NiFe	547	561
W2NiFe	546	561

(a)

(b)

(c)
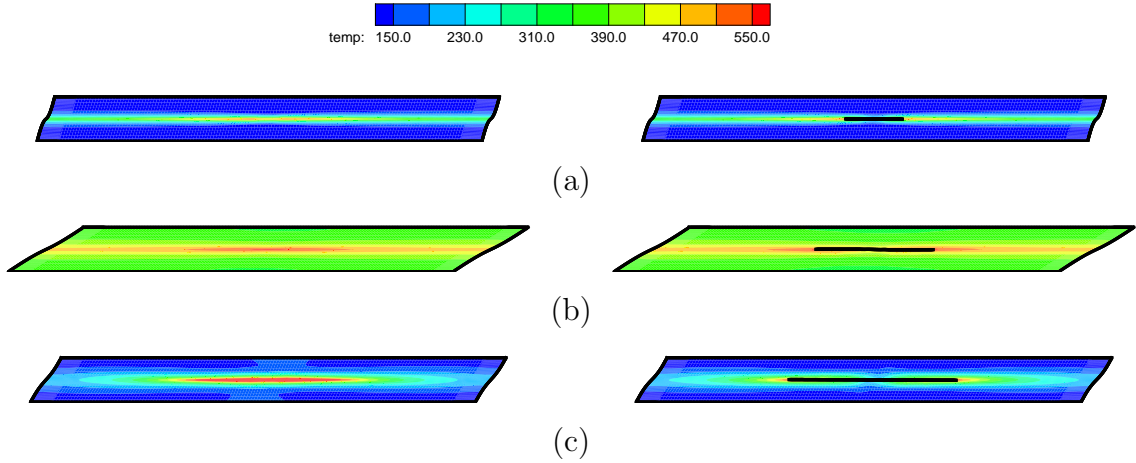
Figure 4.10: Temperature distribution in (a) W, (b) NiFe and (c) W2NiFe plates at $t = 40$, 170 and 70 μs, respectively. Plots on the left (right) are without (with) crack opening

the maximum temperature occurs at the specimen centroid and not at the ASB-tip. This is because, with the passage of time, the difference between the effective plastic strain at the specimen centroid from where an ASB first originated and that at the ASB-tip continues to increase; e.g. see Figure 4.9b. However, when a crack is formed, then the maximum temperature occurs at the crack-tip. Values listed in Table 4.3 depend upon the ASB/crack initiation criterion.

Relative sliding between surfaces

The relative sliding between the upper and the lower parts of the body is exhibited in Figure 4.11 that shows the deformed shape of a small region. It is clear that the part of the body occupying the region $X_2 > 0$ in the reference configuration has moved to the right relative to that in the domain $X_1 < 0$. Recalling that the FE mesh in the reference configuration has rectangular elements with sides parallel to the horizontal and the vertical axes, the two elements in the vertical direction next to the sliding/crack surface have been sheared

considerably more than those further away from the crack surface. The slight asymmetry in the results about the horizontal centroidal axis is attributed to numerical oscillations in the computed results. The smoothing of oscillations located the crack surface at $X_2 = 0.001$ rather than at $X_2 = 0.0$. At some points, the crack surface $X_2 = 0^+$ has moved over the crack surface $X_2 = 0^-$ by as much as four element lengths, or $\sim 18\mu m$.
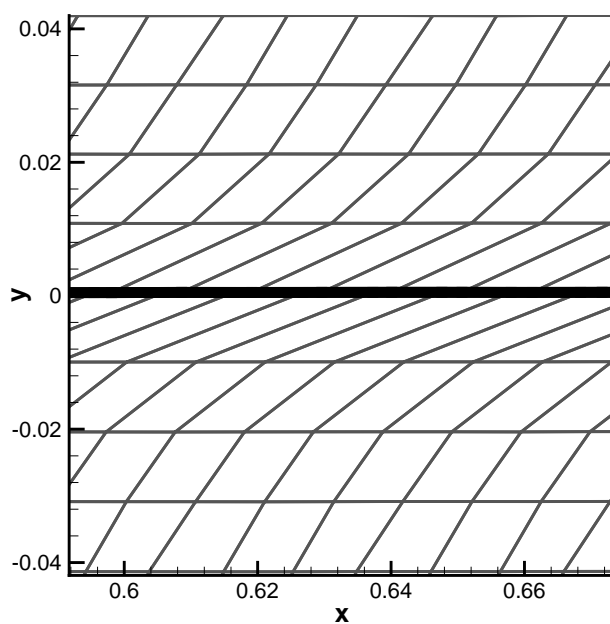

Figure 4.11: A section of the W plate deformed in plane strain shear showing relative sliding between the cracked surfaces

Porosity Evolution

The hydrostatic pressure in the material within the ASB, ahead of it and directly in front of the crack-tip was found to be compressive. Thus no new voids nucleated in the material even though it had enormous plastic deformations. The total porosity evolved in the intensely deformed region is rather minuscule.

4.3.5   Dependence of Results on FE Mesh

In Section 4.3.1 we showed that an element size of 100 $\mu m \times$ 100 μm for a FG linear elastic bar gives numerical results close to the analytical solution of the wave propagation problem. As shown in Table 3.1, the uniform FE meshes of element size 125 $\mu m \times$ 125 μm and 42 μm

$\times$ 42 μm gave ASB initiation times differing by 2.1%. Thus, FE meshes used herein should give reasonably accurate results. The CPU time needed to compute speeds of propagation of an ASB and a crack due to ductile failure in a FG body is close to 200 hours. Thus, results could not be computed with a FE mesh much finer than the one used here.

One way to eliminate the effect of FE mesh on computed results is to use a strain-rate gradient dependent viscoplasticity theory such as that employed in [97–99]. It introduces material characteristic lengths that can not be easily estimated.

4.4 Conclusions

We have analyzed the initiation and propagation of brittle and ductile fractures in homogeneous and functionally graded plates deformed either in plane strain tension at nominal strain-rates of 200 and 2,000/s or in plane strain shear at a nominal strain-rate of 5,000/s. It is found that for the crack propagating due to brittle failure at the nominal strain-rate of 200/s, the driving force is a non-decreasing function of the crack extension. At the higher strain-rate of 2,000/s the axial pulling force increases as the crack extends till the crack length equals approximately one-half the plate width, and it subsequently decreases. When the crack length in a NiFe plate deformed at an average strain-rate of 2,000/s equals about one-half the plate width, a large region of the material ahead of the crack-tip fails instantaneously signifying shattering of the plate. It is found that the NiFe plate shatters only if the nominal axial strain-rate exceeds 1,130/s, and the crack elongation prior to shattering varies with the nominal axial strain-rate. For the finite size plate studied here, the maximum computed crack speed in a FG plate pulled at a nominal axial strain-rate of 2,000/s is almost equal to the Rayleigh wave speed. For an FG plate, the Rayleigh wave speed varies with the position.

We have also analyzed ductile failure in a plate deformed in plane strain simple shear. It is found that in a W plate, an adiabatic shear band (ASB) and a crack propagate at virtually identical speeds. However, in a NiFe plate the crack speed is higher than the ASB speed in the beginning but the two are nearly equal after they have propagated for 15 μs. In W and NiFe plates, the crack speed increases from $\sim$ 0.05 km/s at the instant of initiation to $\sim$ 1.8 km/s when the crack-tip has approached the edge of the plate. However, in a FG plate with the crack propagating from W rich to W poor regions, the crack propagation speed is nearly steady for a certain interval, and its maximum value is about 1/10th of that in a homogeneous W or NiFe plate. The tangential force applied at the top and the bottom surfaces decreases as the ASB/crack extends, and is lower when a crack is allowed to open than that without the opening of a crack. The effective plastic strain-rate is finite at the

crack-tip but is singular ahead of the propagating crack-tip; the order of singularity is ~ 0.4. However, the effective plastic strain-rate ahead of a propagating ASB varies rather gradually and equals $\sim 1.3 \times 10^5$/s in a W plate deformed at a nominal strain-rate of 5,000/s. The temperature at a crack-tip is ~ 14 K higher than that at an ASB-tip.

Chapter 5

Comparison of Results from Meso- and Macro-level Computations of Adiabatic Shear Bands and Multi-scale Modeling

5.1 Problem Statement

Recall that in Chapter 2, we studied plane strain deformations of a RVE and found values of material parameters for the homogeneous medium so that the responses of the RVE and the homogenized medium in thermal and mechanical deformations were virtually the same. Naturally, the following question arises: will an ASB initiate at the same time when deformations of the individual constituents are modeled as compared to the case when deformations of the equivalent homogenized medium are scrutinized? In the former case, the two materials are presumed to be perfectly bonded together at their common interfaces. Because of differences in their acoustic and thermal impedances, mechanical and thermal waves are reflected and refracted from the interfaces between the two materials. Depending upon the number of particulates in the composite, these waves are reflected and refracted numerous times. However, in the homogenized material waves are only reflected from the outer bounding surfaces. The interaction among these waves and also their interaction with the incident waves result in an inhomogeneous deformation of the body. Below, we delineate the influence of the particulate size on the initiation and propagation of an ASB, and then compare the formation of an ASB with that in the equivalent homogenized medium.

5.2   ASBs in a Particulate Composite

As in Chapters 3 and 4, plane strain coupled thermomechanical deformations of the material in the first quadrant are analyzed. The 0.5 mm × 0.5 mm region is divided into 100 x 100 uniform 4-node quadrilateral elements. Keeping the volume fraction of W particulates fixed at 50%, random distributions of particulates of 40, 50, 60 and 75 μm in diameter, as shown in Figure 5.1, are considered. Boundary conditions arising from the presumed symmetry of deformations are applied on the bottom and the left edges, and the other two edges are taken to be thermally insulated. The right edge is traction free and the prescribed normal velocity on the top smooth surface increases linearly from 0 to 2.5 m/s in 1 μs and then stays steady. Thus the nominal axial strain-rate induced in the body is 5000/s. Figure 5.1 also exhibits time-histories of the axial loads for the four cases. As for a homogeneous body, with the continuous application of the axial velocity, the axial load first increases, reaches a plateau and then drops rapidly. Whereas the time history of the axial load exhibits oscillations for a homogeneous body (cf. Figure 3.3), it varies rather smoothly for the particulate composite. It suggests that the overall response to dynamic loads of a body containing a reasonably large number of particulates is smoother than that of a homogeneous body. Even though the peak axial load varies slightly with the particulate size, it occurs approximately at an axial strain of 0.08 for the four particulate sizes considered.

In order to delineate the initiation and formation of an ASB in a particulate composite, we have plotted in Figure 5.2 contours of the effective plastic strain at five different times, for the case with 40 μm diameter particulates. As the top surface is pulled axially with the prescribed velocity, the softer NiFe matrix undergoes more severe plastic deformations as compared to those of W particulates. In Figure 5.2a, there are several narrow regions of intense plastic deformation. During deformations of the body from $t = 30$ μs to $t = 40$ μs, the effective plastic strain has grown in many of these regions. However, it is hard to delineate where an ASB will eventually develop. There seems to be at least two regions of large plastic deformation in Figures 5.2c and 5.2d. Even at an average axial strain of 0.35 there are many regions where the effective plastic strain is nearly 100%. We now attempt to delineate which ones, if any, of these regions correspond to ASBs.

Figure 5.3 shows the axial stress σ_{yy} and the effective plastic strain as a function of time in the 40 μm particulate diameter composite at two points: a point inside W initially located at $(X_1, X_2) = (0.06, 0.4)$ and a nearby point located inside the NiFe matrix initially at $(0.085, 0.4)$. Note that the effective plastic strain is much higher in the NiFe matrix than in the W particulate and the axial stress is higher in the W than in the NiFe. Because of the assumption of perfect bonding between the two materials, displacements and surface
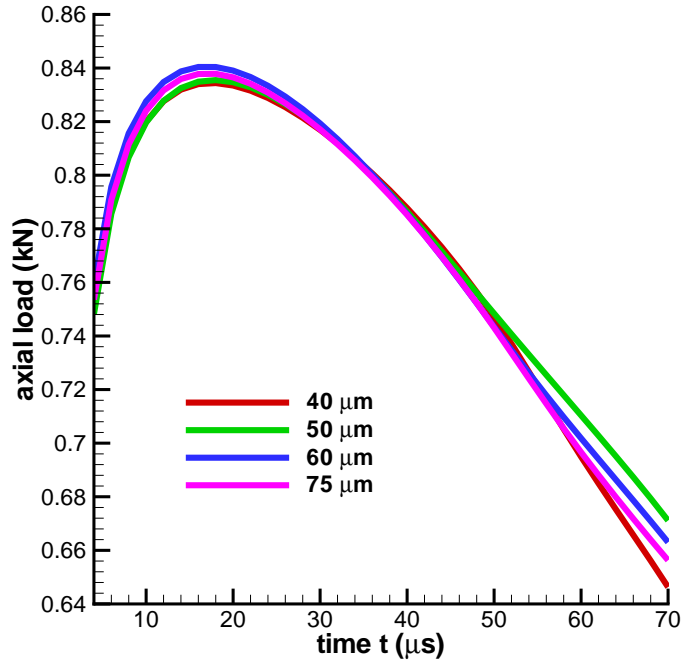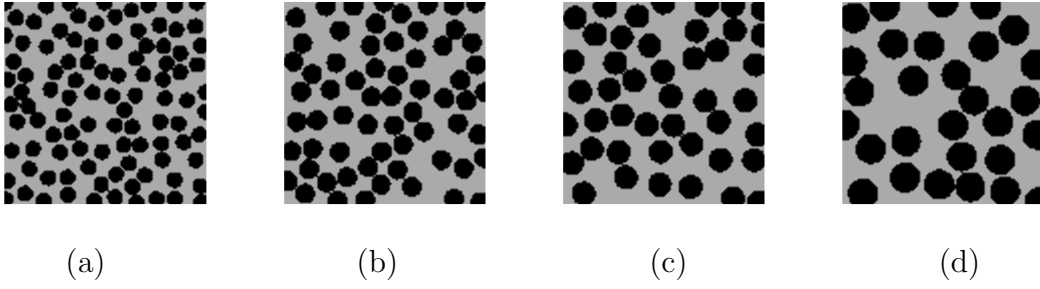
Figure 5.1: W (particulate)/NiFe (matrix) RVEs with particulate diameter (a) 40 μm, (b) 50 μm, (c) 60 μm, and (d) 75 μm; (e) axial load versus time for RVEs (a)-(d)

tractions at common interfaces between them are continuous. Even though the quasistatic yield stress of W is nearly three times that of NiFe, for $t > 10$ μs the effective stress in W is only a little higher than that in NiFe because of the large differences in their strain- and strain-rate hardening characteristics. However, results plotted in Figure 5.3b reveal that the effective plastic strain in W is less than one-fourth that in NiFe. Since the heat capacity ρc of W is approximately 24% higher than that of NiFe, the temperature rise is W is only slightly less than that of NiFe; this is depicted in Figure 5.3c. Thus the thermal energy density, $\rho c\theta$, in W is nearly 20% less than that in NiFe. The two materials are softened

thermally at different rates due to differences in their temperatures and thermal softening parameters. Thus effective plastic strain rates are different in the two materials. Results plotted in Figure 5.3b suggest that the effective plastic strain rate at the point in the NiFe matrix is considerably more than that in the W particulate. At $t \approx 70$ μs or the average axial strain of about 0.35, the effective plastic strain rate at the point in NiFe decreases noticeably.

For $t = 80.1$ μs and $t = 90.1$ μs, Figure 5.4 depicts points where the ASB initiation criterion adopted in Section 3.2.2 has been satisfied and also contours of the effective plastic strain. Points where the ASB criterion has been satisfied do not lie on a continuous curve and hence do not form a discernible ASB, despite the high levels of deformation exhibited in the corresponding contours of the effective plastic strain. It is thus clear that the ASB initiation criterion in a particulate composite is different from that in a body with either uniform or continuous variation of material properties.

After a close scrutiny of the spatial and the temporal variations of different measures of deformation, it was found that at late stages of deformation the spatial variations of velocity and the rate of change of temperature are similar. At points where the velocity varies sharply, the rate of increase of temperature is also very high. In locally adiabatic deformations, the rate of increase of temperature equals the energy dissipation rate/mass divided by the specific heat. In general, the heat conduction, the energy dissipation rate and the heat capacity influence the rate of temperature rise at a point.

For a particulate composite with 50% volume fraction of 40 μm diameter W particulates in NiFe matrix, Figure 5.5 evinces contour plots of the axial velocity and the rate of increase of temperature at an axial strain of 35%. It is clear that the axial velocity varies sharply across regions where the rate of increase of temperature is also extremely large. These results and those plotted in Figure 5.3b suggest that an ASB initiates at a point in the NiFe matrix at an average axial strain of $\sim$0.35.

One would like to replace the particulate composite with a homogeneous material with effective properties obtained from the technique described in Chapter 2. However, the particulate composite possesses many particulate/matrix interfaces that act as local defects, producing ASBs earlier than would be expected in a homogeneous material. We propose to simulate the cumulative effect of these defects in the homogeneous body with an initial porosity distribution given by equation 5.1.

$$f_0(\boldsymbol{X}) = \begin{cases} f_{ce}\left(1 - \frac{r}{H}\right), \ 0 \leq r \leq H \\ 0, \ r \geq H \end{cases} \tag{5.1}$$
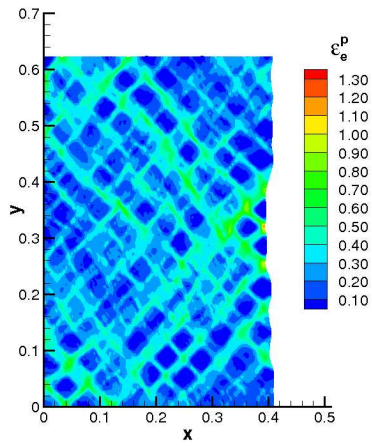
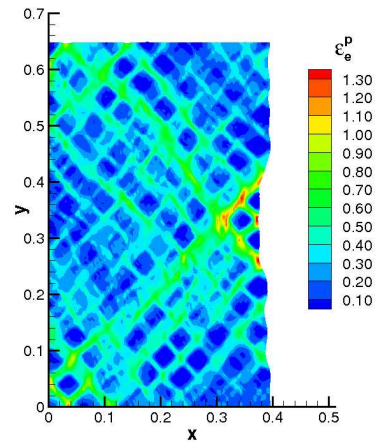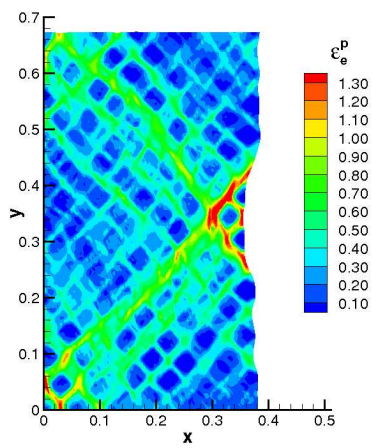Here $r = \sqrt{X_\alpha X_\alpha}$, is the distance from the centroid in the reference configuration and
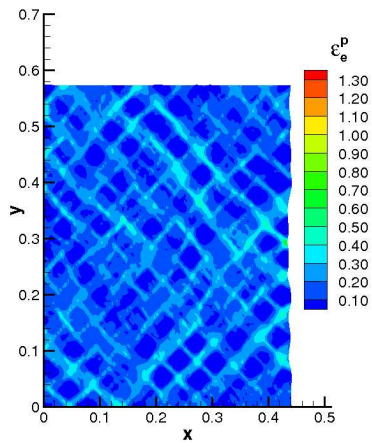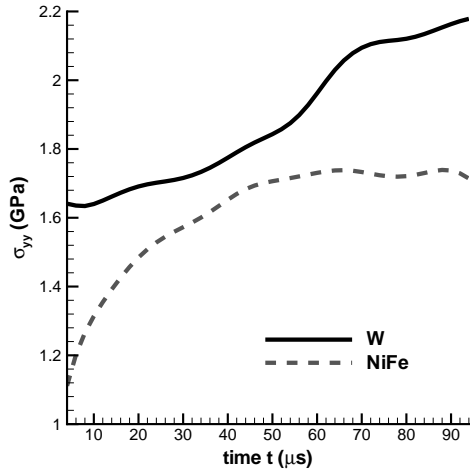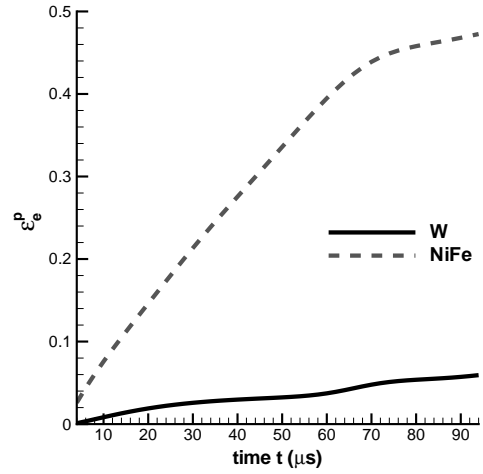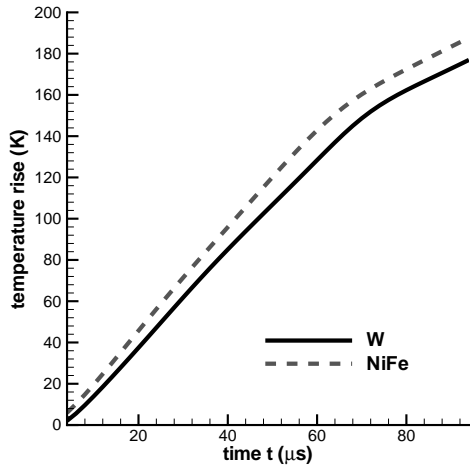
(a)
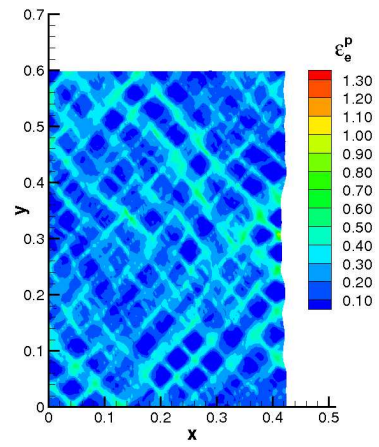
(b)

(c)

(d)

(e)

Figure 5.2: Contours of effective plastic strain for an RVE with W particulates of diameter 40 μm at (a) 30 μs, (b) 40 μs, (c) 50 μs, (d) 60 μs, and (e) 70 μs

(a)

(b)

(c)

Figure 5.3: Time histories of (a) axial stress, (b) effective plastic strain, and (c) temperature rise at two nearby points, one inside a particulate and the other in the matrix for the 40 μm particulate diameter composite

$H = 0.5$ mm is the height of the specimen. The porosity f_{ce} at the centroid is varied such that the rate of increase of temperature inside the ASB in the particulate composite and the homogeneous material are similar. Figure 5.6 shows the rate of increase in temperature as a function of time for several points inside the ASB in the particulate composites and the rate of increase in temperature at the centroid of an equivalent homogeneous body for different values of f_{ce}. The points in the particulate composites were selected in local regions of intense plastic deformation that also have a large rate of change of temperature. Note that the rate of increase of temperature for the homogeneous body increases monotonically with time; that for the particulate composites show some fluctuation at different points. Furthermore, at any time t several points in a particulate composite exhibit heating at similar rates. This
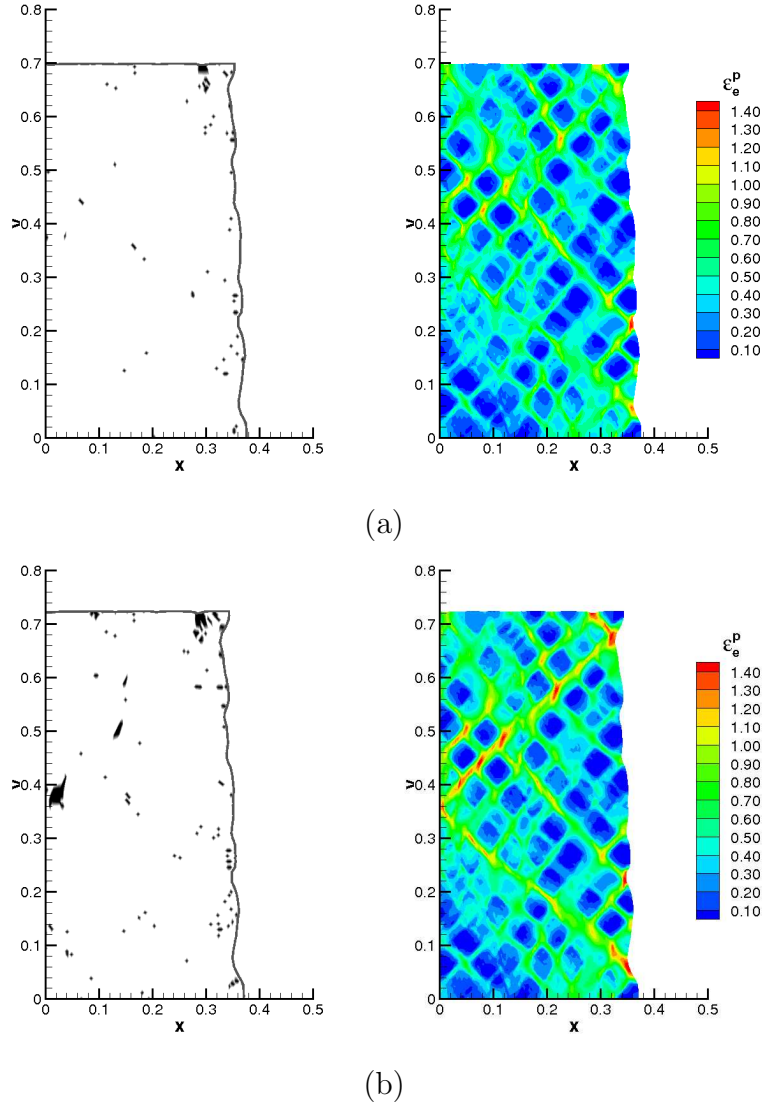
Figure 5.4: Points satisfying the ASB initiation criterion of Section 3.2.2 and contours of effective plastic strain in a W/NiFe particulate composite with 50 μm diameter tungsten particulates at (a) 80.1 μs and (b) 90.1 μs

behavior is not seen in the homogeneous body, where the centroid is heated more rapidly than other points in the body. These severely heated points in a particulate composite may be disconnected. In a homogeneous body, the ASB originates at the centroid and propagates at 45° in the present configuration. ASB formation and propagation in the particulate composite is more complex–ASBs may originate either simultaneously or sequentially at several points and then connect, forming the noticeable shear band.

Dai et al. [13] studied ASB initiation in a composite body comprised of SiC particles immersed in aluminum. The specimens were twisted in a split Hopkinson bar with presumably
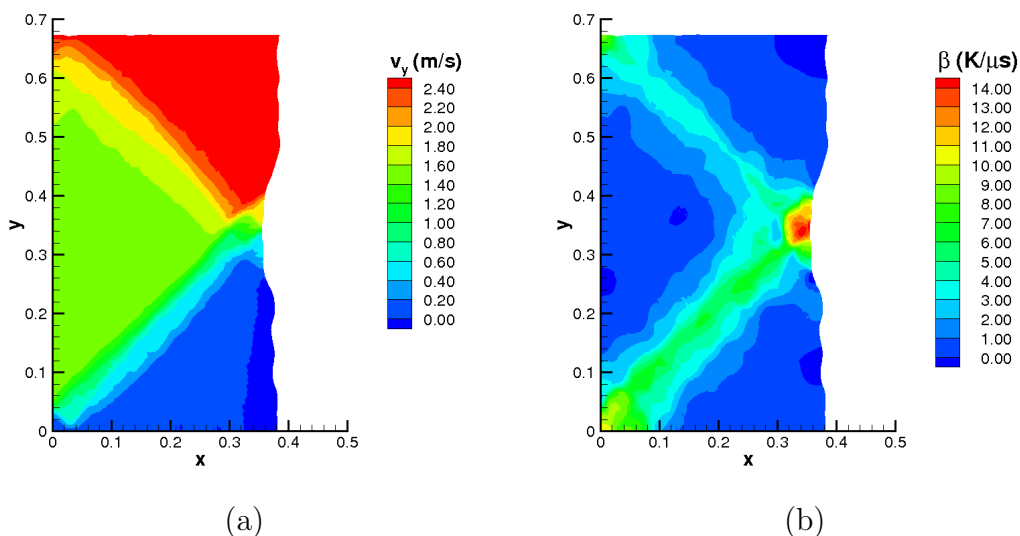
Figure 5.5: Contours of (a) axial velocity and (b) rate of increase of temperature in a particulate composite with 40 μm diameter particulates at an axial strain of 35%

the same torsional impulse. They found that the maximum shear strain induced in particulate composites increased with a decrease in the particulate diameter. They explained this by conjecturing that strain gradients increase with a decrease in the particulate diameter and this provides a driving force for the ASB initiation. Batra and Kim [100] numerically simulated displacement controlled simple shearing deformations of simple and dipolar materials and showed that the consideration of strain-rate gradients and the corresponding higher-order stresses delays the initiation of an ASB. In order to see how strain gradients depend upon the particulate size, we have plotted in Figure 5.7 the spatial variation on the line $x_2 = 0.4$ mm of the effective plastic strain for the four particulate sizes considered when the average axial strain in each composite equals 0.25. These plots confirm Dai et al.'s conjecture. However, one can not conclude from our simulations that ASBs initiate sooner with a decrease in the particulate diameter. We note that the composite studied by Dai et al. is comprised of SiC particles disbursed in 2024 aluminum and most likely the SiC particles are hardly deformed, though this is not clear from the micrographs included in [13]. Furthermore, the SiC particles considered had diameters of 3.5 μm, 10 μm, and 20 μm and were present in very small volume fractions. Zhou [101] has analyzed ASBs in plane strain simple shear deformations of composites comprised of 75.4% W particulates in a NiFe matrix and considered particulate diameters of 10 μm, 5 μm, and 2.5 μm. A sharp notch provided a nucleation site for an ASB. It was found that the ASB initiation time decreased
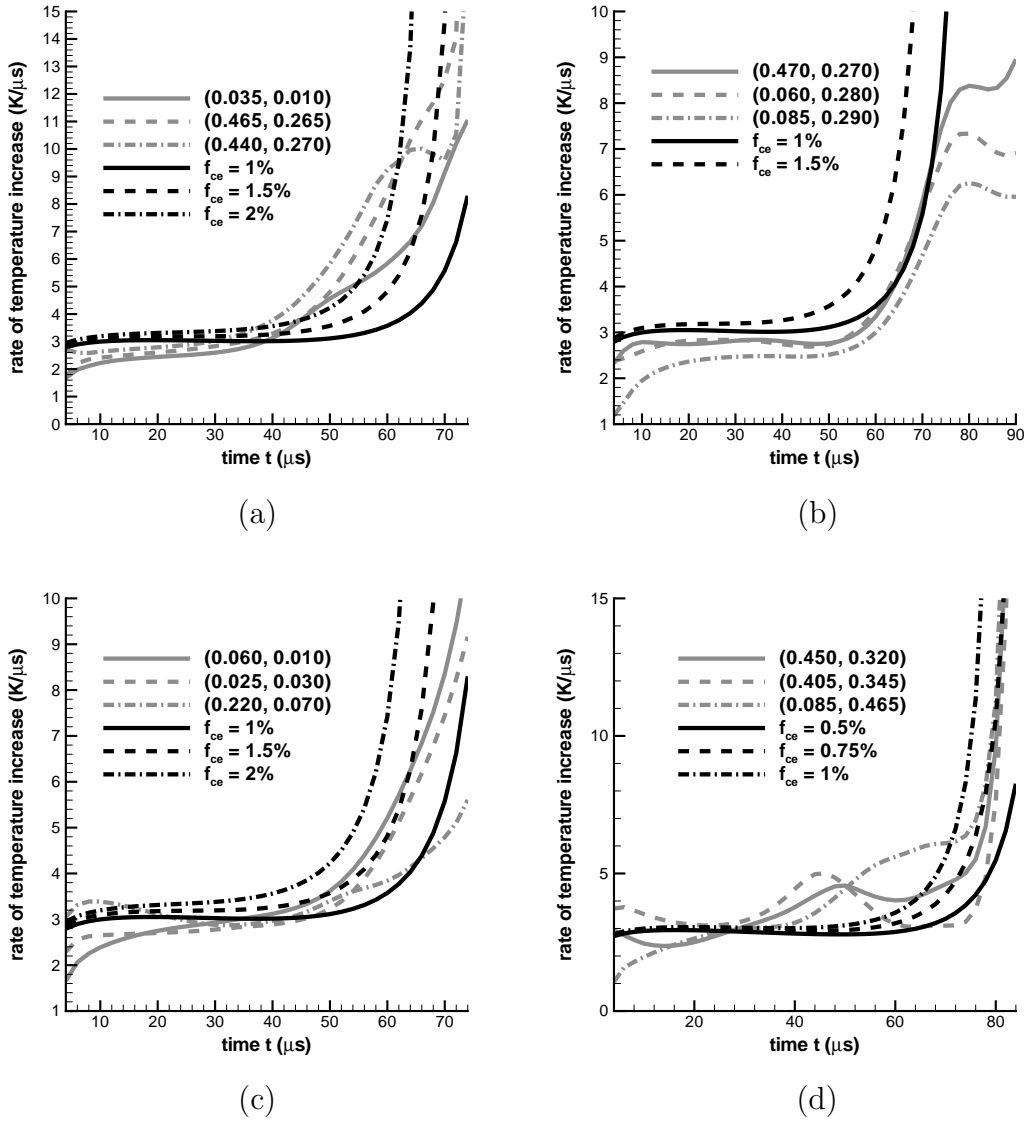
Figure 5.6: Rate of increase in temperature at a point inside the ASB in 50/50 W/NiFe particulate composites with particulate diameters of (a) 40 μm, (b) 50 μm, (c) 60 μm, and (d) 75 μm, as well as the rate of increase of temperature at the centroid of equivalent homogeneous bodies with nonuniform initial porosity; coordinates denote the position of the point in the particulate composite in the reference configuration.

with a decrease in the particulate diameter because smaller particles facilitated the turning of an ASB into the relatively weak matrix.

In order to assess the effect of the particulate arrangement, we have plotted in Figure 5.8 contour plots of the axial velocity for three different random distributions of 50 μm diameter particulates. It is clear that the particulate placements strongly influence when and where

an ASB initiates. For example in Figure 5.8a, an ASB seems to have originated from a point on the vertical centroidal axis and propagated at $\pm45^o$, but in Figure 5.8c, the origin of the ASB is at a point on the free surface and it propagated only towards the centroid of the cross-section. Furthermore, the times of initiation equal $\sim$90 μs and 60 μs for particulate distributions of Figures 5.8a and 5.8c, respectively. For the particulate distribution of Figure 5.8b, there is no narrow region across which the axial velocity increases sharply. The plots of the rate of temperature increase depicted in Figure 5.9 support the aforementioned remarks. The variation of the effective plastic strain on the line $x_2 = 0.4$ mm is exhibited in Figure 5.10. It is apparent that strain gradients are higher for the particulate arrangement of Figure 5.10b than those for the other two arrangements analyzed. The time histories of the rate of temperature rise evinced in Figure 5.11 suggest that an ASB initiates at $t \approx 60$ μs. There is less variation in the ASB initiation time than in the contour plots of the axial velocity and the rate of temperature increase. An initial affine porosity variation with approximately 1.5% porosity at the specimen centroid in the equivalent homogenized body will result in the ASB initiating at $t \approx 60$ μs.

We note that the time histories of the axial load plotted in Figure 5.1 indicate that the drop in the axial load to 80% of its peak value occurs at 64 μs $\leq t \leq$ 68 μs for the four particulate diameters. Whether or not it can be used as a criterion for the ASB initiation remains to be investigated.
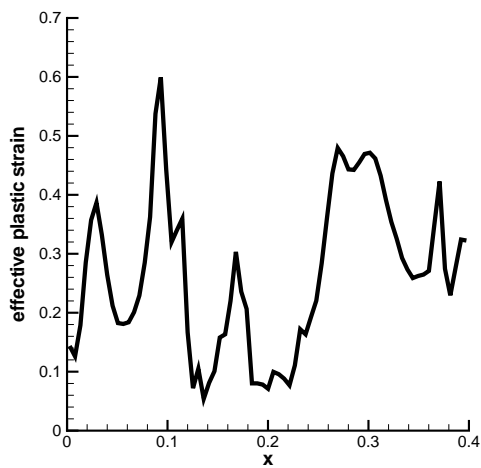
The particulate diameters considered here are typical of those employed by Dick et al. [102] in their experiments on tungsten heavy alloys.
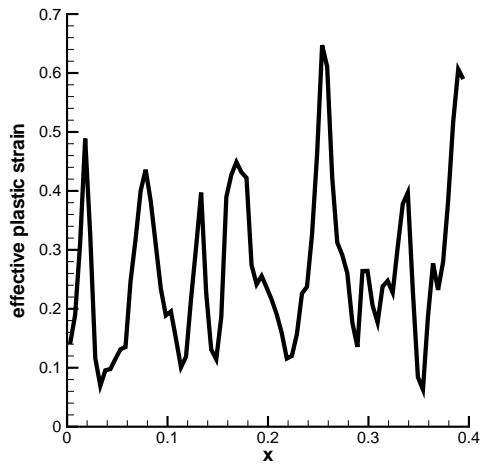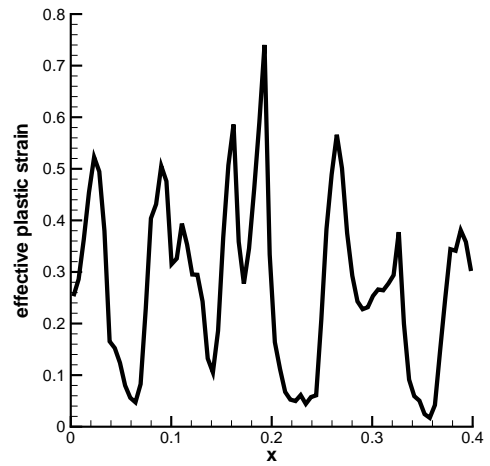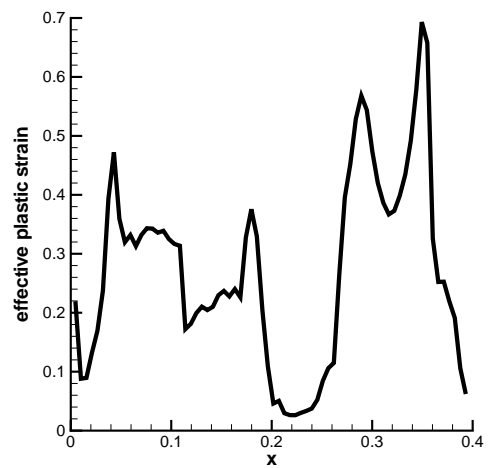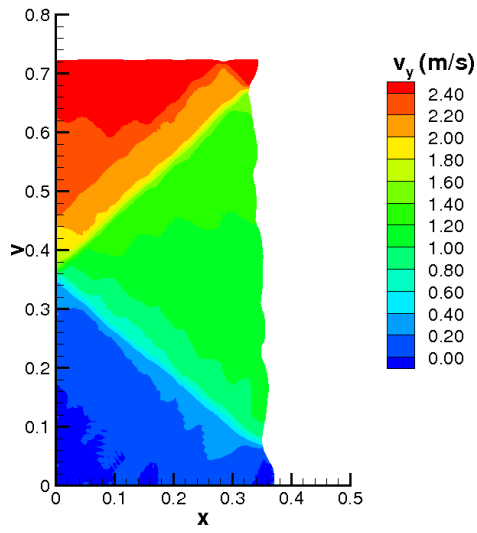
Figure 5.7: At an average axial strain of 0.25, variation of the effective plastic strain along $x_2 = 0.4$ mm for particulate composites with particulate diameters of (a) 40 μm, (b) 50 μm, (c) 60 μm, and (d) 75 μm

(a)

(b)

(c)

Figure 5.8: Contours of the axial velocity for three different random arrangements of 50 μm diameter particulates: (a) arrangement 1 at 90 μs, (b) arrangement 2 at 70 μs, and (c) arrangement 3 at 60 μs.
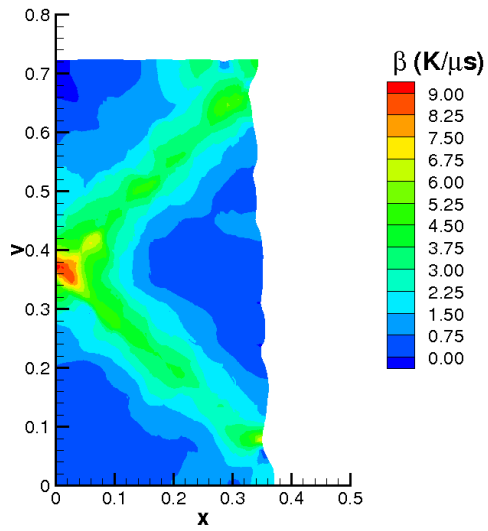
(a)
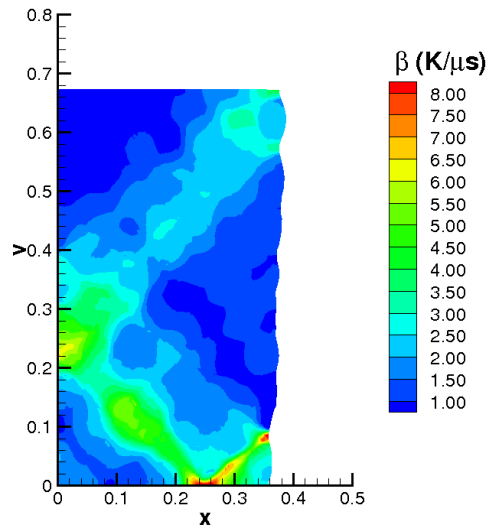
(b)
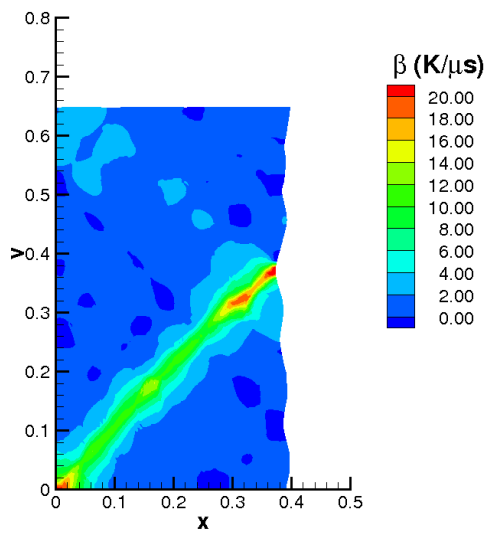
(c)

Figure 5.9: Contours of the rate of change of temperature for three different random arrangements of 50 μm diameter particulates: (a) arrangement 1 at 90 μs, (b) arrangement 2 at 70 μs, and (c) arrangement 3 at 60 μs.
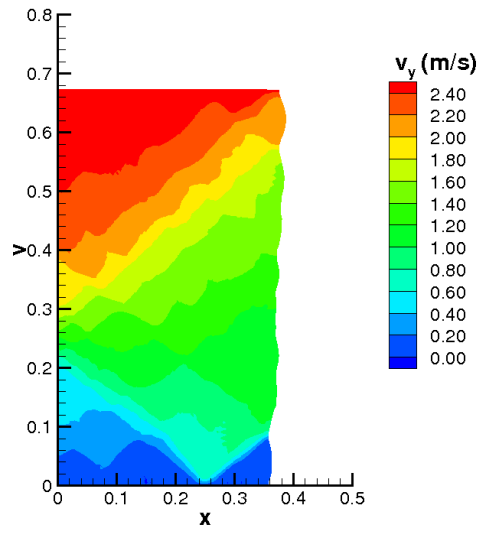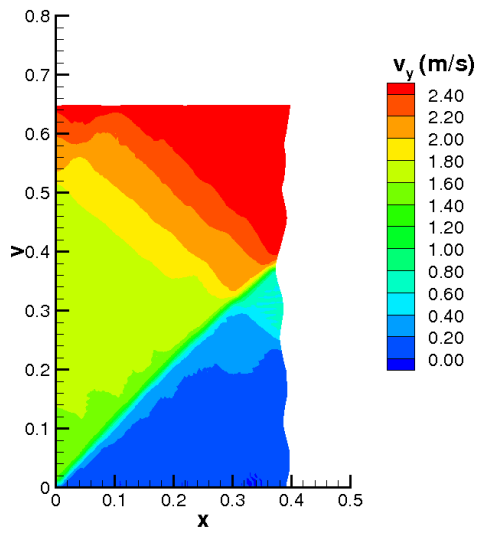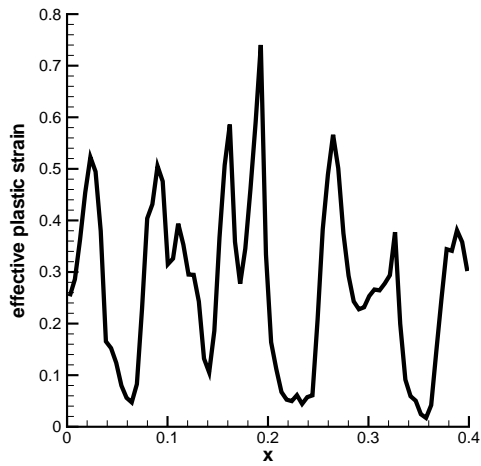
(a)
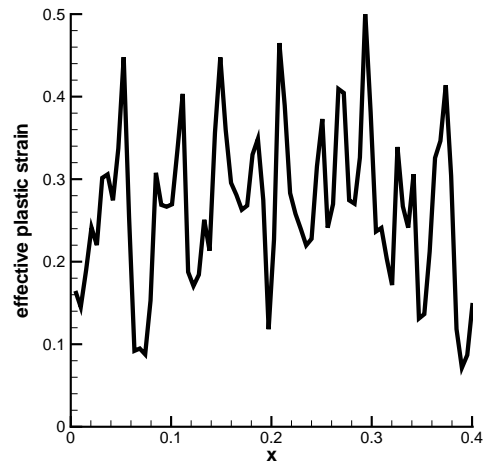
(b)
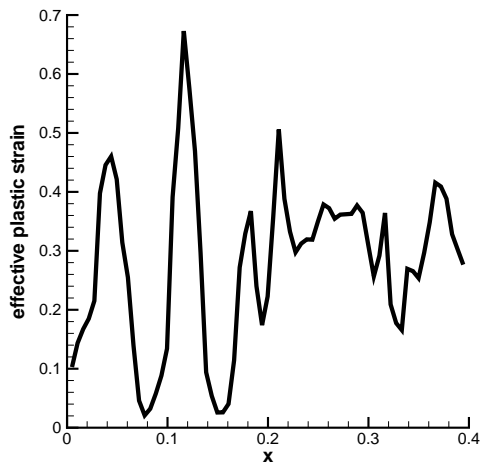
(c)

Figure 5.10: At an average axial strain of 0.25, variation of the effective plastic strain along $x_2 = 0.4$ mm for particulate composites with randomly distributed 50 μm diameter particulates: (a) arrangement 1, (b) arrangement 2, and (c) arrangement 3
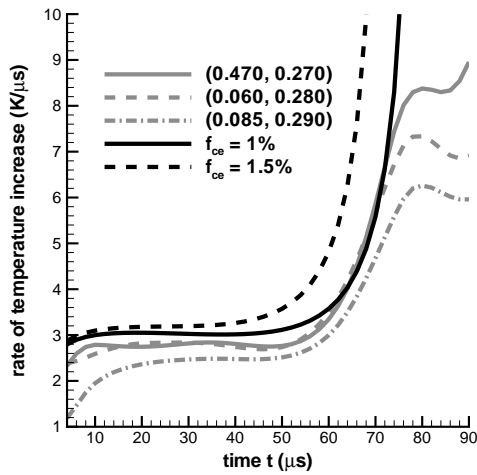
(a)
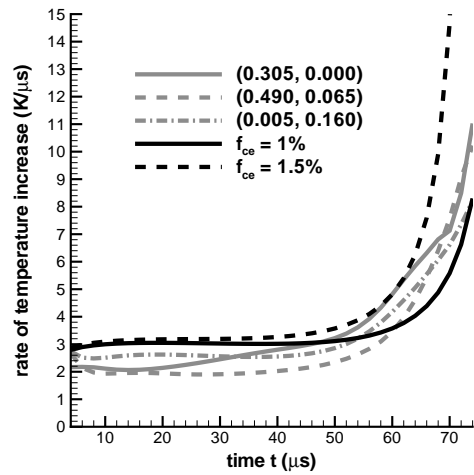
(b)
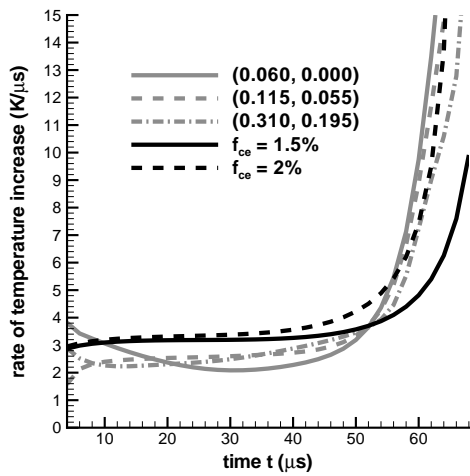
(c)

Figure 5.11: Rate of increase in temperature at a point inside the ASB in 50/50 W/NiFe particulate composites with particulate diameters of 50 μm for (a) arrangement 1, (b) arrangement 2, and (c) arrangement 3, as well as the rate of increase of temperature at the centroid of equivalent homogeneous bodies with nonuniform initial porosity; coordinates denote the position of the point in the particulate composite in the reference configuration.

5.3 Multiscale Modeling

We first analyze the initiation and development of an ASB in a prismatic body of 10×10 mm square cross-section deformed in plane strain tension. The body is made of a homogenized material whose response is equivalent to that of a 50% volume fraction W particulate composite with 50 μm diameter W particulates in the NiFe matrix; material parameters of the homogenized body are ascertained by using the procedure outlined in Chapter 2. As in the previous studies discussed in Chapter 3, symmetries about the two centroidal axes are exploited and coupled thermomechanical deformations of the material in the first quadrant are analyzed. The 5 mm $\times$ 5 mm region is divided into a uniform 100 x 100 FE mesh of 4-node quadrilateral elements. The initial porosity distribution is given by equation (5.1) with $f_{ce} = 0.025$, and it is deformed at a nominal strain-rate of 5,000/s till plastic deformations have localized into a narrow region. The time histories of 13 unknowns at nodes on the surfaces $X_1 = 1$ mm and $X_2 = 1$ mm in the undeformed configuration are recorded for later use. Subsequently, detailed deformations of the material in the 1 mm $\times$ 1 mm region with two edges along the centroidal axes of the original cross-section are analyzed. As shown in Figure 5.12, the 0.5 mm $\times$ 0.5 mm region has 50 μm diameter W particulates randomly distributed in the NiFe matrix and the remaining region is the homogenized material equivalent to the particulate composite. On the surfaces $X_1 = 1$ mm and $X_2 = 1$ mm the time history of surface tractions (normal and tangential stresses) and of temperature as computed from the previous analysis is applied with the remaining two surfaces having the same boundary conditions as in the original analysis of the 5 mm $\times$ 5 mm region. Numerical experiments with the velocity and the temperature prescribed on the surfaces $X_1 = 1$ mm and $X_2 = 1$ mm failed because of severe differences in deformations of particles on the common interface between the homogenized medium and the particulate composite. However, these experiments were successful for a homogenized body and the two approaches yielded identical results. With tractions assigned on the surface $X_1 = 1$ mm and $X_2 = 1$ mm, deformations of these and other particles adopt readily to the constraints imposed by the stiffer W particulates. It should be added that, in the reference configuration, nodes on the top and the right surfaces of the 1 mm $\times$ 1 mm mesh coincide with those on the surfaces $X_1 = 1$ mm and $X_2 = 1$ mm in the 5 mm $\times$ 5 mm mesh, respectively.

5.3.1 Verification of the Methodology

The aforementioned approach was used to analyze deformations of a homogeneous body. Figure 5.13 compares the time histories of the temperature and rate of increase of temperature of a material particle located at the specimen centroid obtained by the two procedures,
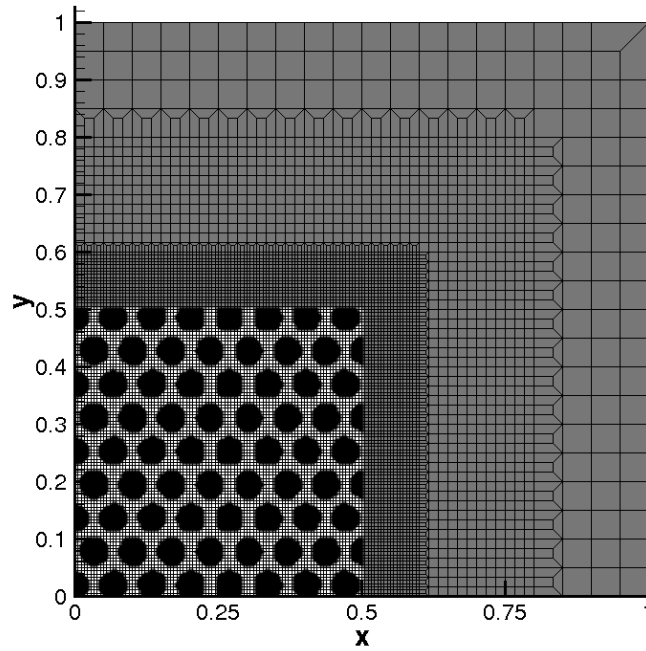
Figure 5.12: FE mesh for the sub-section in the multiscale analysis

and Figure 5.14 depicts contours of the effective plastic strain at an average axial strain of 0.29 in the macro-scale analysis. It is clear that the average axial strain in the 1 mm × 1 mm subsection is more than 0.29. The rate of increase of the temperature is much higher in the micro-macro analysis than in the pure macro analysis. The combined analysis can be viewed as refining the FE mesh and as shown by Batra and Ko [21] the effective plastic strain rate at the ASB center increases when FE mesh is refined. The ASB initiates, as signified by the jump in the rate of temperature increase, slightly earlier for the macro-micro analysis as compared to that for the macro analysis; the difference between the two times is ∼7%. The intensely deformed region is significantly narrower for the macro-micro analysis than that for the macro analysis. In Figure 5.14a,b the right edge is not straight because it is an inner surface in the 5 mm × 5 mm cross-section. For the same reason, the average axial strain in this 1 mm × 1 mm region need not equal the average axial strain of 0.29 in the 5 mm × 5 mm region. This micro-macro analysis could be repeated several times to fully resolve an ASB.

Figure 5.13: (a) Temperature and (b) rate of increase of temperature versus time at the centroid of a homogenized (50% W, 50% NiFe) body for the macro and the macro-micro analyses

Figure 5.14: Contours of effective plastic strain for a homogenized 50/50 W/NiFe sample at an average axial strain of 0.29 for $X_1 \leq 1$ mm and $X_2 \leq 1$ mm for the (a) macro-scale analysis and (b) macro-micro analysis
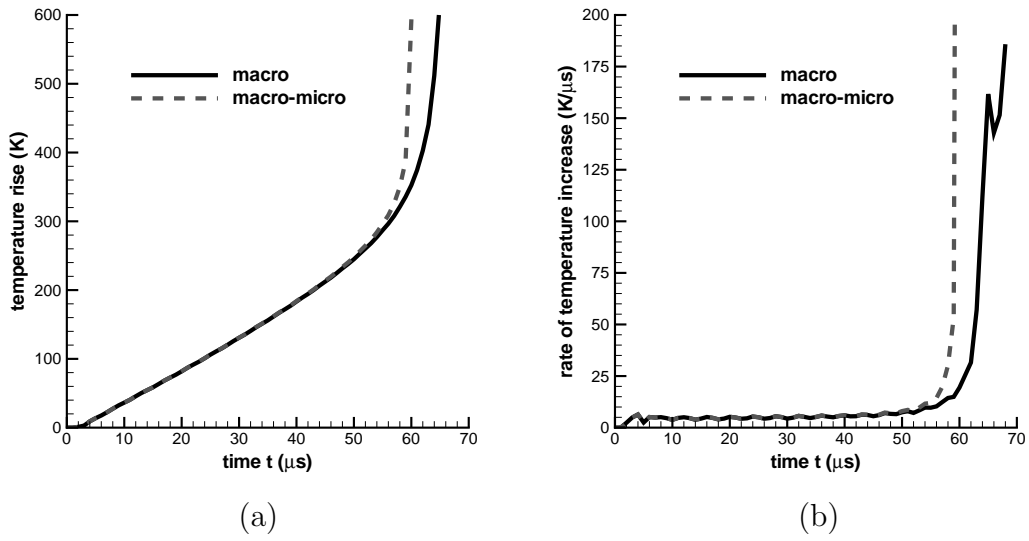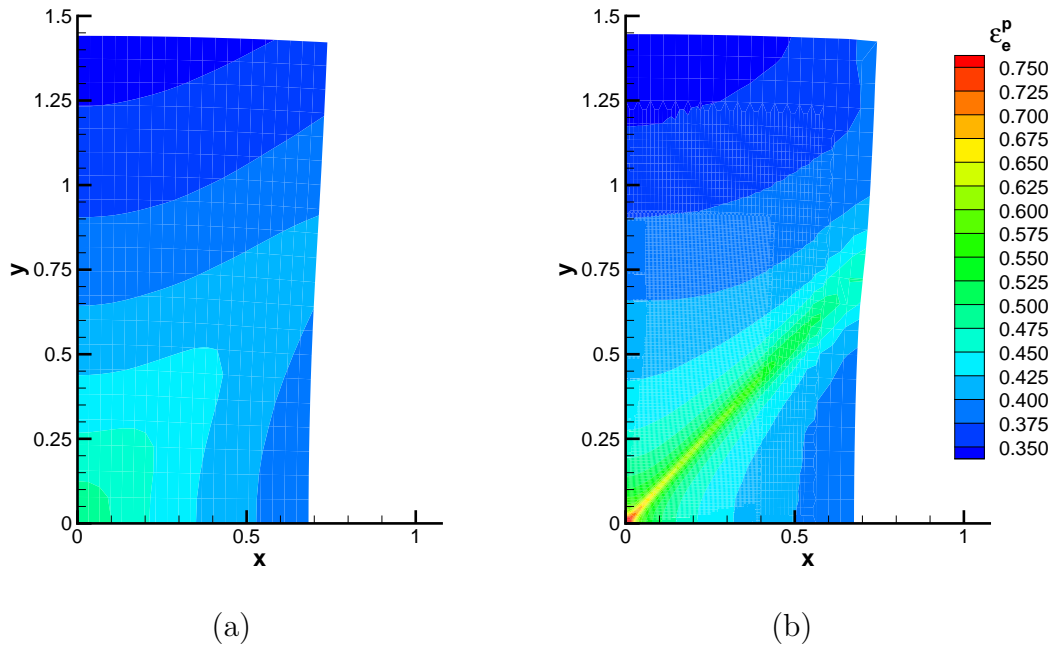
5.3.2   Results for the Particulate Composite

The above described procedure was applied to four different distributions of 50 μm diameter W particulates disbursed in the 0.5 mm $\times$ 0.5 mm region. Figure 5.15 depicts contours of the effective plastic strain and Figure 5.16 contours of the rate of increase of temperature for the four distributions. It is evident that an ASB initiates from a different point in each case. Furthermore, intense plastic deformations occur in different regions in the four cases, and only one of these agrees with the general shape of the intensely deformed region in the equivalent homogeneous body; c.f. Figure 5.9. The ASB center can be located from a visual inspection of the contour plots of Figures 5.15 and 5.16; its location does not coincide with the origin or the centroid of the cross-section, where the initial porosity is maximum. The inhomogeneities induced by the presence of W particulates strongly affect where and when an ASB initiates. For the four distributions of W particulates, we have plotted in Figure 5.17 time histories of the rate of temperature rise and the effective plastic strain at the ASB center. The ordered and the three random distributions of particulates give ASB initiation times between 22 and 24 μs which is considerably sooner than the nearly 60 μs deduced from the meso-scale results plotted in Figure 5.6b. The large difference between the two values can not be attributed to the considerably finer mesh employed in the micro analysis; the reasons are a subject for future investigations. The deformed configuration plotted in Figure 5.15 suggest that the nominal axial strain for the three random distributions is essentially the same but is slightly less than that for the ordered distribution of particulates.
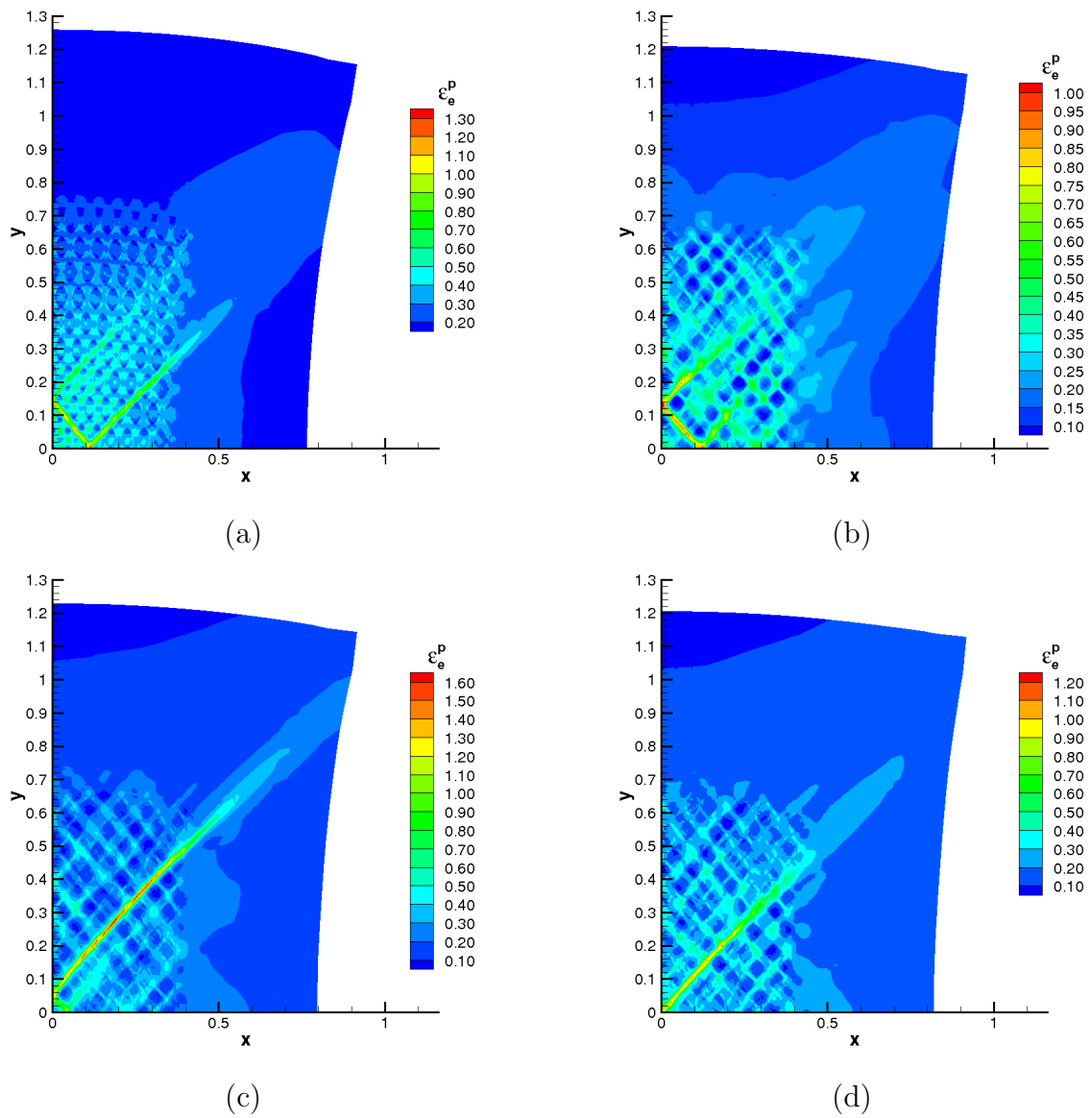
Figure 5.15: Contours of the effective plastic strain at $t = 25$ μs for (a) an ordered particulate arrangement and (b)-(d) three random particulate arrangements
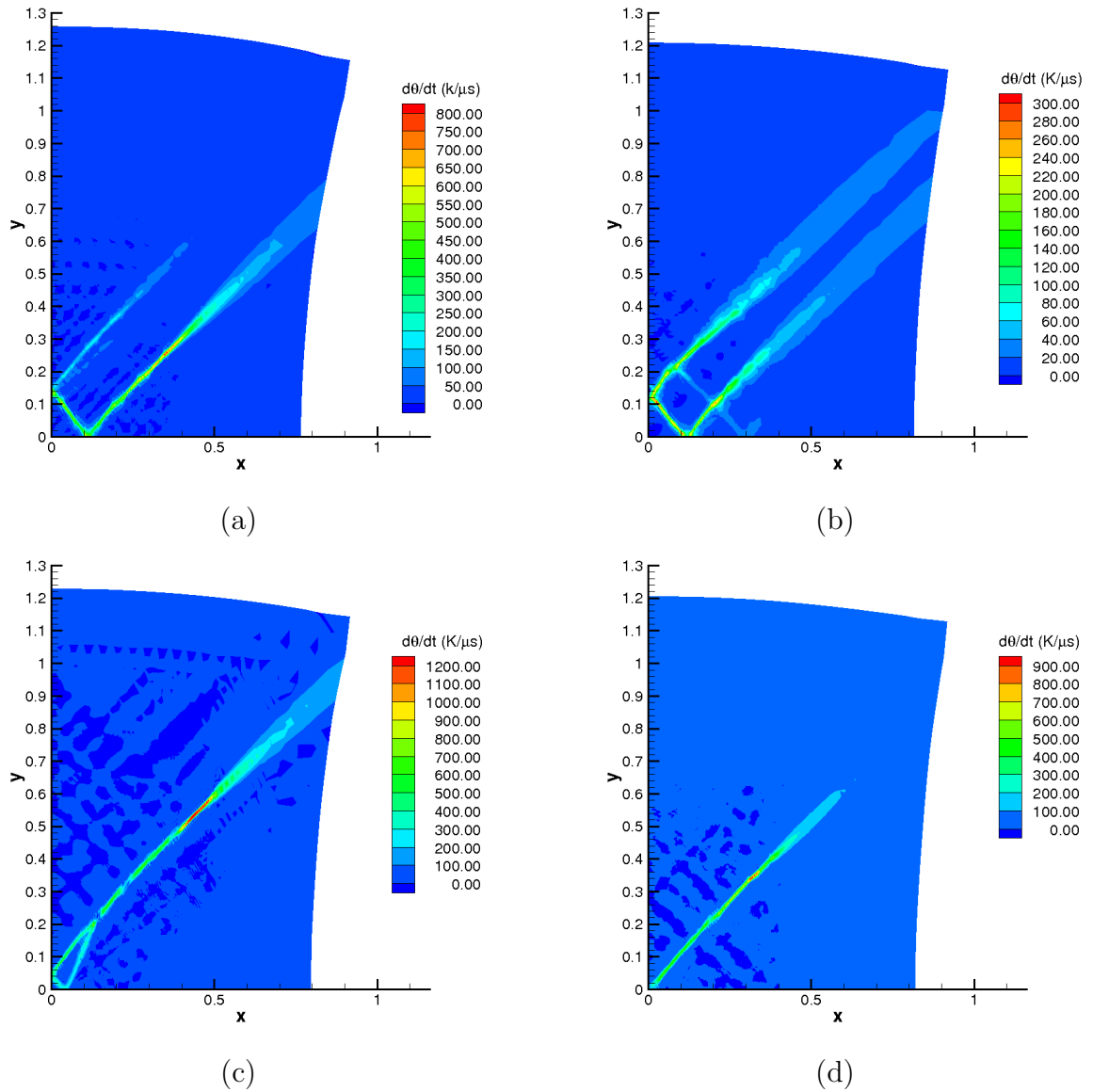
Figure 5.16: Contours of the rate of increase in temperature at $t = 25$ μs for (a) an ordered particulate arrangement and (b)-(d) three random particulate arrangements
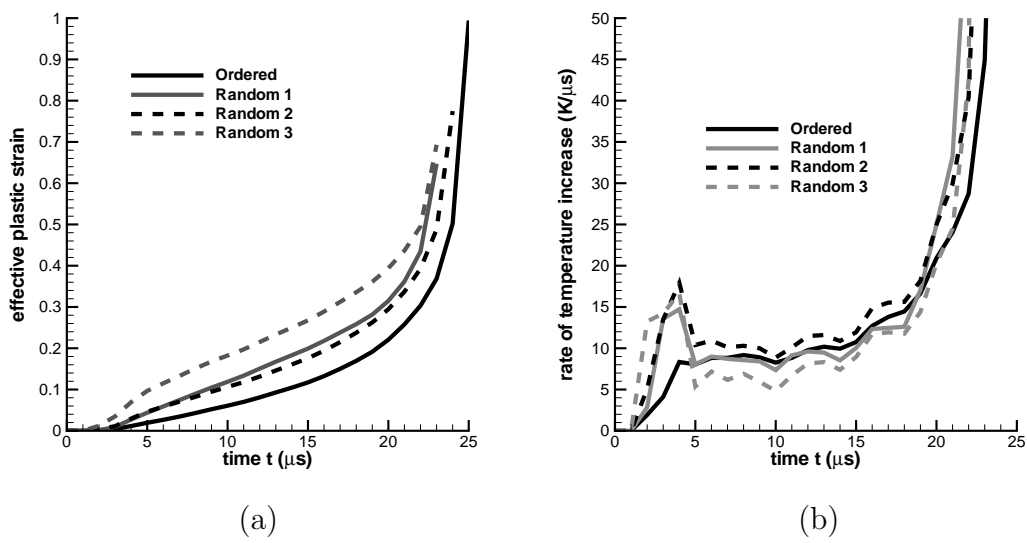
Figure 5.17: (a) Effective plastic strain and (b) rate of temperature increase at a point inside the ASB as functions of time for four particulate arrangements

5.4 Conclusions

We have studied the initiation and propagation of ASBs in particulate composites, using both plane strain tension tests at the meso-scale and a multi-scale analysis that bridges the length scales between meso- and macro-level analyses of the heterogeneous composite. It was found that the initiation and propagation of ASBs in particulate composites is decidedly different than that in the equivalent homogenized material (with properties derived from the technique presented in Chapter 2); particulate/matrix interfaces act as defects, promoting the formation of ASBs. We have modeled these defects in the homogenized material by assuming that the initial porosity varies affinely with the maximum value, f_{ce}, at the centroid of the cross-section. Values of f_{ce} between 0.0075 and 0.015 give ASB initiation times for the homogenized body that are close to those for the particulate composite.

The multiscale analyses of the particulate composite revealed that ASB initiation time is nearly one-half of that for the meso-scale analysis of a composite with the same volume fraction and distribution of particulates. Reasons for this difference are unclear and need to be investigated.

The ASB initiation criterion for heterogeneous solids is totally different from that for homogeneous bodies.

Chapter 6

Contributions

A significant contribution of the present work is the examination of a particulate composite under a wide variety of loading conditions at multiple length scales. A numerical homogenization technique for thermoelastoviscoplastic particulate composites was developed, enabling one to calculate effective viscoplastic parameters that are not easily obtained through traditional analytical methods. Adiabatic shear bands were studied for the first time in functionally graded materials, demonstrating that FGMs can produce quantitatively and qualitatively different results from homogeneous materials. Furthermore, the brittle and ductile failure of FGMs was studied; for the first time, a sustained ductile crack was simulated and analyzed. The initiation and propagation of adiabatic shear bands at the microstructural level was also studied-it was shown that prior ASB criteria were not applicable to a multi-constituent particulate composite. These contributions are detailed below.

We have used the finite element technique to study plane strain deformations of representative volume elements of tungsten/nickel-iron particulate composites. Through a constructed set of tests, effective material parameters such as Young's modulus, Poisson's ratio, strain- and strain-rate hardening parameters, thermal softening parameters, thermal conductivity and the coefficient of thermal expansion are determined for each given microstructure. It was found that particulate size and arrangement played little role in effective material properties as long as the arrangement is statistically isotropic. The effect of the volume fraction of constituents was also examined–effective material parameters for volume fractions between 50 and 80% of tungsten particulate were obtained for tungsten/nickel-iron (frequently referred to as tungsten-heavy alloy). The significant contribution is the homogenization technique, however–it can easily be adapted to any isotropic composite, giving effective material parameters that have been difficult to determine previously.

The plane-strain finite element code is then used to study the formation of adiabatic shear bands in functionally graded materials. FGMs were comprised of tungsten and nickel-

iron (as well as some tungsten and copper/iron/steel systems). It was shown that ASBs tend to form in the highly-ASB-susceptible region (in this case, tungsten). Furthermore, it was shown that ASB initiation occurred sooner in systems with more spatial variation of material properties, possibly due to the greater degree of inhomogeneity.

Brittle and ductile failure were studied in tungsten and nickel-iron as well as in W/NiFe FGMs. Brittle crack speed was found to follow the Rayleigh wave speed in the local material given a sufficient applied nominal strain-rate. Ductile failure was found to closely match the propagation speed of an ASB. It was also shown that ductile failure can be significantly delayed and the ductile crack speed altered by spatial variation in material properties. To the best of the author's knowledge, this work represents the first time the sustained propagation of a ductile crack has been simulated numerically.

A multiscale analysis technique was used to study the initiation and propagation of ASBs in particulate composites. Macro-scale analyses of an effective homogeneous material were used to derive boundary conditions for a micro-scale analysis. It was shown that ASB initiation location in a particulate composite is dependent on the microstructure (such as the arrangement of particulates), however, the initiation time is not significantly affected. Furthermore, it was shown that prior ASB initiation criteria are not applicable to particulate composites-load transfer between the constituents makes stress-based criteria unusable.

References

[1] Z. Hashin and S. Shtrikman. A variational approach to the theory of elastic behavior of multiphase materials. *J. Mech. Phys. Solids*, 11:127–140, 1963.

[2] T. Mori and K. Tanaka. Average stress in matrix and average elastic energy of materials with misfitting inclusions. *Acta Metal.*, 21:571–574, 1973.

[3] G.J. Weng. Some elastic properties of reinforced solids, with special reference to isotropic ones containing spherical inclusions. *Int'l J. Eng. Sci.*, 22:845–856, 1984.

[4] R.M. Christensen and K.H. Lo. Solution for effective shear properties of three phase sphere and cylinder models. *J. Mech. Phys. Solids*, 27:315–330, 1979.

[5] S. Nemat-Nasser and M. Hori. *Micromechanics: Overall Properties of Heterogeneous Materials*. Elsevier, Amsterdam, 1993.

[6] P. Suquet. Overall potential and extremal surfaces of power law or ideally plastic composites. *J. Mech. Phys. Solids*, 41:981–1002, 1993.

[7] J.R. Willis. The overall elastic response of composite materials. *J. Appl. Mech.*, 50:1202–1209, 1993.

[8] D.R.S. Talbot and J.R. Willis. Variational principles for inhomogeneous nonlinear media. *IMA J. Appl. Math.*, 35:39–54, 1985.

[9] P. Ponte Castaneda. Exact second order estimates for the effective mechanical properties of nonlinear composites. *J. Mech. Phys. Solids*, 44:827–862, 1996.

[10] P. Ponte Castaneda. Second-order homogenization estimates for nonlinear composites incorporating field fluctuations: I–theory. *J. Mech. Phys. Solids*, 50:737–757, 2002.

[11] I. Doghri and C. Friebel. Effective elasto-plastic properties of inclusion-reinforced composites; study of shape, orientation, and cyclic response. *Mechanics of Materials*, 2004.

[12] G.J. Dvorak and M.V. Srinivas. New estimates of overall properties of heterogeneous solids. *J. Mech. Phys. Solids*, 47:899–920, 1999.

[13] L.H. Dai, L.F. Liu, and Y.L. Bai. Effect of particle size on the formation of adiabatic shear bands in particle reinforced metal-matrix composites. *Materials Letters*, 58:1773–1776, 2004.

[14] H. Tresca. On further application to the flow of solids. *Proc. Inst. Mech. Engrs.*, 30:301–345, 1878.

[15] H.F. Massey. The flow of metal during forging. *Proc. Manchester Assoc. of Engineers*, pages 21–26, 1928.

[16] C. Zener and J.H. Hollomon. Effect of strain rate upon plastic flow of steel. *J. Applied Physics*, 15:22–32, 1944.

[17] R.F. Recht. Catastrophic thermoplastic shear. *J. Applied Mechs.*, 31:1898–193, 1964.

[18] Y.L. Bai. Thermoplastic instability in simple shear. *J. Mech. Phys. Solids*, 30:195–207, 1982.

[19] R.C. Batra and L. Chen. Effect of viscoplastic relations on the instability strain, shear band initiation strain, the strain corresponding to maximum shear band spacing, adn the band width in a thermoviscoplasatic material. *Int. J. Plasticity*, 17:1465–1489, 2001.

[20] A. Marchand and J. Duffy. An experimental study of the formation process of adiabatic shear bands in a structural steel. *J. Mech. Phys. Solids*, 36:251–283, 1988.

[21] R.C. Batra and K. Ko. Analysis of shear bands in dynamic axisymmetric compression of a thermoviscoplastic cylinder. *Int. J. Engng. Sci.*, 31:529–547, 1993.

[22] R.C. Batra and X.T. Zhang. On the propagation of a shear band in a steel tube. *J. Eng'g Materials and Technology*, 116:155–161, 1994.

[23] Y.L. Bai and B. Dodd. *Adiabatic Shear Localization: Occurence, Theories, and Applications*. Pergamon Press, Oxford, 1992.

[24] T.W. Wright. *The Physics and Mathematics of Adiabatic Shear Bands*. Cambridge University Press, Cambridge, 2002.

[25] Y. Tomita. Simulation of plastic instabilities in solid mechanics. *Appl. Mechs. Revs.*, 47:171–205, 1994.

[26] R. Armstrong, R.C. Batra, M. Meyers, and T.W. Wright. Shear instabilities and viscoplasticity theories. *Mechs. of Materials*, 17:83–328, 1994.

[27] R.C. Batra, Y.D.S. Rajapakse, and A. Rosakis. Failure mode transitions under dynamic loading. *Int. J. of Fracture*, 101:1–180, 2000.

[28] H.M. Zbib, T. Shawki, and R.C. Batra. Material instabilities. *Appl. Mech. Rev.*, 45:1–173, 1992.

[29] P. Perzyna, editor. *Localization and Fracture Phenomenon in Inelastic Solids*. Springer-Verlag, 1998.

[30] R.C. Batra and H.M. Zbib. *Material Instabilities: Theory and Applications*. ASME Press, 1994.

[31] D.P.H. Hasselman and G.E. Youngblood. Enhanced thermal stress resistance of structural ceramics ther thermal conductivity gradient. *J. American Ceramic Society*, 61:49–52, 1978.

[32] A. Kawasaki and R. Watanabe. Finite element analysis of thermal stress of the metals/ceramics multi-layer composites with controlled compositional gradients. *J. Japan Inst. Metals*, 52:525–529, 1987.

[33] N. Noda and T. Tsuji. Steady thermal stresses in a plate of functionally graded material. In M. Yamaouchi, M. Koizumi, T. Hirai, and I. Shiota, editors, *Proc. 1st Int. Symp. on Functionally Graded Materials*, pages 339–344, Sendai, Japan, 1990.

[34] Y. Tanigawa, Y. Ootao, and R. Kawamura. Thermal bending of laminated composite rectangular plates and nonhomogeneous plates due to partial heating. *J. Thermal Stresses*, 14:285–308, 1991.

[35] K. Ravichandra. Thermal residual stresses in a functionally graded system. *Material Science and Eng'g*, 201A:269–276, 1995.

[36] N. Noda. Thermal stress intensity factor for a functionally-graded plate. *J. Thermal Stresses*, 20:373–387, 1997.

[37] Y. Ootao and Y. Tanigawa. Three-dimensional transient thermal stresses of functionally graded rectangular plate due to partial heating. *J. Thermal Stresses*, 22:35–55, 1999.

[38] Z.H. Jin and R.C. Batra. Stress intensity relaxation at the tip of an edge crack in a functionally graded material subjected to a thermal shock. *J. Thermal Stresses*, 19:317–339, 1996.

[39] Z.Q. Cheng and R.C. Batra. Three-dimensional thermoelastic deformations of a functionally graded elliptic plate. *Composites: Part B*, 31:97–106, 2000.

[40] J.N. Reddy and Z.Q. Cheng. Three-dimensional thermomechanica deformations of functionally graded rectangular plates. *European Journal of Mechanics A/Solids*, 20:841–855, 2001.

[41] S.S. Vel and R.C. Batra. Exact solutions for thermoelastic deformations of functionally graded thick rectangular plates. *AIAA J.*, 40(7):1421–1433, 2002.

[42] S.S. Vel and R.C. Batra. Three-dimensional analysis of transient thermal stresses in functionally graded plates. *Int. J. of Solids and Structures*, 40:7181–7196, 2003.

[43] Z.G. Zhu and R.C. Batra. Analysis of shear banding in plane strain compression of bimetallic thermally softening viscoplastic body containing and elliptical void. *J. Engng. Mat. Tech.*, 113:382–395, 1991.

[44] R.C. Batra and Z.G. Zhu. Dynamic shear band development in a thermally softening bimetallic body containing two voids. *Acta Mechanica*, 86:31–52, 1991.

[45] R.C. Batra and Z.G. Zhu. Dynamic adiabatic shear band development in a bimetallic body containing a void. *Int. J. Solids Structures*, 27:1829–1854, 1991.

[46] Z. Wang and T. Nakamura. Simulations of crack propagation in elastic-plastic graded materials. *Mechanics of Materials*, 36:601–622, 2004.

[47] F. Erdogan. Fracture mechanics of functionally graded materials. *Composite Eng'g*, 5:753–770, 1995.

[48] Z.H. Jin and N. Noda. Crack-tip singular fields in nonhomogeneous materials. *ASME J. Appl. Mech.*, 61:738–740, 1994.

[49] J.W. Eischen. Fracture of nonhomogeneous materials. *Int. J. Fracture*, 34:3–22, 1987.

[50] T. Honein and G. Herrmann. Conservation laws in nonhomogeneous plane elastostatics. *J. Mech. Phys. Solids*, 45:789–908, 1997.

[51] P. Gu and R.J. Asaro. Crack deflection in functionally graded materials. *Int. J. Solids Structures*, 34:3085–3098, 1997.

[52] T.L. Becker, R.M. Cannon, and R.O. Ritchie. Finite crack kinking and t-stresses in functionally graded materials. *Int. J. Solids Structures*, 38:5545–5563, 2001.

[53] Z.H. Jin and R.C. Batra. Some basic fracture mechanics concepts in functionally graded materials. *J. Mech. Phys. Solids*, 44:1221–1235, 1996.

[54] Z.H. Jin and R.C. Batra. R-curve and strength behavior of a functionally graded material. *Material Sci. and Eng'g*, A242:70–76, 1998.

[55] C. Atkinson and R.D. List. Steady state crack propagation into media with spatially varying elastic properties. *Int. J. Eng. Sci.*, 16:717–730, 1978.

[56] L. Ma, L.Z. Wu, Z.G. Zhou, and T. Zeng. Crack propagating in a functionally graded strip under the plane loading. *Int. J. Fracture*, 126:39–55, 2004.

[57] K.H. Lee. Characteristics of a crack propagating along the gradient in functionally gradient materials. *Int. J. Solids Structures*, 41:2879–2898, 2004.

[58] V. Tvergaard. Theoretical investigation of the effect of plasticity on crack growth along a functionally graded region between dissimilar elastic-plastic solids. *Eng'g Fracture Mechanics*, 69:1635–1645, 2002.

[59] Z.H. Jin and R.H. Dodd. Crack growth resistance behavior of a functionally graded material: computational studies. *Eng'g Fracture Mechanics*, 71:1651–1672, 2004.

[60] R.C. Batra and N.A. Jaber. Failure mode transition in an impact loaded prenotched plate with four thermoviscoplastic relations. *Int. J. Fracture*, 110:47–71, 2001.

[61] A.L. Gurson. Continuum theory of ductile rupture by void nucleation and growth: Part i. *J. of Engr. Mater. and Tech.*, 99:2–15, 1977.

[62] Z.P. Wang and Q. Jiang. A yield criterion for porous ductile media at high strain rate. *J. Appl. Mech.*, 64:503–509, 1997.

[63] Z.P. Wang. Void-containing nonlinear materials subjected to high-rate loading. *J. Appl. Phys.*, 81:7213–7227, 1997.

[64] V. Tvergaard. Influence of voids on shear band instabilities under plane strain conditions. *Int. J. Fracture*, 17:389–407, 1981.

[65] G.R. Johnson and W.H. Cook. A constitutive model and data for metals subjected to large strains, high strain-rates, and high temperatures. *Proc. 7th Int'l Symp. on Ballistics*, pages 541–547, 1983.

98

[66] C. Chu and A. Needleman. Void nucleation in biaxially stretched sheets. *J. Engr. Mat. Tech.*, 102:249–256, 1980.

[67] V. Tvergaard and A. Needleman. Analysis of the cup-cone fracture in a round tensile bar. *Acta Metallurgica*, 32:157–169, 1984.

[68] B. Budiansky. Thermal and thermoelastic properties of isotropic composites. *J. Composite Materials*, 4:701–744, 1990.

[69] B. Jiang and R.C. Batra. Effective properties of a piezocomposite containing shape memory alloy and inert inclusions. *Continuum Mech. Thermodynamics*, 14:87–111, 2002.

[70] C. Cattaneo. A form of the heat equation which eliminates the paradox of instantaneous propagation. *CR Acad. Sci.*, 247:431–433, 1958.

[71] P. Vernotte. The true heat equation. *CR Acad. Sci.*, 247:2103, 1958.

[72] M. Chester. Second sound in solids. *Phys. Rev.*, 131:2013–2015, 1963.

[73] R.C. Batra and M.H. Lear. Adiabatic shear banding in plane strain tensile deformations of eleven thermoviscoplastic materials with finite wave speed. *Int. J. Plasticity*, page in press, 2004.

[74] R.C. Batra and L. Chen. Instability analysis and shear band spacing in gradient-dependent thermoviscoplastic materials with finite speeds of thermal waves. *Archives of Mechanics*, 53:167–192, 2001.

[75] R.C. Batra. Steady state penetration of thermoviscoplastic targets. *Comp. Mechs.*, 3:1–12, 1988.

[76] R.C. Batra and K.H. Kim. Effect of viscoplastic flow rules on the initiation and growth of shear bands at high strain rates. *J. Mech. Phys. Solids*, 38:859–874, 1990.

[77] S.R. Bodner and Y. Partom. Constitutive equations for elastic-viscoplastic strain-hardening materials. *J. Appl. Mech.*, 56:385–389, 1975.

[78] R.C. Batra and X.Q. Liang. Finite deformations of smart structures. *Comp. Mechs.*, 20:427–438, 1997.

[79] E. Zywicz and M. Puso. A general conjugate-gradient-based predictor-corrector solver for explicit finite element contact. *Int. J. Numer. Meth. Eng'g*, 44:439–459, 1999.

[80] N. Carpenter, R. Taylor, and M. Katona. Lagrange constraints for transient finite element surface contact. *Int. J. Numer. Meth. Eng'g*, 32:103–128, 1991.

[81] R.C. Batra and M.H. Lear. Simulation of brittle and ductile fracture in an impact loaded prenotched plate. *Int. J. Fracture*, 126:179–203, 2004.

[82] J.B. Stevens and R.C. Batra. Adiabatic shear bands in the taylor impact test of a wha rod. *Int'l J. Plasticity*, 14:841–854, 1998.

[83] R.C. Batra and B.M. Love. Adiabatic shear bands in functionally graded materials. *J. Thermal Stresses*, 2004.

[84] H. Hatta and M. Taya. Effective thermal conductivity of a misoriented short fiber composite. *J. Appl. Physics*, 58:2478–2486, 1985.

[85] Z. Hashin and B.W. Rosen. Effective thermal expansion coefficients and specific heats of composite materials. *Int. J. Eng. Sci.*, 8:157–173, 1970.

[86] R.C. Batra and D. Rattazzi. Adiabatic shear banding in a thick-walled steel tube. *Comp. Mechs.*, 5:426–442, 1997.

[87] R.C. Batra and C.H. Kim. Analysis of shear banding in twelve materials. *Int. J. Plasticity*, 8:425–452, 1992.

[88] R.C. Batra and Y.W. Kwon. Adiabatic shear banding in a bimetallic body. *Acta Mechanica*, 77:281–297, 1989.

[89] M. Zhou, A. Needleman, and R.J. Clifton. Finite-element simulation of shear localization in plate impact. *J. Mechs. Phys. Solids*, 42:423–458, 1994.

[90] R.C. Batra and G.M. Zhang. Analysis of adiabatic shear bands in elastothermoviscoplastic materials by modified smoothed-particle hydrodynamics method. *J. Comp. Phys.*, 2004.

[91] R.C. Batra and B.M. Love. Crack propagation due to brittle and ductile failures in microporous thermoelastoviscoplastic functionally graded materials. *submitted for publication*.

[92] R.O. Ritchie, J.F. Knott, and J.R. Rice. On the relationship between critical tensile stress and fracture toughness in mild steel. *J. Mech. Phys. Solids*, 21:395–410, 1973.

[93] J.A. Hendrickson, D.S. Wood, and D.C. Clark. The initiation of brittle fracture in mild steel. *J. Mech. Phys. Solids*, 50:656–681, 1958.

[94] R.C. Batra. Finite plane strain deformations of rubberlike materials. *Int. J. Numer. Meth. Eng'g*, 15:145–160, 1980.

[95] T.C. Chiu and F. Erdogan. One-dimensional wave propagation in a functionally graded medium. *J. Sound and Vibration*, 222:453–487, 1999.

[96] L.B. Freund. Crack propagation in an elastic solid subjected to general loading - iii. stress wave loading. *J. Mech. Phys. Solids*, 21:47–61, 1973.

[97] R.C. Batra. The initiation and growth of, and the interaction among adiabatic shear bands in simple and dipolar materials. *Int. J. Plasticity*, 3:75–89, 1987.

[98] R.C. Batra and C.H. Kim. Adiabatic shear banding in elastic-viscoplastic nonpolar and dipolar materials. *Int. J. Plasticity*, 6:127–141, 1990.

[99] R.C. Batra and J. Hwang. Dynamic shear band development in dipolar thermoviscoplastic materials. *Computational Mechs.*, 12:354–369, 1994.

[100] R.C. Batra and C.H. Kim. Analysis of shear banding in twelve materials. *Int. J. Plasticity*, 8:425–452, 1992.

[101] M. Zhou. The growth of shear bands in composite microstructures. *Int. J. Plasticity*, 14:733–754, 1998.

[102] R.D. Dick and et al. V. Ramachandran. In A. Crowson and E.S. Chen, editors, *Tungsten and Tungsten Alloys–Recent Advances*, pages 269–276. The Minerals, Metals & Materials Society, 1991.

Vita

Bryan Matthew Love was born on July 22, 1978 in Charlotte, North Carolina to Thomas and Karen Love. He graduated from North Carolina State University in 1999 with a B.S. in Mechanical Engineering. He continued his education at NCSU, completing a M.S. in Mechanical Engineering in 2001. Subsequently, he enrolled at the Virginia Polytechnic Institute and State University in the fall of 2001, pursuing his PhD in Engineering Mechanics under the guidance of Professor Romesh Batra. After graduation, he plans to pursue a faculty position at a major research university.